Accurate optical simulation of disordered scattering layers for light extraction from organic light emitting diodes

Zur Erlangung des akademischen Grades eines

DOKTOR-INGENIEURS

von der KIT-Fakultät für Elektrotechnik und Informationstechnik
des Karlsruher Instituts für Technologie (KIT) genehmigte

DISSERTATION

von

Dipl.-Phys. Amos Egel

Tag der mündlichen Prüfung:	26.7.2018
Hauptreferent:	Prof. Dr. Uli Lemmer
Korreferent:	Prof. Dr. Carsten Rockstuhl

This document is licensed under a Creative Commons Attribution 4.0 International License
(CC BY 4.0): https://creativecommons.org/licenses/by/4.0/deed.en

Meinem Großvater Franz Egel gewidmet

Abstract

This thesis presents a method for the comprehensive optical simulation of disordered scattering layers that can be used for light extraction in organic light emitting diodes (OLEDs). The method is accurate in the sense that it solves Maxwell's equations for dipole emission into a plane parallel system of layers including multiple scattering particles. To this end, the electromagnetic field is computed by means of an expansion in *spherical waves* (to treat the scattering by the individual particles) as well as in *plane waves* (for the propagation of the field through the OLED thin film system).

After visiting the fundamentals of OLEDs and the issue of trapped light, the relevant multiple-scattering formulas are derived in an *excitation-response* notation. They allow the formulation of the scattering problem in terms of a linear system of equations for the scattered field coefficients, featuring the so called *T-matrix* to account for the scattering properties of the individual particles.

Numerical aspects of an efficient assembly and solution of the linear system are discussed, and formulas to process the solution further into the relevant figures of merit (electric field distribution, dissipated dipole power, power flux through surfaces, far field intensity distribution) are given.

The presented formalism has been implemented into a freely available software package, *Smuthi*. The program structure is sketched and the validity of the implementation is demonstrated by a comparison to finite-elements calculations.

Finally, the simulation method is applied to a typical OLED light management scenario: it consists of a flat scattering layer integrated within a white OLED, whose planar layout and the location of the emission zones have been optimized beforehand to optimize the outcoupling efficiency. This way, a fair estimate for the gain in outcoupling efficiency through an internal scattering layer is provided.

It is noted that the range of possible use cases for the presented theoretical formalism and for the software package is not limited to light extraction from OLEDs, but includes many other applications that involve particles near planar interfaces.

Zusammenfassung

Diese Arbeit handelt von einer Methode zur umfassenden optischen Simulation von organischen Leuchtdioden (OLEDs) mit internen ungeordneten Streuschichten zur Lichtauskopplung. Die Methode ist exakt in dem Sinne, dass sie die Lösung der Maxwellgleichungen für Dipolstrahlung in einem planparallelen Schichtsystem mit mehreren Streupartikeln ermöglicht. Dies wird durch die Entwicklung des gestreuten elektromagnetischen Feldes in Kugelvektorwellenfunktionen (zur effizienten Handhabung der Streuung an den einzelnen Partikeln) sowie in ebenen Wellen (zur Handhabung der Propagation des Lichtes durchs Dünnschichtsystem) erreicht.

Nach einer Einführung zum Thema OLEDs mit einem besonderen Augenmerk auf Lichtauskopplung werden die relevanten Formeln für die Mehrfachstreuung in einem Formalismus von Anregung und Systemantwort hergeleitet. Auf diese Weise kann das Streuproblem in ein System von linearen Gleichungen überführt werden, das auf der Grundlage des T-Matrix Formalismus' die Berechnung der Streukoeffizienten erlaubt.

Es werden auch numerische Aspekte einer effizienten Aufstellung und Lösung dieses Gleichungssystemes erörtert und Gleichungen, welche die Berechnung der interessanten Kenngrößen ermöglichen, werden hergeleitet (elektrische Feldverteilung, dissipierte Leistung, Leistungsfluss durch Grenzflächen, Fernfeld-Intensitätsverteilungen).

Die hier vorgestellte Simulationsmethode wurde auch in einer frei verfügbaren Software (*Smuthi*) implementiert. Die Programmstruktur von Smuthi wird skizziert, und die Korrektheit der Simulationsergebnisse wird durch einen Vergleich mit Finite-Elemente Rechnungen belegt.

Abschließend wird die Simulationsmethode an Hand einer praxisrelevanten Fallstudie illustriert. Hierzu wird eine weiße OLED, deren Auskoppeleffizienz bereits durch Anpassen der Schichtdicken und der Lage der Emissionszonen optimiert worden ist, mit einer internen Streuschicht versehen und der erwartbare Zugewinn in der Lichtausbeute durch Simulationen berechnet.

Außer der Lichtauskopplung aus OLEDs kann der hier präsentierte theoretische Formalismus und die Software für zahlreiche andere Anwendungen genutzt werden, welche die Streuung von Licht an Partikeln in der Nähe von ebenen Grenzflächen beinhalten.

Preface

When I started my PhD project in the summer of 2012, my initial objective was to study mechanisms of light scattering in layered media in order to identify design rules for efficient organic light emitting diodes (OLEDs)[1]. My work was thus planned to be part of a broader experimental research effort carried out at the Light Technology Institute [1] with the aim of improving the efficiency of (mostly wet processed and eventually printed) OLEDs – and simulations were supposed to be a mere tool that would be used to approach this goal.

But soon it became evident that the numerics of scattering by disordered structures in OLEDs is a difficult and interesting problem on its own. A major challenge is that OLEDs with scattering layers involve multiple length scales: from the wavelength of light, the layer thicknesses and the size of scattering particles, each in the order of hundreds of nanometers, over the decay length of waveguide modes in the order of tens of microns to the thickness of the substrate layer in the order of millimeters. This makes the choice of a suitable modeling approach difficult, because each technique usually applies only to a certain regime of length scales.

The focus of my project gradually shifted from

> *"What can we learn from optical simulations for the design of OLEDs with scattering layers?"*

towards

> *"What numerical strategy is best suited for the optical simulation of scattering layers in OLEDs?"*

The latter became the central question of my PhD studies. The new goal was to identify a simulation method that is accurate and numerically efficient at the same time.

The existing literature on optical simulations of scattering layers in OLEDs offered basically two types of approaches: The first kind would apply approximate numerical methods with restrictive assumptions like independent scattering or incoherent multiple scattering. A frequently seen example is the usage of Monte-Carlo ray optics scattering for disordered nanoscopic geometries. These simulation strategies run with a moderate computational workload, but the underlying assumptions are in general not fulfilled and it is not clear how accurate the results are.

[1] As will be explained in chapter 1, OLEDs suffer from light trapping and scattering layers can be used for light extraction.

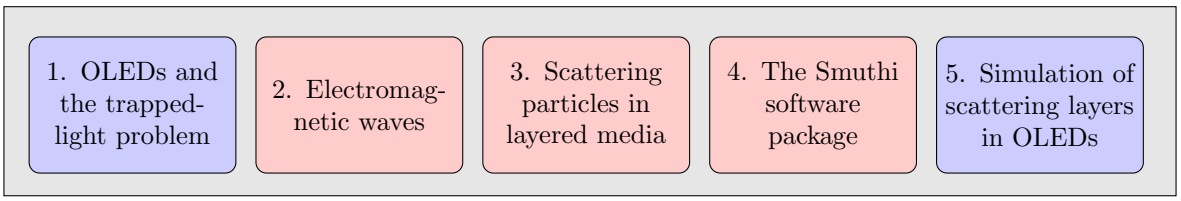

Figure – Outline of this thesis. The chapters follow an A-B-B-B-A structure, where A refers to OLEDs (blue) and B refers to electromagnetic scattering (red).

The second class of approaches follows rigorous modeling concepts like the finite element (FEM) or the finite difference time domain (FDTD) method. These simulations usually bring an enormous computational workload and are thus limited to a simulation volume spanning a couple of wavelengths. It is then not straightforward to derive macroscopic device parameters from these microscopic simulations.

With a look at the general electromagnetic scattering literature, it became clear that one of the most powerful techniques for the simulation of scattering by particles is the T-matrix method [2]. In the OLED literature, it seemed to be almost completely unknown (one exception being a book chapter by Tishchenko [3]) although extensions of the T-matrix method to multiple scattering [4] and to particles near infinite interfaces [5, 6] had existed for a long time. In addition to its relatively low recognition in the nano-photonics research community, the lack of available computer codes for particles near interfaces prevented the T-matrix method to be used more frequently for these applications.

In light of these observations, the scope of this thesis is to ...

- transfer the T-matrix concept to scattering by many particles in stratified media
- identify numerical bottlenecks and present strategies for computational efficiency
- introduce a computer code (Smuthi) for the simulation of light scattering by particles near or between planar interfaces
- demonstrate that the suggested concepts are well suited for the accurate simulation of relevant optical figures of merit of macroscopic OLED devices.

In that regard, this thesis addresses two scientific disciplines: the OLED research and the electromagnetic scattering research. In fact, the theoretical and numerical concepts as well as their implementation are not limited to the use in OLED simulations, but can be applied to many fields including meta surfaces, near field microscopy or the scattering of surface plasmon polaritons by particles on a metal surface – basically any application involving scattering by particles near planar interfaces.

Accordingly, I have tried to prepare the thesis such that it is accessible for readers from the OLED community without a dedicated interest in numerical details (they

might want to read chapters 1 and 5 only) as well as for readers from the electromagnetic scattering community or users of the Smuthi software package (who might want to read chapters 2 to 4 only), compare the above chapter flowchart.

As a consequence, there are two introductory chapters: In chapter 1, OLEDs and the trapped light problem are introduced, and basic concepts for the optical modeling of OLEDs are reviewed. Chapter 2 then takes a step back and introduces some concepts of electrodynamic theory that will be needed later on, especially the vector wave functions as a basis set of solutions to the Maxwell equations in homogeneous space, as well as an *excitation-and-response* formalism for the propagation of waves in a planarly layered medium. Chapter 3 is the central part of this work. It contains the derivation of the multiple scattering formalism for particles in a layered medium as well as a discussion of some numerical aspects. Chapter 4 introduces Smuthi, a freely available software package for the simulation of scattering by multiple particles in a layered medium. Chapter 5 demonstrates how the presented computational strategy and computer code can be applied to a realistic optimization problem of scattering layers in white OLEDs. Equipped with the newly developed theoretical tools, the OLED extraction problem is taken up again, and the simulated extraction efficiency for OLEDs with scattering layer is compared to that of OLEDs without scattering layer. Finally, in chapter 6 I draw conclusions and give an outlook on possible future developments.

Contents

1. OLEDs and the trapped-light problem

This chapter introduces the working principles of organic light emitting diodes (OLEDs) (section 1.1), and loss mechanisms that limit the efficiency of OLEDs are discussed, with an emphasis to waveguiding losses (section 1.2). The outcoupling efficiency is identified as the figure of merit with the most direct connection to optical simulations, and various approaches to enhance the light extraction are reviewed. Fundamental concepts of optical OLED modeling are introduced (section 1.3). As the central figure of interest, the extraction pattern is defined. A semi-quantum mechanical approach is compared to the (more usual) classical modeling framework. Finally, the state of the art for the optical simulation of internal scattering layers in OLEDs is reviewed.

Organic light emitting diodes (OLEDs) turn electrical energy into visible light. They are organic in the sense that emitter materials are carbon-based, in contrast to conventional inorganic light emitting diodes (LEDs) made of inorganic crystalline semiconductors. The working principle is based on molecular electroluminescence, that is the decay of an excited molecular electronic state to a state of lower energy under emission of a photon, while the electronic excitation is achieved by applying a voltage.

1.1. The working principle of an OLED

1.1.1. The OLED stack

Due to the limited electrical conductivity of organic materials, OLEDs are designed as thin-film devices with layer thicknesses in the range of $\sim 10\,\mathrm{nm}$ to $\sim 100\,\mathrm{nm}$ but with lateral dimensions that can range in the order of centimeters (thus, OLEDs are *area light sources*). The bottom of the OLED stack is given by a mechanically stable or flexible substrate layer. The lateral charge transport is provided by two electrode layers, and the active material is sandwiched between them (see figure 1.1). The charge carriers thus only need to travel a distance in the order of the layer thickness through the emitter layer. In so called *bottom-emitting OLEDs*, all layers below the emitter layer are transparent in order to allow the photons to propagate through the bottom side out of the OLED, whereas in *top-emitting OLEDs*, the layers above the emitter layer

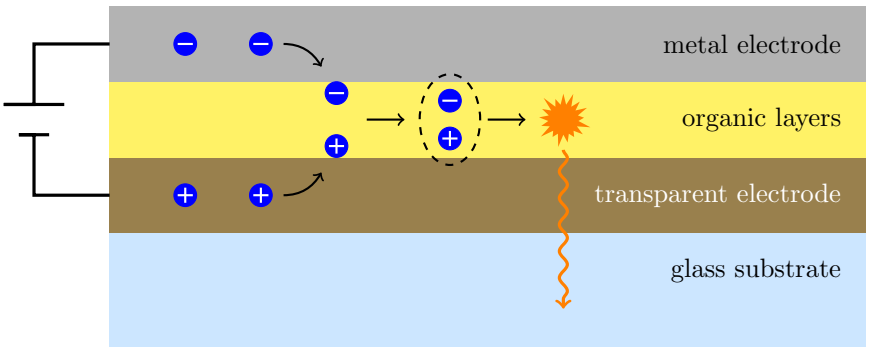

Figure 1.1. – Working principle of a bottom-emitting OLED: Charges are injected into and transported through the emitter layer by applying a voltage between the electrode layers. The charges form bound states (excitons) which eventually decay to emit a photon.

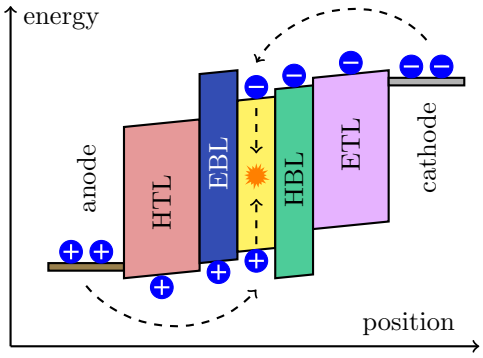

Figure 1.2. – Energy diagram of a typical OLED stack consisting of anode, hole transport layer (HTL), electron blocking layer (EBL), emitter layer, hole blocking layer (HBL), electron transport layer (ETL) and cathode. Electrons propagate in the *lowest unoccupied molecular orbital* (LUMO), whereas holes propagate in the *highest occupied molecular orbital* (HOMO) of the respective layer materials.

are transparent. If both is the case, a *semi-transparent OLED* can be realized. In any case, at least one of the two electrodes needs to be transparent. So called transparent conducting oxides (TCOs) like indium doped tin oxide (ITO) or aluminum doped zinc oxide (AZO) are typically employed.

In order to shape the emission spectrum of white OLEDs, several emitter layers covering different parts of the visible light spectrum can be combined. Further, additional layers can be included to improve the internal quantum efficiency: charge injection layers improve the charge injection by energy level alignment, charge transport layers avoid space charges and charge blocking layers confine the charges in the desired emission zone. A typical OLED energy level diagram is depicted in figure 1.2.

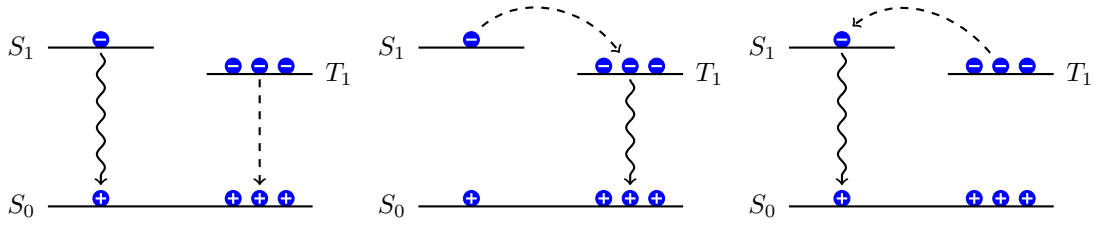

Figure 1.3. – Electroluminescence mechanisms in OLEDs. Left: Fluorescence (only singlet excitons decay under emission of a photon). Middle: Phosphorescence (also triplet excitons decay radiatively). Right: Thermally activated delayed fluorescence (triplet excitons are thermally elevated to the singlet state from where they decay radiatively).

1.1.2. Molecular luminescence

Electrons and holes are attracted to each other by the Coulumb force. In organic materials, the screening of that force is weak such that bound states of one electron and one hole, called *excitons*, emerge. Here, singlet excitons with a total spin of zero are distinguished from triplet excitons with a total spin of one. Only the former can decay radiatively to the molecule's ground state without violating the quantum mechanical selection rules. As the multiplicity of triplet excitons is three times higher than that of singlet excitons, only $25\,\%$ of the excitons that form under electrical operation of an OLED are at first in the singlet state.

Fluorescent emitter based OLED devices which do not offer a harvesting mechanism for triplet excitons, can therefore not have an efficiency larger than $25\,\%$, because the energy of triplet excitons is wasted to non-radiative decay channels. In contrast, *phosphorescent* emitter materials allow higher internal quantum efficiencies (see section 1.2) of up to $100\,\%$ [7]. Heavy nuclei like iridium in the molecule lead to a high spin-orbit interaction which enhances the probability of the "forbidden" radiative decay of triplet excitons. Finally another class of emitter materials, allowing *thermally activated delayed fluorescence* [8] have been demonstrated to yield high internal quantum efficiencies: They are characterized by a small energy difference between singlet and triplet excitons, such that the latter can be thermally converted into the former.

1.2. Efficiency

Various figures of merit can be defined to quantify the efficiency of an OLED. In this work, I focus on the *external quantum efficiency* η_{ext}, because it is most directly related to the (passive) optical properties of the OLED. The external quantum efficiency is defined as the number of emitted photons $N_{\gamma,\mathrm{out}}$ divided by the number of electrons

N_e injected into the device:

$$\eta_{\text{ext}} = \frac{N_{\gamma,\text{out}}}{N_e} \tag{1.1}$$

An ideal (single-junction) OLED would have a quantum efficiency of 1, but in real devices, absorption on the one hand and electronic losses on the other hand lead to significantly smaller values, such that

$$\eta_{\text{ext}} = \eta_{\text{int}}\eta_{\text{out}}, \tag{1.2}$$

where η_{int} denotes the *internal quantum efficiency*, that is the number of generated photons divided by the injected number of electrons and η_{out} denotes the *outcoupling efficiency*, that is the number of emitted photons divided by the total number of generated photons, including the absorbed.

It is instructive to further split up the internal quantum efficiency into factors representing the various loss mechanisms [9]. First, the number of formed excitons divided by the number of injected charge carriers is denoted by γ. It is also called the charge balance factor, because if an unequal amount of electrons and holes are injected, then $\gamma < 1$.

Further, the singlet/triplet factor $\eta_{\text{S/T}}$ accounts for the fact that during electrical operation of an OLED, the probability to form triplet excitons is 0.75, whereas the probablity to form singlet excitons is 0.25. As explained in section 1.1.2, up to 75% of the generated excitons are thus lost for light production due to selection rules. This scenario would correspond to a singlet/triplet factor of $\eta_{\text{S/T}} \approx 0.25$, whereas $\eta_{\text{S/T}} = 1$ for a material where both singlet and triplet excitons contribute to light generation.

Finally, the actual rate of radiative exciton decay can be smaller than the value dictated by spin statistics, because other loss mechanisms like non-radiative decay or "quenching" (non-radiative energy transfer to non luminescing molecules) are present. This additional loss is denoted by q_{eff}. Collecting these loss mechanisms, the external quantum efficiency is written as

$$\eta_{\text{ext}} = \gamma\eta_{\text{S/T}}q_{\text{eff}}\eta_{\text{out}}. \tag{1.3}$$

By selection of appropriate materials and by a wise stack design, each of these loss factors can be addressed and optimized, see for example [9,10].

1.2.1. The trapped-light problem

While OLEDs with an internal quantum efficiency of approximately $100\,\%$ are feasible [7], it is mainly the outcoupling efficiency that ultimately limits the external quantum efficiency. As the refractive index of the organic layers ($n \sim 1.75$) as well as that of the transparent electrode layers ($n \sim 1.85$) is usually higher than that of the

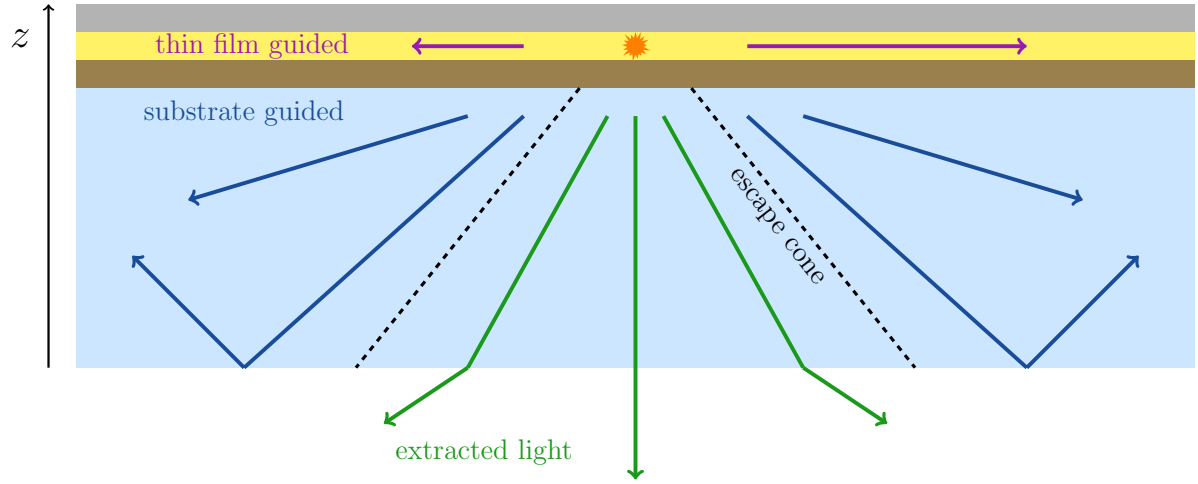

Figure 1.4. – Trapped light in an OLED: Only photons that are emitted into the escape cone of the substrate (i.e., with an emission angle smaller than the critical angle for total internal reflection) contribute to the usable light output.

substrate ($n \sim 1.5$), the OLED stack as depicted in figure 1.4 forms a slab waveguide structure with waveguide modes that are confined in the thin-film system, see also figure 1.5. In the following, I will refer to light in these modes as *thin-film guided light*. In addition, for bottom-emitting and transparent OLEDs, the substrate's refractive index is higher than that of air, and further waveguide modes exist that can propagate in the substrate but not in the air. These modes will be referred to as *substrate modes*.

Light emission from inside the emitter layer will necessarily excite the thin-film and substrate waveguide modes. These compete with the radiation out of the device, such that the external quantum efficiency of conventional white OLEDs is limited to $\eta_{\text{ext}} \lesssim 25\,\%$ [10].

1.2.2. Light extraction approaches

Numerous approaches have been suggested to improve light extraction from waveguide modes or to suppress their excitation. Several review articles have been dedicated to this topic [9, 11–13]. In the following, the most important ideas will be enumerated.

Some light extraction approaches only aim at the extraction or suppression of substrate modes. They are referred to as *external outcoupling*. Other approaches mostly aim at the extraction or suppression of thin-film guided modes. This is referred to as *internal outcoupling*.

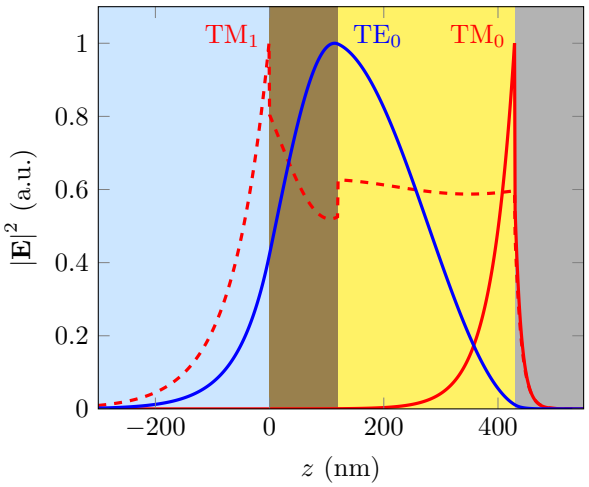

Figure 1.5. – Electric field profile of waveguide modes for a typical OLED structure. The stack supports three modes: The fundamental (TM_0) and first order (TM_1) transverse magnetic mode as well as the fundamental transverse electric mode (TE_0). The TM_0 mode is also called surface plasmon polariton (SPP).

Micro-cavity optimization Interference in the OLED thin-film system influences the fraction of photons trapped in waveguide modes. A careful choice of the layer thicknesses and the inclusion of additional optical spacer layers can significantly enhance the (internal and external) outcoupling efficiency. In particular, the distance of the emitting molecule from the metal electrode is an important parameter. Section 5.1 presents a detailed discussion of the stack optimization with regard to outcoupling efficiency of white OLEDs.

Dipole moment orientation Luminescent molecules are dipole emitters, see chapter 1.3. The light emission is preferred in the directions perpendicular to the transition dipole moment, whereas in the direction parallel to the dipole moment, emission is suppressed. A statistically preferred in-plane orientation of the dipole moments ("horizontal dipoles") thus leads to a greatly enhanced (internal and external) outcoupling compared to a statistically isotropic or out-of-plane orientation ("vertical dipoles") [9, 14–17]. Emitter molecules can be chemically designed to show a preferred orientation of transition dipole moments. In combination with suitable deposition techniques, the alignment of the dipole moments with the layer interfaces and thereby the outcoupling efficiency can be positively influenced.

Macro-extractors Macro extractors achieve almost $100\,\%$ external outcoupling. A macroscopic glass half sphere is brought into optical contact with the substrate using index-matching oil. If the dimension of the active area is much smaller than the glass half sphere's size, all light rays approach its surface approximately under normal incidence, such that reflection is effectively suppressed [9]. Alternatively, a prism

instead of a half sphere can be used [18]. For large-area OLEDs, this approach is not practicable because very large extractors would be required. For an analysis of the total light emitted into the substrate, macro-extractors are very useful. The so extracted light pattern, measured with respect to its spectral, angular and polarization dependence, allows for conclusions regarding the emission zone, emitter orientation and internal quantum efficiency [14, 17, 19–22].

External particle-based scattering layers A scattering layer is deposited on the bottom side of the substrate (i.e., the air side) [23–26]. When propagating through that layer, the direction of a light ray is changed in a probabilistic manner. This redistribution of propagation angles allows for a photon recycling of the trapped light: Rays that have undergone total internal reflection at the substrate/air interface need to pass the scattering layer before hitting that interface again, such that they are not necessarily in the angular regime of total reflection anymore and thus get a "second chance" to escape. In terms of fabrication, this approach is quite simple. Scattering particles are dispersed into a matrix material, and this mixture is applied to the substrate back side after the actual OLED fabrication steps have been completed. The drawback is that only external outcoupling can be achieved.

External micro-structures Instead of particle-based scattering structures, microstructures can be used to redistribute the light in the substrate. The most prominent example are micro-lenses [27–30]. Pyramids or roughened surfaces have been proposed, too [18]. In contrast to the macro-extractor the projected surface area is not larger than the active area of the OLED, such that due to Étendue conservation, a complete light extraction is not possible. However, for non Lambertian emission profiles from the OLED stack into the substrate, the shape of the micro structures can be adapted to yield an optimal external outcoupling efficiency [31].

High index substrates Technologically, internal outcoupling is more difficult than external outcoupling, because internal scattering structures carry the risk of introducing shunts in the electrically relevant layers. One solution is to use high index glasses or plastics for the substrate of bottom emitting OLEDs and thereby eliminate the refractive index contrast between the thin film system and the substrate [32–34]. This way, no thin-film guided modes are supported, and the increased portion of substrate guided light can be extracted through external structures, see above. The approach can be regarded as an internal outcoupling technique, but it only works in combination with additional external outcoupling. In the case of high index glass as substrate, a drawback of this method is high material cost.

Periodic internal structures One dimensional (gratings, [35–41]) or two dimensional (photonic crystal slabs, [42–45]) periodic scattering structures have been introduced into the thin film system to couple the internal waveguide modes to radiation. These structures are typically fabricated in a top-down manner by means of lithographic techniques. This approach allows good control over the achieved structures, but the emission characteristics of such devices often shows angular color distortions due to deterministic outcoupling of the waveguide modes into certain directions.

Disordered internal structures Scattering structures without periodicity can be fabricated using bottom-up techniques like dewetting of thin metal films as etch masks [46–48], microsphere lithography [49] or phase separation of polymer blends [49–57]. Cylindrical nano discs or nano pillars can be formed, and planarized by a transparent layer of different refractive index. In bottom-emitting OLEDs, such structures are typically inserted between the substrate and the transparent electrode. The remaining OLED stack can then be applied without alteration on top of the scattering layer, which can in fact be regarded as part of the substrate. Using internal disordered scattering layers in combination with a macro-extractor and an emitter material with a horizontal dipole orientation, a record efficiency of $\eta_{\mathrm{ext}} = 78\,\%$ has recently been claimed [58].

Volumetric internal scattering layers Another very promising approach relies on internal scattering layers on the basis of nano particles [25, 26, 59–70]. Again, the preferred location for such layers in bottom-emitting OLEDs is between the substrate and the transparent electrode. The scattering intensity can be tuned by changing the particle concentration, size and material. Compared to 2D-disordered scattering structures, the scattering layers on the basis of nano particles are quite thick (in the range of several micron). Consequently, the scattering matrix material needs to have a high refractive index in order to allow the thin-film guided modes to propagate in the scattering layer. This can be achieved by mixing smaller nano particles into the layer. The resulting effective refractive index can be tuned by the volume fraction of these smaller, non scattering particles [62]. The most frequently used material used for the scattering particles is $\mathrm{TiO_2}$ due to its high refractive index and low absorption. Alternatively, hollow-core nano particles have been proposed [68], exploiting the low refractive index of air. In fact, it is the refractive index contrast to the host medium which yields scattering.

Rough internal interfaces Surface roughening of the substrate by means of sand blasting, abrasion and wet etching has been proposed to introduce a scattering internal interface. After application of a thin film of a high index material, the rough surface can be planarized with a polymer layer [71].

Corrugated OLED stack One can also produce an OLED stack such that the electrically relevant layers, especially the metal electrode, is corrugated [35, 72–74]. The advantage is a comparatively large scattering effect, that also couples surface plasmon polariton (SPP) modes to radiation. This is difficult to achieve with other approaches, as the mode overlap of the SPP modes with the scattering centers is weak for planarized structures. A drawback of this approach is that the electrical properties of the OLED are affected, and it is difficult to exclude an introduction of shunts. For top-emitting OLEDs, corrugation of the layer stack is nevertheless the most important approach for outcoupling [75, 76].

1.3. Optical modeling concepts

Optical simulations are of great importance in the layout of OLED designs, as they allow to predict the outcoupling efficiency [77] as well as the color and angular emission properties for a given layer stack. Compared to purely experimental optimization approaches, where the variation of parameters require the production of many samples, OLEDs with desired properties can be designed with less effort and materials consumption. In addition, optical simulations have successfully been used to draw conclusions on internal OLED properties [14, 21] such as emission zones [19], transition dipole orientation distributions [17, 22] and internal quantum efficiencies [20]. This can be achieved by measuring the angular and polarization resolved spectral light output into the substrate using a goniometer setup with macro-extractor and then fitting simulated emission patterns to the measured.

In order to achieve a simple optical model, it is common to apply the following idealizations:

- Layers are homogeneous (constant refractive index)[1].
- Layers are bounded by parallel planes. That implies that surface roughness is neglected.
- Layers are infinitely extended into the lateral direction.

These idealizations can be subsumed in stating that the OLED thin-film system is a stratified medium, see chapter 2.4. Further,

- Light emission is assumed to originate from electric dipole transitions (higher orders are neglected, see section 1.3.2).
- The coherence length of the molecular luminescence is assumed to be large compared to the thin film thicknesses, whereas in the substrate, incoherent light propagation is assumed (see section 1.3.1).

[1] This approximation prohibits the treatment of absorption in the emitter layer, because dipole life times in absorbing media are zero.

All of these approximations are well justified in most practical cases, and excellent agreement between measurement and simulation has been achieved (see for example [9,20,77]).

1.3.1. The extraction pattern

The propagation of light through a bottom-emitting OLED stack is inherently a multi-scale problem: Whereas the thin-film system of the OLED is characterized by layer thicknesses in the nano scale (such that a wave optics treatment is essential in order to account for interference), the substrate and possible external micro-structures are much larger than the wavelength of visible light such that a ray optics treatment is more appropriate.

In order to achieve an overall optical model of the bottom-emitting OLED, one can define the *extraction pattern* as the central quantity[2] [78]:

$$X_j^{\mathrm{air}}(\lambda,\beta) = \frac{1}{P_0(\lambda)} \frac{\mathrm{d}}{\mathrm{d}\beta} P_j^{\mathrm{air}}(\lambda), \tag{1.4}$$

where λ denotes the vacuum wavelength, β is the polar propagation angle with $\pi/2 \leq \beta \leq \pi$, see figure 1.6, $P_0(\lambda)$ is the internal spectrum (that is the rate of photons generated per wavelength times the photon energy), j is an index to distinguish between TE ($j = 1$) and TM ($j = 2$) polarized radiation and $P_j^{\mathrm{air}}(\lambda)$ is the total power of light emitted with polarization j and wavelength λ. If the extraction pattern and the internal spectrum are known, the outcoupling (quantum) efficiency can be calculated according to

$$\eta_{\mathrm{out}} = \sum_{j=1}^{2} \frac{\int \mathrm{d}\lambda\, P_0^{\gamma}(\lambda) \int \mathrm{d}\beta\, X_j^{\mathrm{air}}(\lambda,\beta)}{\int \mathrm{d}\lambda\, P_0^{\gamma}(\lambda)}$$

with $P_0^{\gamma}(\lambda) = P_0(\lambda)/\hbar\omega$ denoting the internal photon number spectrum (as opposed to the energy spectrum $P_0(\lambda)$). Before calculating the extraction pattern to the air, it is first necessary to solve for the radiation pattern in the substrate in analogy to (1.4),

$$X_j^{\mathrm{sub}}(\lambda,\beta) = \frac{1}{P_0(\lambda)} \frac{\mathrm{d}}{\mathrm{d}\beta} P_j^{\mathrm{sub}}(\lambda), \tag{1.5}$$

where $P_j^{\mathrm{sub}}(\lambda)$ is the intensity inside the substrate. In contrast to the extraction pattern to the air, the radiation pattern in the substrate contains radiation propagating in both *downward* directions $\pi/2 \leq \beta \leq \pi$ and *upward* directions $0 \leq \beta \leq \pi/2$, due to the reflection from the substrate/air interface.

[2] I assume that all structures of the OLED are statistically isotropic with regard to rotations around the direction normal to the layer interfaces. Therefore, the extraction pattern is assumed to only depend on the polar angle.

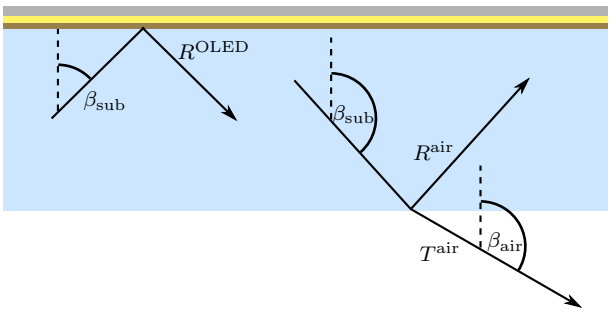

Figure 1.6. – Light propagation in the substrate.

Solving for X_j^{sub} is thus a ray optics problem with the following boundary conditions [78]:

- An *initial substrate pattern* $X_j^{\mathrm{sub},0}(\lambda, \beta)$ which corresponds to the initial radiation from the active OLED thin film stack into the substrate, divided by the total dissipated power. The initial substrate pattern is computed by means of a wave optics calculation. Interference effects are essential.
- The *reflectivity* of the OLED stack, which is again the solution of a wave optics problem.
- The *transmittivity* and *reflectivity* of the substrate/air interface.

Once the substrate radiation pattern is known, the air radiation pattern can be evaluated according to

$$X_j^{\mathrm{air}}(\lambda, \beta_{\mathrm{air}}) = T_j^{\mathrm{air}}(\lambda, \beta_{\mathrm{sub}})\, X_j^{\mathrm{sub}}(\lambda, \beta_{\mathrm{sub}})\, \frac{\mathrm{d}\beta_{\mathrm{sub}}}{\mathrm{d}\beta_{\mathrm{air}}} \tag{1.6}$$

with

$$n_{\mathrm{sub}} \sin \beta_{\mathrm{sub}} = \sin \beta_{\mathrm{air}} \tag{1.7}$$

and

$$\frac{\mathrm{d}\beta_{\mathrm{sub}}}{\mathrm{d}\beta_{\mathrm{air}}} = \frac{\cos \beta_{\mathrm{air}}}{n_{\mathrm{sub}} \cos \beta_{\mathrm{sub}}}, \tag{1.8}$$

where β_{air} and β_{sub} are the respective propagation angles in air and in the substrate, $T_j^{\mathrm{air}}(\lambda, \beta_{\mathrm{sub}})$ is the transmittance of light rays with polarization j from the substrate into the air and n_{sub} is the substrate refractive index.

For a planar OLED stack, the molecular emission (see section 1.3.2) and thereby the initial substrate pattern $X_j^{\mathrm{sub},0}$ can be modelled in closed form up to the numerical solution of a one-dimensional integral [79, 80]. The reflectivity $R_j^{\mathrm{oled}}(\lambda, \beta)$ of the OLED stack is a function of the wavelength and propagation angle and polarization, and can be evaluated by means of the transfer matrix method or the scattering matrix method (see section 2.4). Finally, the reflectivity $R_j^{\mathrm{air}}(\lambda, \beta)$ at the substrate/air interface is simply given by the Fresnel formula, and the transmittivity into air is $T_j^{\mathrm{air}}(\lambda, \beta) = 1 - R_j^{\mathrm{air}}(\lambda, \beta)$.

Then, the forward and backward propagating radiation patterns are connected by the following equations:

$$X_j^{\mathrm{sub}}(\lambda,\beta) = \begin{cases} R_j^{\mathrm{air}}(\lambda,\beta)\, X_j^{\mathrm{sub}}(\lambda,\pi-\beta) & \text{for } 0 \le \beta \le \pi/2 \\ X_j^{\mathrm{sub,0}}(\lambda,\beta) + R_j^{\mathrm{oled}}(\lambda,\beta)\, X_j^{\mathrm{sub}}(\lambda,\pi-\beta) & \text{for } \pi/2 < \beta \le \pi \end{cases} \tag{1.9}$$

1.3.2. Molecular luminescence in a photonic environment

Molecular luminescence is a quantum mechanical problem, and the interaction of light and matter inside a thin-film system can be studied in the framework of cavity quantum electrodynamics. However, for the optical modeling of OLEDs, a description in terms of classical electrodynamics is more appropriate in most cases. In the following, I want to briefly sketch both approaches. The aim is to show how the classical model is related to the quantum mechanical picture and where are the conceptual and the practical limitations of the classical and the quantum approach, respectively.

1.3.2.1. Quantum-mechanical description

The decay of an excited molecular state $|e\rangle$ into a lower energy state $|g\rangle$ under the creation of a photon $|\gamma_\mu\rangle$ is a quantum mechanical transition, called *spontaneous emission*:

$$|e\rangle \rightarrow |g,\gamma_\mu\rangle \tag{1.10}$$

In the so called minimal coupling treatment, the electronic states of the excited and the relaxed molecule are treated as quantum states, whereas the generated photon enters the picture as an external field $\mathbf{E}_\mu(\mathbf{r})$.

In first order perturbation theory, the transition rate is given by Fermi's Golden Rule [81,82],

$$\Gamma(e,g) = \frac{2\pi}{\hbar^2} \sum_\mu \left| \langle g|\hat{H}_\mu|e\rangle \right|^2 \delta(\omega_\mu - \omega_{eg}), \tag{1.11}$$

where $\hat{H}_\mu$ is the perturbation Hamilton operator for the photon state $|\gamma_\mu\rangle$, and ω_μ and ω_{eg} are the frequencies that correspond to the photon energy and the energy difference between the molecular states $|e\rangle$ and $|g\rangle$, respectively. The sum runs over all photon states, indexed by μ.

In dipole approximation, the interaction Hamilton operator H_μ reads

$$H_\mu = q\hat{\mathbf{r}} \cdot \mathbf{E}_\mu, \tag{1.12}$$

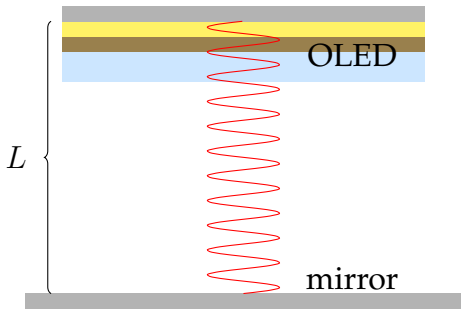

Figure 1.7. – Regularization of photonic states: OLED between hypothetic perfect electric conductors

where q stands for the elementary charge and $\hat{\mathbf{r}}$ denotes the electronic position operator. We can thus write

$$\Gamma(e,g) = \frac{2\pi q}{\hbar^2} \sum_{\mu} |\mathbf{d}_{eg} \cdot \mathbf{E}_{\mu}(\mathbf{r}_0)|^2 \delta(\omega_{\mu} - \omega_{eg}). \tag{1.13}$$

In the above,

$$\mathbf{d}_{eg} = \langle g|\hat{\mathbf{r}}|e\rangle \tag{1.14}$$

denotes the transition dipole moment of the transition from state $|e\rangle$ into $|g\rangle$ and $\mathbf{r}_0$ is the location of the emitting molecule [3].

When modeling photon emission inside a photonic environment (like planarly layered media), the idea is to replace the electric field of the free-space photon (a plane wave), by a solution of Maxwell's equations for the system at hand.

The actual total transition rate Γ cannot be determined theoretically without considering the wavefunctions of the electronic states $|e\rangle$ and $|g\rangle$. However, in many situations it is more important to assess the relative transition rate $\Gamma_{\mu}(e,g)/\Gamma(e,g)$, that is the share of excited photons in some collection of states $\{|\gamma_{\mu}\rangle \, | \mu \in \Omega\}$ relative to the total number of excited photons. And the relative transition rate can be evaluated knowing only the orientation of the transition dipole moment. Setting

$$\mathbf{d}_{eg} = |\mathbf{d}_{eg}|\hat{\mathbf{e}}_{eg}, \tag{1.15}$$

one can write

$$\frac{\Gamma_{\Omega}(e,g)}{\Gamma(e,g)} = \frac{\sum_{\mu\in\Omega} |\hat{\mathbf{e}}_{eg} \cdot \mathbf{E}_{\mu}(\mathbf{r}_0)|^2}{\sum_{\mu} |\hat{\mathbf{e}}_{eg} \cdot \mathbf{E}_{\mu}(\mathbf{r}_0)|^2}. \tag{1.16}$$

[3] Here we have used that the wavelength of the photon is large compared to the molecule size, such that $\mathbf{E}_{\mu}(\mathbf{r}) \approx \mathbf{E}_{\mu}(\mathbf{r}_0)$.

A priori, it is not clear how the sum in the above expression shall be evaluated, as the set of photonic modes in an unbounded volume is not countable. The trick is to imagine the photonic environment (e.g., the thin film system) between a pair of perfectly conducting metallic plates[4] (see figure 1.7), and consider the limit of the distance L between those plates tending towards infinity [83]. The number of modes fitting into this 1D cavity scales proportional to L. At the same time, the mode profile $\mathbf{E}_\mu(\mathbf{r})$ needs to be scaled such that the energy in the respective mode is constant (as it corresponds to ω_{eg}). As the total energy is porportional to $\int \mathrm{d}^3\mathbf{r}|\mathbf{E}_\mu|^2$, $|\mathbf{E}_\mu|^2$ scales as L^{-1}, such that the sum in (1.16) takes a well-defined value in the limit $L \to \infty$, compare [84].

One can thus model the outcoupling efficiency of an OLED by following these steps:

1. Use the transfer matrix method (see chapter 2.4) to evaluate the mode profile $\mathbf{E}_\beta(z)$ for a list of radiation modes, indexed by the polar angle of propagation β. These are nothing else than a reflected plane wave, incident under polar angle β. The density of states as well as the normalization of the mode profile are obtained using the above described regularization scheme.
2. Calculate the waveguide modes supported by the layered medium. Here, the regularization scheme with the metallic box is not necessary, as the waveguide modes are countable with regard to the polar direction and their energy is confined to the thin film system.
3. Use (1.16) to obtain the relative transition rate into each of these modes. The outcoupling efficiency would correspond to the relative transition rate $\Gamma_\Omega(e,g)/\Gamma(e,g)$ where Ω is the set of all radiative states (as opposed to the waveguided).

The above described formalism can yield accurate results for lossless media. But in the case of optical losses, it is not well defined. In particular, the near-field coupling to metal layers is not estimated correctly [85]. Despite this drawback, the quantum mechanical approach has been used for the optical modeling of planar OLEDs in a couple of publications [85–87].

1.3.2.2. Classical description

In the framework of classical electrodynamics, molecular luminescence can be described by identifying the emitter with a monochromatic point dipole source [79, 88, 89], that is an external current distribution of the form

$$\mathbf{j}(\mathbf{r}) = -\mathrm{i}\omega\delta(\mathbf{r}-\mathbf{r}_0)\mathbf{d}_{eg}, \tag{1.17}$$

[4] For OLEDs with reflecting electrode, consider a single perfectly conducting plate in opposition to the OLED.

where $\mathbf{d}_{eg}$, as before, denotes the electric dipole moment associated with the molecular decay. A harmonic time dependency of $\exp(-\mathrm{i}\omega t)$ is implicitly understood for all fields, where as before, the angular frequency $\omega = \omega_{eg}$ corresponds to the energy difference between excited molecular state and ground state. The electric power dissipated by the time-harmonic current distribution is [89]

$$\begin{aligned} P_{\mathrm{dip}} &= -\frac{1}{2}\int_{\mathbb{R}^3} \mathrm{d}^3\mathbf{r}\ \mathrm{Re}\left(\mathbf{j}^*(\mathbf{r})\cdot\mathbf{E}(\mathbf{r})\right) \\ &= \frac{\omega}{2}\,\mathrm{Im}\left(\mathbf{d}_{eg}^*\cdot\mathbf{E}(\mathbf{r}_0)\right). \end{aligned} \tag{1.18}$$

The above just describes that a current performs work against the electric field that it generates, and $\mathbf{E}(\mathbf{r}_0)$ includes both, the dipole's primary field as well as the response from the photonic environment[5]. According to Poynting's theorem, the electric power dissipated by the dipole source equals the radiated electromagnetic power.

In order to model the outcoupling efficiency of an OLED, the following steps are followed:

1. Compute the electromagnetic fields by solving Maxwell's equations for an external current distribution (1.17). This can be achieved by expanding the field of the dipole source in terms of cylindrical waves [79, 91] or plane waves [92], and employ the transfer matrix scheme or the scattering matrix scheme (see chapter 2.4) to propagate the partial waves through the layer stack.
2. Evaluate the total dissipated power P_{dip} of the dipole using (1.18).
3. Evaluate the electromagnetic outcoupled power and the far field intensity as will be explained in section 2.3.1.2. The ratio between the emitted power and the total dissipated power yields the outcoupling efficiency.

The classical treatment has been demonstrated to yield relative life time predictions in very good agreement to experimental observations, see [79]. It is valid also for lossy materials[6] and the near-field coupling to metal layers is treated accurately[7]. For that reason, the classical model is the state of the art for optical OLED modeling in the academic [93] as well as in the industrial sector. Commercial software products are available on the market, for example Setfos by FLUXIM [94].

[5] As the dipole's dissipated power models the decay rate of the luminescent molecule, we can see at this point that the latter depends on the photonic environment of the molecule. This result that might seem counter-intuitive at first sight is called the *Purcell effect* [90].

[6] With one exception: Absorption in the emitter layer cannot be considered. It would lead to an infinite decay rate due to absorption of the singular near field

[7] The mathematical treatment of surface plasmon polariton modes was introduced by Arnold Sommerfeld who studied their radio-frequency analogs in his seminal paper "Über die Ausbreitung der Wellen in der drahtlosen Telegraphie" [91]

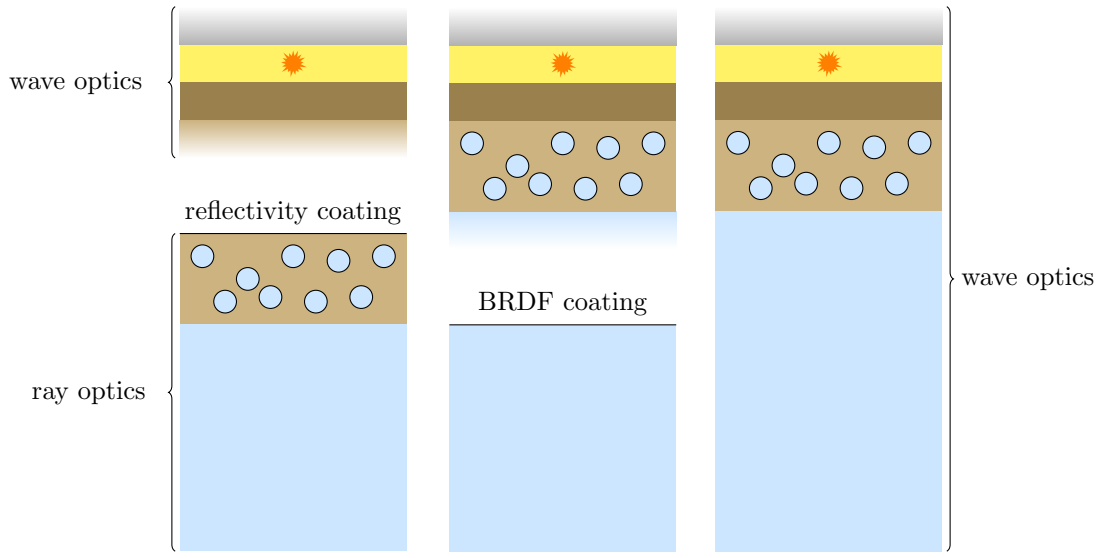

Figure 1.8. – Modeling approaches for OLEDs with internal disordered scattering layers.

1.3.3. Internal disordered scattering layers (state of the art)

Internal disordered scattering layers in OLEDs break the transverse translational symmetry, such that a closed form computation of the extraction pattern is no longer feasible. In this section, I want to briefly discuss numerical approaches that have instead been applied to this problem. First, it is worth noting that the computation of the extraction efficiency is a statistical problem, and numerical simulations will in one or the other way need to address the probabilistic nature of disordered scattering layers. Secondly, simulation strategies can be distinguished by how they treat light scattering – coherently or incoherently? In other words, is the electromagnetic field or the electromagnetic intensity the central quantity of the scattering calculation?

1.3.3.1. Incoherent and coherent scattering

For *volumetric* nano particle based scattering layers, the most popular modeling technique is to follow an incoherent Monte-Carlo approach [24, 95, 96] or to solve the radiative transfer equation (RTE) [97, 98] for the propagation in the scattering layer (compare the left picture in figure 1.8). The initial emission from the OLED layer system into the scattering layer can be computed using the standard modeling formalism for flat OLEDs, see section 1.3.2.2, whereas the reflectivity for light rays hitting the OLED thin film system can be evaluated by means of the transfer matrix formalism, see chapter 2.4. With this approach, the statistical nature of the scattering layer is automatically accounted for and the overall computational effort is low.

One issue with this method is that for compact scattering layers with smaller interparticle distances it can be expected that coherent multiple scattering effects become

significant [99], such that an incoherent treatment does no longer yield an accurate estimate of the extraction pattern. In fact, the thicknesses of experimentally realized volumetric scattering layers reported in literature vary from several ten microns [18, 64] over a couple of microns [62,67] to a few hundred nanometers [59,66]. In addition, it is not straightforward to include evanescent wave scattering (like the extraction of surface plasmon polariton modes) within the incoherent framework.

On the other hand, many publications that deal with the simulation of *flat* scattering layers in OLEDs treat the whole OLED stack including the substrate in a wave optics simulation (see the right of figure 1.8). The extraction pattern into air can then directly be evaluated by monitoring the electromagnetic power flux through the substrate air interface [47, 48, 68]. In order to meet the probabilistic nature of the scattering layer, ensemble averages over the random particle configuration or at least over the dipole position relative to the scattering particles need to be computed by repeated simulations.

A drawback of the full wave optics approach is that the substrate is usually modeled with an unrealistically low thickness, the effect of which on the estimated extraction pattern is not clear and should at least be averaged over by varying the substrate layer thickness.

The most rigorous (but also most expensive) approach is to treat the OLED thin film system including the scattering layer in a wave optics picture, and to address only light propagation in the substrate with a ray optics treatment (compare the middle picture of figure 1.8) [78].

First, one computes the initial radiation pattern $X_j^{\mathrm{sub},0}$ from the OLED stack with scattering layer into the substrate by means of wave optics simulations, see chapter 5 or [78]. Further, the reflectivity at the OLED stack[8] (with scattering layer) is modeled by means of a *bidirectional reflectance distribution function* (BRDF), the calculation of which is again based on wave optics simulations [78].

Assuming that the OLED is azimuthally isotropic (i.e., there is no preferred azimuthal direction in the scattering structure or the emitter molecules), a bookkeeping of the polar propagation angle is then sufficient to describe the light field in the substrate, and in that spirit one can define the *polar BRDF* by the relation

$$R_{j,j'}^{\mathrm{oled}}\left(\lambda,\beta,\beta'\right)=\Phi_{\mathrm{inc}}^{-1}\frac{\mathrm{d}\Phi_{j,\mathrm{refl}}}{\mathrm{d}\beta} \tag{1.19}$$

where

- Φ_{inc} is the radiant flux of a light ray with polar propagation angle β' and polarization j' that is incident on the OLED from the substrate

[8] In the case of external micro-structures, one can also use a *bidirectional scattering distribution function* for the substrate/air interface, which can be obtained by means of ray tracing simulations. However, in this work only planar substrate/air interfaces are considered.

- $\Phi_{j,\mathrm{refl}}$ is the j-polarized part of the radiant flux reflected back into the substrate (diffuse and specular reflection).

The second case of (1.9) (the case of $\pi/2 \leq \beta \leq \pi$) is then replaced by

$$X_j^{\mathrm{sub}}(\lambda,\beta) = X_j^{\mathrm{sub},0}(\lambda,\beta) + \sum_{j'} \int_0^{\pi/2} \mathrm{d}\beta' R_{j,j'}^{\mathrm{oled}}(\lambda,\beta,\beta') X_{j'}^{\mathrm{sub}}(\lambda,\beta') . \tag{1.20}$$

to compute the substrate radiation pattern and from that the extraction pattern according to (1.6).

1.3.3.2. Wave optics computational approaches

The simulation of the light extraction pattern within the coherent approach involves the solution of one or multiple wave optics problems for scattering centers inside a planarly layered background medium. The wave optics problem has a unique exact solution, and the task is to numerically construct an approximation to that solution. A variety of computational approaches has been suggested in literature, and the selection of an appropriate strategy depends on the desired accuracy, the complexity of the problem, symmetries, availability of computer codes, and personal taste.

Following [100], we can distinguish between[9] *differential approaches*, *integral approaches* and *series approaches*.

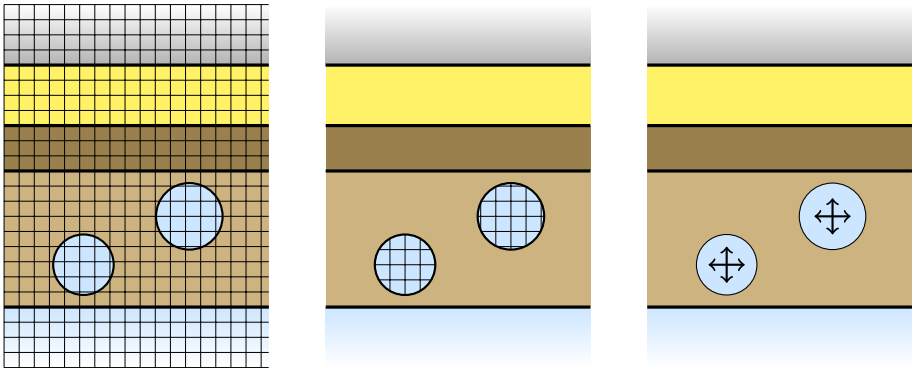

Figure 1.9. – Computational wave optics approaches for particles inside a stratified medium. In the differential approach (left), the whole geometry is discretized. In the integral approach (middle), only the particle volumes or surfaces need to be discretized, whereas the propagation in the layered background medium is treated analytically. In the T-matrix method (a representative of the series approach) (right), the scattered field is expanded in multipoles.

[9] For completeness, treatments on the basis of *perturbation theory* have also been published [101].

Differential approach The differential approach aims at the direct solution of the Helmholtz equation, (see section 2.1). Typical examples are

- the Finite-Difference Time Domain (FDTD) Method [102]
- the Finite-Element Method (FEM) [103].

These methods are most flexible and can be applied to complex geometries. Commercial [104–106] and free [107] computer codes are available. It seems that currently, the FDTD method is most popular for the simulation of OLEDs with internal scattering layers [42, 45, 47, 68, 87, 108–110], whereas only few papers are based on the FEM [111].

Integral approach In the integral approach, the Helmholtz equation is rewritten in terms of an integral equation [112], coupling the electromagnetic fields with an induced current distribution through the Green's function of the Helmholtz equation, see section 2.2. Methods that fall into this class include

- the volume integral equation (VIE) approach [113] which is related to the the discrete dipole approximation (DDA) [114]. In a scattering problem, only the scattering particle needs to be discretized, whereas the propagation in the surrounding medium is treated analytically. This can be regarded as an advantage over the FDTD and FEM methods. However, the drawback is that the system of linear equations for the VIE or DDA approach is dense as compared to the sparse interaction matrices in the FEM.
- the boundary element method (BEM) [115]. In contrast to the VIE approach, the fields emerging from the induced current sources inside the scatterer are represented by equivalent surface currents.

These volume integral or surface integral methods have in common that they rely on the Green's function formalism. Scattering particles inside a layered medium can thus be treated by replacing the free-space Green's function with the layered-medium Green's function, thereby avoiding the need to discretize the background geometry [116, 117]. It seems that the integral approach has been applied only rarely to the simulation of scattering layers in OLEDs [118].

Series approach Finally, the class of series approaches is given by methods where space is partitioned into domains of constant refractive index, and the solution of the Helmholtz equation is written as a series of basis solution functions in each of these domains. The coefficients of these series expansions are calculated from a linear system of equations that exploits the continuity condition of the respective series expansions across a domain boundary. A discretization of the geometry is not necessary, and by a wise choice of the basis functions, an accurate representation of the

scattered field can often be achieved with a small number of parameters. Methods that fall into this category include

- methods that are based on the expansion of the scattered field in plane waves, also called the *rigorous coupled wave analysis* (RCWA) [119, 120]. This method is well suited for rectangular periodic geometries and has been applied to the problem of light extraction from OLEDs in some publications [109, 121, 122].
- a method based on the expansion of the scattered field in cylindrical waves [123–125]. Although this approach seems very promising, it has not yet been applied to scattering layers in organic light emitting diodes. The reason is probably that this method is relatively unknown and computer codes seem not to be available.
- a method based on the expansion of the scattered field in spherical waves and plane waves, also called the *T-matrix method* [2, 4–6]. It has been applied to scattering layers in OLEDs in a few publications [3, 78, 126, 127] and will be the main subject of this thesis.

2. Electromagnetic waves

This chapter introduces some basic concepts of electromagnetic wave propagation that are needed for the treatment of scattering by particles in a thin film system. After briefly recalling the wave equation of the electric field and the definition of the dyadic Green's function (sections 2.1 and 2.2), the plane and spherical vector wave functions are introduced in section 2.3, and the transformation of the one kind into the other is discussed. The section on plane vector wave functions also includes the definition of a beam with Gaussian transverse footprint and gives the expansion of the according electric field in plane waves. Finally, section 2.4 provides an extensive treatment of wave propagation in stratified media, including the important case of excitations from within.

2.1. The wave equation

Throughout this thesis, I assume that all media are non-magnetic, linear, local, piecewise homogeneous and isotropic. In the context of optoelectronic thin film devices like OLEDs, the last of these assumptions is not always justified, as some commonly used materials show a significant optical anisotropy. It is possible to extend the here presented treatment to the case of anisotropic materials [128], but for simplicity I just assume isotropy.

Monochromatic solutions [1]

$$\mathbf{E}(t,\mathbf{r}) = \mathbf{E}(\mathbf{r})\,\mathrm{e}^{-\mathrm{i}\omega t} \tag{2.1}$$

$$\mathbf{H}(t,\mathbf{r}) = \mathbf{H}(\mathbf{r})\,\mathrm{e}^{-\mathrm{i}\omega t} \tag{2.2}$$

of the Maxwell's equations can then be constructed by first solving the system [89, 129]

$$\boldsymbol{\nabla}\times\boldsymbol{\nabla}\times\mathbf{E}(\mathbf{r}) - k^2\mathbf{E}(\mathbf{r}) = \mathrm{i}\omega\mu_0\mathbf{j} \tag{2.3}$$

$$\boldsymbol{\nabla}\cdot\mathbf{E}(\mathbf{r}) = \frac{\rho}{\varepsilon\varepsilon_0} \tag{2.4}$$

and then let

$$\mathbf{H}(\mathbf{r}) = \frac{1}{\mathrm{i}\omega\mu_0}\boldsymbol{\nabla}\times\mathbf{E}(\mathbf{r})\,. \tag{2.5}$$

[1] This is not a restriction, as a general time-dependent field can be expanded in monochromatic fields by means of a Fourier transform.

In the above, k is the wavenumber in the respective medium containing $\mathbf{r}$,

$$k = \frac{n\omega}{c}, \tag{2.6}$$

μ_0 is the vacuum permeability, $\mathbf{j}(\mathbf{r})$ is a time-harmonic source current in the sense of equations (2.1) and (2.2), $\rho(\mathbf{r})$ is a time-harmonic source charge density distribution, ε and ε_0 are the relative permittivity of the medium at angular frequency ω and the vacuum permittivity, respectively, c is the vacuum speed of light and

$$n = \sqrt{\varepsilon + \mathrm{i}\sigma/(\omega\varepsilon_0)}, \tag{2.7}$$

is the complex refractive index, where σ is the conductivity of the medium at angular frequency ω.

In a source-free domain, equations (2.3) and (2.4) reduce to the homogeneous Helmholtz equation for a divergence-free field:

$$\left(\nabla^2 + k^2\right)\mathbf{E}(\mathbf{r}) = \mathbf{0} \tag{2.8}$$

$$\boldsymbol{\nabla}\cdot\mathbf{E}(\mathbf{r}) = 0. \tag{2.9}$$

At an interface between two media, the fields fulfill the transmission boundary conditions

$$\begin{aligned}\hat{\mathbf{n}}\times(\mathbf{E}(\mathbf{r}) - \mathbf{E}'(\mathbf{r})) &= \mathbf{0}\\ \hat{\mathbf{n}}\times(\mathbf{H}(\mathbf{r}) - \mathbf{H}'(\mathbf{r})) &= \mathbf{0},\end{aligned} \tag{2.10}$$

where $\mathbf{E}(\mathbf{r})$, $\mathbf{H}(\mathbf{r})$ and $\mathbf{E}'(\mathbf{r})$, $\mathbf{H}'(\mathbf{r})$ denote the fields at either side of the interface and $\hat{\mathbf{n}}$ is the unit normal vector of the interface. Finally, a radiation condition is required in order to distinguish between waves of outgoing and incoming type, respectively. This is ensured by the Silver-Müller radiation condition [129]

$$\lim_{|\mathbf{r}|\to\infty}\left(\sqrt{\varepsilon_0}\mathbf{E}(\mathbf{r})\times\mathbf{r} + |\mathbf{r}|\sqrt{\mu_0}\mathbf{H}(\mathbf{r})\right) = \mathbf{0}. \tag{2.11}$$

2.2. Dyadic Green's function

The dyadic Green's function is an operator that maps a given point current source to the resulting electric field. It is a matrix-valued function of two positions, $\mathbf{r}$ (the field position) and $\mathbf{r}'$ (the source position). It obeys the relations

$$\boldsymbol{\nabla}\times\boldsymbol{\nabla}\times\mathbf{G}(\mathbf{r},\mathbf{r}') - k^2\mathbf{G}(\mathbf{r},\mathbf{r}') = \mathbf{I}_3\delta(\mathbf{r}-\mathbf{r}') \tag{2.12}$$

$$\lim_{|\mathbf{r}|\to\infty}\left(\sqrt{\varepsilon_0}\mathbf{G}(\mathbf{r},\mathbf{r}')\times\mathbf{r} + \frac{|\mathbf{r}|}{\mathrm{i}\omega\sqrt{\mu_0}}\boldsymbol{\nabla}\times\mathbf{G}(\mathbf{r},\mathbf{r}')\right) = \mathbf{0} \tag{2.13}$$

with $\mathbf{I}_3$ denoting the unit matrix. Then, for an arbitrary source current distribution $\mathbf{j}$, the electric field reads

$$\mathbf{E}(\mathbf{r}) = \mathrm{i}\omega\mu_0\int_{\mathbb{R}^3}\mathrm{d}^3\mathbf{r}'\mathbf{G}(\mathbf{r},\mathbf{r}')\cdot\mathbf{j}(\mathbf{r}'). \tag{2.14}$$

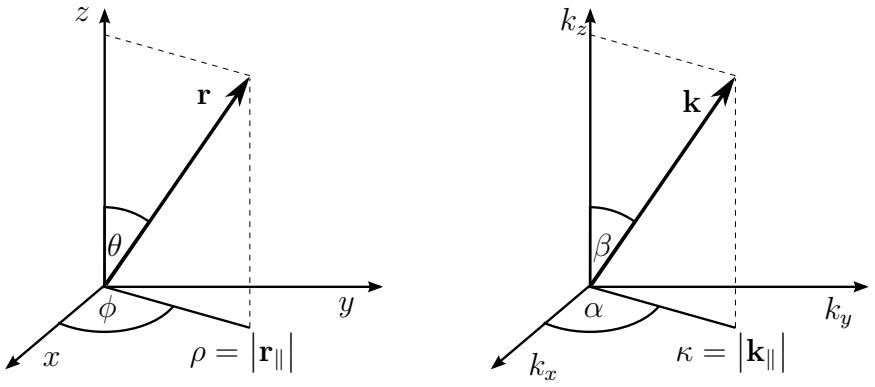

Figure 2.1. – Coordinate systems for vectors in position space and in reciprocal space.

	$\mathbf{r}$	$\mathbf{k}$
Cartesian	(x, y, z)	(k_x, k_y, k_z)
Cylindrical	(ρ, ϕ, z)	(κ, α, k_z)
Spherical	(r, θ, ϕ)	(k, β, α)

Table 2.1. – Notation for Cartesian, cylindrical and spherical coordinates of $\mathbf{r}$ and $\mathbf{k}$.

2.3. Vector wave functions

In the spirit of what can be called the *series approach* to the numerical solution of electromagnetic scattering problems [100], the field in a domain of constant refractive index is expanded in terms of basis solutions to the Helmholtz equation. Namely, I will employ the *plane vector wave functions* (PVWFs) and the *spherical vector wave functions* (SVWFs). These basis sets are constructed from the Helmholtz equation by a separation of variables for the Cartesian and the spherical coordinate system, respectively [130].

Vectors $\mathbf{r}$ in configuration space and vectors $\mathbf{k}$ in reciprocal space will be represented in cartesian, cylindrical and spherical coordinates. Figure 2.1 and table 2.1 give an overview on the notation used in this work for the respective coordinates.

2.3.1. Plane vector wave functions

The plane vector wave functions in a medium with refractive index n and wavenumber $k = n\omega/c$ are given by

$$\mathbf{\Phi}_j^{\pm}(\kappa, \alpha; \mathbf{r}) = \mathrm{e}^{\mathrm{i}\mathbf{k}^{\pm}\cdot\mathbf{r}}\hat{\mathbf{e}}_j^{\pm}. \tag{2.15}$$

Here $\hat{\mathbf{e}}_j^{\pm}$ denotes the unit vector in the azimuthal direction for $j = 1$ (TE-polarization) and the unit vector in the polar direction for $j = 2$ (TM-polarization) at $\mathbf{k} = \mathbf{k}^{\pm}$,

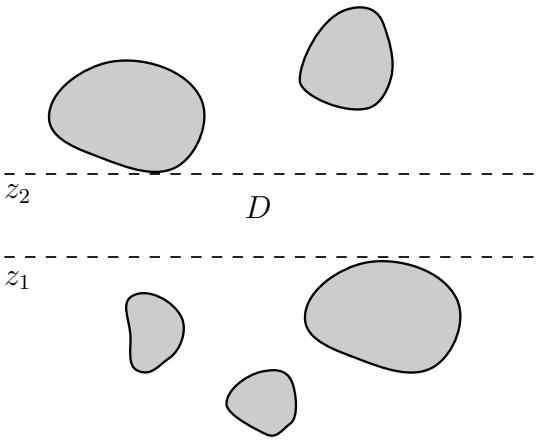

Figure 2.2. – In a homogeneous domain D bounded by two z-planes, every solution of the homogeneous Maxwell's equations can be expanded in plane waves.

where $\mathbf{k}^{\pm}$ is the wave vector given by the cylindrical coordinates $(\kappa, \alpha, \pm k_z)$ and k_z is a function of κ,

$$k_z = \sqrt{k^2 - \kappa^2}, \tag{2.16}$$

ensuring $|\mathbf{k}| = k$. As the square root is double-valued, the following convention is employed to pick one well-defined value:

$$\begin{array}{ll} \operatorname{Re} k_z \geq 0 & \text{if } \operatorname{Im} k_z = 0 \\ \operatorname{Im} k_z > 0 & \text{else.} \end{array} \tag{2.17}$$

In vacuum or in a dielectric medium, i.e., when the refractive index n is real, k_z is a real number for $\kappa \leq k$. Then, the amplitude of the PVWFs is an oscillating function of all three components of the position vector $\mathbf{r}$. The PVWF marked with a plus sign, $\mathbf{\Phi}_j^+$, correspond to waves propagating in the positive z-direction, whereas the minus sign in $\mathbf{\Phi}_j^-$ indicates a propagation into the negative z-direction.

For $\kappa > k$, k_z is imaginary, such that $\mathbf{\Phi}_j^{\pm}$ is an exponential function of z. This is called an *evanescent wave*. Then, the square root convention (2.17) ensures that $\mathbf{\Phi}_j^+$ decays in the positive z-direction whereas $\mathbf{\Phi}_j^-$ decays in the negative z-direction.

2.3.1.1. Completeness

In this thesis, I assume without proof[2] that the set of PVWFs, including the evanescent waves, is complete in the following sense:

If a domain $D \subset \mathbb{R}^3$ is

- bounded by two z-planes, i.e., $D = \{\mathbf{r} | z_1 \leq z \leq z_2\}$ with $-\infty \leq z1 < z_2 \leq \infty$ (see figure 2.2),

[2]For a rigorous analysis of the plane-wave spectrum representation, see [131].

- source-free and homogeneous, i.e., filled with a material (or vacuum) of constant refractive index,

and $\mathbf{E}(\mathbf{r})$ is a field that

- is divergence-free,
- fulfills the Helmholtz equation for $\mathbf{r} \in D$,

then there exist functions $g_1^{\pm}(\kappa, \alpha)$ and $g_2^{\pm}(\kappa, \alpha)$ such that for $\mathbf{r} \in D$

$$\mathbf{E}(\mathbf{r}) = \sum_{j=1}^{2} \int_{\mathbb{R}^2} \mathrm{d}^2\mathbf{k}_\parallel \left(g_j^+(\kappa,\alpha)\mathbf{\Phi}_j^+(\kappa,\alpha;\mathbf{r}) + g_j^-(\kappa,\alpha)\mathbf{\Phi}_j^-(\kappa,\alpha;\mathbf{r}) \right) \tag{2.18}$$

$$= \sum_{j=1}^{2} \int_{\mathbb{R}^2} \mathrm{d}^2\mathbf{k}_\parallel \left[\mathbf{\Phi}_j^+(\kappa,\alpha;\mathbf{r}), \mathbf{\Phi}_j^-(\kappa,\alpha;\mathbf{r}) \right] \cdot \begin{bmatrix} g_j^+(\kappa,\alpha) \\ g_j^-(\kappa,\alpha) \end{bmatrix}, \tag{2.19}$$

where $\mathrm{d}^2\mathbf{k}_\parallel$ is a short-hand notation for $\mathrm{d}k_x \mathrm{d}k_y = \mathrm{d}\kappa\, \kappa\, \mathrm{d}\alpha$. In the second line of the above equation, I have introduced a two-vector notation for the coefficients of the forward and backward going waves for later convenience.

If $z_1 = -\infty$, i.e., all sources and inhomogeneities are located above z_2, then $g_j^+(\kappa, \alpha)$ must vanish for all (κ, α) in order to fulfill the Silver-Müller radiation condition. Analogously, for $z_2 = \infty$ we have $g_j^-(\kappa, \alpha) = 0$. In either of these cases, the plane-wave spectrum is uniquely determined if we know the electric field at a single z-surface, the so-called *scan plane* [131].

2.3.1.2. Energy flux through a z-surface

The time-averaged electromagnetic power of a monochromatic field radiated through a surface $z = \mathrm{const}$ can be evaluated using the complex Poynting vector:

$$\langle P(z) \rangle = \mathrm{Re} \int_{\mathbb{R}^2} \mathrm{d}^2\mathbf{r}_\parallel\, \mathbf{S}(\mathbf{r}) \cdot \hat{\mathbf{e}}_z \tag{2.20}$$

with

$$\mathbf{S}(\mathbf{r}) = \frac{1}{2}\mathbf{E}(\mathbf{r}) \times \mathbf{H}^*(\mathbf{r}). \tag{2.21}$$

Inserting (2.18) into (2.5), one can see after a lengthy derivation (see Appendix A):

$$\langle P(z) \rangle = \frac{2\pi^2}{\omega\mu_0} \sum_{j=1}^{2} \int_{\mathbb{R}^2} \mathrm{d}^2\mathbf{k}_\parallel \Big\{ \mathrm{Re}(k_z) \left(\left| g_j^+(\kappa,\alpha) \right|^2 - \left| g_j^-(\kappa,\alpha) \right|^2 \right) - 2\,\mathrm{Im}(k_z)\, \mathrm{Im}\left(g_j^+(\kappa,\alpha) g_j^{-*}(\kappa,\alpha) \right) \Big\} \tag{2.22}$$

From (2.22) we can see that the PVWFs are *orthogonal* in the sense that the power flux through a z-surface only couples partial waves with the same j, κ and α.

In lossless dielectric media, k_z is real for $\kappa \leq k$ and purely imaginary for $\kappa > k$. Then, *forward and backward propagating waves* are decoupled with regard to energy flux through z-surfaces, whereas the near field contributes to the power flux through a *coupling of forward and backward decaying evanescent waves*. As a consequence, an isolated object cannot radiate electromagnetic power through the near field.

In fact, in a dielectric medium above all sources and sinks, g_j^- must vanish, and we can write

$$\langle P_{\mathrm{top}} \rangle = \frac{2\pi^2}{\omega\mu_0} \sum_{j=1}^{2} \int_{|\mathbf{k}_\parallel| \leq k} \mathrm{d}^2\mathbf{k}_\parallel k_z \left| g_j^+(\kappa, \alpha) \right|^2, \tag{2.23}$$

whereas below all sources and sinks,

$$\langle P_{\mathrm{bot}} \rangle = -\frac{2\pi^2}{\omega\mu_0} \sum_{j=1}^{2} \int_{|\mathbf{k}_\parallel| \leq k} \mathrm{d}^2\mathbf{k}_\parallel k_z \left| g_j^-(\kappa, \alpha) \right|^2. \tag{2.24}$$

I compare this expression to the definition of the far field radiant intensity $I_{\Omega,j}$:

$$\langle \Phi \rangle = \sum_{j=1}^{2} \int \mathrm{d}^2\Omega \, I_{\Omega,j}(\beta, \alpha), \tag{2.25}$$

where $\langle \Phi \rangle$ is the time-averaged total radiant flux and $\Omega = (\beta, \alpha)$ is the solid angle. Thus,

$$I_{\Omega,j}(\beta, \alpha) = \frac{2\pi^2}{\omega\mu_0} k k_z^2 \begin{cases} \left| g_j^+(\kappa, \alpha) \right|^2 & \text{for } \beta \in \left[0, \frac{\pi}{2}\right] \\ \left| g_j^-(\kappa, \alpha) \right|^2 & \text{for } \beta \in \left[\frac{\pi}{2}, \pi\right] \end{cases}, \tag{2.26}$$

for $\kappa = k \sin\beta$. In the above, $\mathrm{d}^2\mathbf{k}_\parallel = \pm k k_z \mathrm{d}^2\Omega$ has been used.

2.3.1.3. Expansion of the dyadic Green's function in PVWFs

The dyadic Green's function can be expanded in terms of plane waves [132]:

$$\mathbf{G}(\mathbf{r}, \mathbf{r}') = \frac{\mathrm{i}}{8\pi^2} \sum_{j=1}^{2} \int_{\mathbb{R}^2} \mathrm{d}^2\mathbf{k}_\parallel \frac{1}{k_z} \, \mathbf{\Phi}_j^{\pm}(\kappa, \alpha; \mathbf{r}) \otimes \mathbf{\Phi}_j^{\pm\dagger}(\kappa, \alpha; \mathbf{r}') \qquad \text{for } z \gtrless z', \tag{2.27}$$

where $\otimes$ denotes the (dyadic) tensor product[3] and the daggered PVWFs $\mathbf{\Phi}_j^{\pm\dagger}$ are defined by replacing the explicit i in (2.15) with $-\mathrm{i}$.

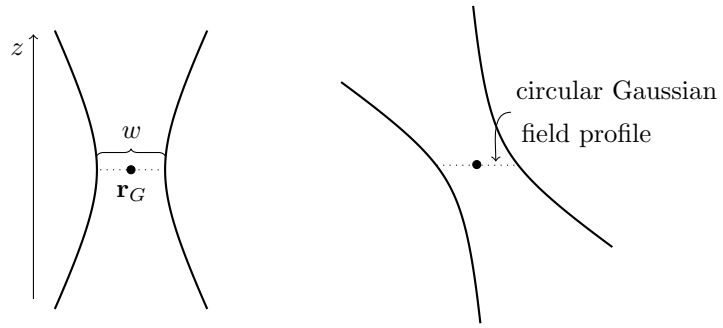

Figure 2.3. – Left: Gaussian beam. Right: Tilted "beam with Gaussian footprint".

2.3.1.4. Expansion of a Gaussian beam in PVWFs

A Gaussian beam, propagating parallel to the z-axis (either in positive or in negative z-direction) is characterized by the width w of the beam waist, the focus coordinates $\mathbf{r}_\mathrm{G} = (x_\mathrm{G}, y_\mathrm{G}, z_\mathrm{G})$ and the electric field amplitude vector $\mathbf{A}_\mathrm{G}$ (oriented in the xy-plane) in the focus. By definition, the transverse electric field profile in the focus plane $z = z_\mathrm{G}$ is then:

$$\mathbf{E}_G(\mathbf{r}) = \exp\left[-\frac{(x-x_G)^2 + (y-y_G)^2}{w^2}\right]\mathbf{A}_G \qquad \text{for } z = z_G. \tag{2.28}$$

In the angular spectrum representation [89] the field can be written as

$$\mathbf{E}_\mathrm{G}(\mathbf{r}) = \int_{\mathbb{R}^2} \mathrm{d}^2\mathbf{k}_\parallel \, \mathrm{e}^{\mathrm{i}\mathbf{k}^\pm\cdot\mathbf{r}}\mathbf{T}(k_x, k_y) \tag{2.29}$$

with

$$\mathbf{T}(k_x, k_y) = \frac{w^2}{4\pi}\exp\left[-(k_x^2 + k_y^2)\frac{w^2}{4} - \mathrm{i}\mathbf{k}^\pm\cdot\mathbf{r}_G\right]\mathbf{A}_G, \tag{2.30}$$

where, as usual, $\mathbf{k}^\pm$ is the wavevector with a z-component of $\pm\sqrt{k^2 - k_x^2 - k_y^2}$ and the plus or minus sign is selected for beams propagating in the positive or negative z-direction, respectively. Defining the polarization angle α_G and the beam amplitude A_G by the relation

$$\mathbf{A}_G = (-\sin\alpha_G\hat{\mathbf{e}}_x + \cos\alpha_G\hat{\mathbf{e}}_y)A_G, \tag{2.31}$$

the amplitude vector can be approximated as

$$\mathbf{A}_G \approx (\cos(\alpha - \alpha_\mathrm{G})\hat{\mathbf{e}}_\alpha + \sin(\alpha - \alpha_\mathrm{G})\hat{\mathbf{e}}_\beta)\, A_G$$

[3]Simply, $\mathbf{a}\otimes\mathbf{b}$ is an operator that maps $\mathbf{c} \mapsto \mathbf{a}(\mathbf{b}\cdot\mathbf{c})$.

for $\beta \approx 0$, such that (2.29) can be approximated as

$$\mathbf{E}_{\mathrm{G}}(\mathbf{r}) \approx \sum_{j=1}^{2} \int_{\mathbb{R}^2} \mathrm{d}^2\mathbf{k}_{\parallel} g^{\pm}_{G,j}(\kappa,\alpha)\mathbf{\Phi}^{\pm}_{j}(\kappa,\alpha;\mathbf{r}) \tag{2.32}$$

with

$$g^{\pm}_{G,j}(\kappa,\alpha) = \frac{A_G w^2}{4\pi} \mathrm{e}^{-\frac{w^2}{4}\kappa^2 - \mathrm{i}\mathbf{k}^{\pm}\cdot\mathbf{r}_G} (\cos(\alpha-\alpha_{\mathrm{G}})\delta_{j1} \pm \sin(\alpha-\alpha_{\mathrm{G}})\delta_{j2}). \tag{2.33}$$

Although the right hand side of (2.32) is only an approximation to (2.28), it exactly solves the Maxwell equations.

For oblique incident angles, we generalize (2.32) and (2.33) to the case of a *beam with Gaussian footprint*, that is, a beam with amplitude A_G that propagates along the solid angle $\Omega_G = (\beta_G, \alpha_G)$ with a beam polarization j_G, and that still fulfils (2.28), by setting

$$\begin{aligned} g^{\pm}_{G,j}(\kappa,\alpha) = &\frac{A_G w^2}{4\pi} \exp\left[-\frac{w^2}{4}\left((k_x - k_{G,x})^2 + (k_y - k_{G,y})^2\right)\right] \mathrm{e}^{-\mathrm{i}\mathbf{k}^{\pm}\cdot\mathbf{r}_G} \times \\ &\left(\cos\left(\alpha - \alpha_G + \delta_{j_G 2}\frac{\pi}{2}\right)\delta_{j1} \pm \sin\left(\alpha - \alpha_G + \delta_{j_G 2}\frac{\pi}{2}\right)\delta_{j2}\right), \end{aligned} \tag{2.34}$$

where $k_{G,x} = k\cos\beta_G \sin\alpha_G$ and $k_{G,y} = k\sin\beta_G \sin\alpha_G$ are the in-plane Cartesian coordinates belonging to the **k**-vector that corresponds to Ω_G. Note that the oblique beam with Gaussian footprint is ...

- not really a Gaussian beam, because it has a Gaussian electric field profile in the plane $z = 0$, but not in the beam's tilted cross section. It is thus more an elliptical beam.
- an exact solution of Maxwell's equations.
- polarized transverse to the beam's direction of propagation. For $j_G = 1$, the electric field is approximately oriented in the xy-plane (transverse electric), whereas for $j_G = 2$, the electric field is oriented in the $\Omega_G z$-plane (transverse magnetic).

2.3.2. Spherical vector wave functions

Like the PVWFs, the spherical vector wave functions (SVWFs) $\mathbf{\Psi}^{(\nu)}_{plm}$ build a basis set of solutions to the homogeneous Helmholtz equation. They are separable in the

spherical coordinate system. I use the definition of the SVWFs given in [133][4]

$$\mathbf{\Psi}_{1lm}^{(\nu)}(\mathbf{r}) = \frac{\exp(\mathrm{i}m\phi)}{\sqrt{2l(l+1)}} z_l^{(\nu)}(kr)\left(\mathrm{i}m\pi_l^{|m|}(\cos\theta)\hat{\mathbf{e}}_\theta - \tau_l^{|m|}(\cos\theta)\hat{\mathbf{e}}_\phi\right) \tag{2.35}$$

$$\begin{aligned}\mathbf{\Psi}_{2lm}^{(\nu)}(\mathbf{r}) = \frac{\exp(\mathrm{i}m\phi)}{\sqrt{2l(l+1)}} \Bigg\{ & l(l+1)\frac{z_l^{(\nu)}(kr)}{kr} P_l^{|m|}(\cos\theta)\hat{\mathbf{e}}_r \\ & + \frac{\partial_{kr}\left(kr z_l^{(\nu)}(kr)\right)}{kr}\left(\tau_l^{|m|}(\cos\theta)\hat{\mathbf{e}}_\theta + \mathrm{i}m\pi_l^{|m|}(\cos\theta)\hat{\mathbf{e}}_\phi\right)\Bigg\}\end{aligned} \tag{2.36}$$

The SVWFs come in two versions, $\nu = 1, 3$. The only difference between them is the radial function $z_l^{(\nu)}(kr)$ which is given by either the spherical Bessel functions in case of the *regular SVWFs* ($\nu = 1$) or the spherical Hankel functions of first kind in case of the *outgoing SVWFs* ($\nu = 3$):

$$\text{regular SVWFs } \mathbf{\Psi}^{(1)}: \qquad z_l^{(1)}(kr) = j_l(kr) \tag{2.37}$$

$$\text{outgoing SVWFs } \mathbf{\Psi}^{(3)}: \qquad z_l^{(3)}(kr) = h_l(kr) \tag{2.38}$$

The indices (plm) of the SVWFs stand for: p, the polarization where $p = 1$ refers to spherically transverse electric (i.e., $\mathbf{E} \perp \mathbf{r}$) and $p = 2$ stands for spherically transverse magnetic ($\mathbf{H} \perp \mathbf{r}$). l, m, the polar and azimuthal index. These indices reveal that the SVWFs are closely related to the well known spherical harmonics functions $Y_{lm}(\theta, \phi)$.

The normalized associated Legendre functions $P_l^m(x)$ read

$$P_l^m = \sqrt{\frac{(2l+1)(l-m)!}{2(l+m)!}}\left(1-x^2\right)^{\frac{m}{2}} \frac{\mathrm{d}^m \tilde{P}_l(x)}{\mathrm{d}x^m}, \tag{2.39}$$

where $\tilde{P}_l(x)$ denotes the l-th Legendre polynomial, and the angular functions $\pi_l^m(x)$ and $\tau_l^m(x)$ are defined as

$$\pi_l^m(\cos\theta) = \frac{P_l^m(\cos\theta)}{\sin\theta} \tag{2.40}$$

$$\tau_l^m(\cos\theta) = \partial_\theta P_l^m(\cos\theta). \tag{2.41}$$

2.3.2.1. Completeness

The set of regular and outgoing SVWFs is complete in the following sense:

If a domain $D \subset \mathbb{R}^3$ is

[4] In that book, the functions $\mathbf{\Psi}_{1lm}^{(\nu)}$ and $\mathbf{\Psi}_{2lm}^{(\nu)}$ are denoted by $\mathbf{M}_{ml}^{(\nu)}$ and $\mathbf{N}_{ml}^{(\nu)}$, which is the more common notation in literature. For the sake of a tidy notation, I prefer to have a single symbol $\mathbf{\Psi}$ for the SVWFs and refer to the polarization through the index p.

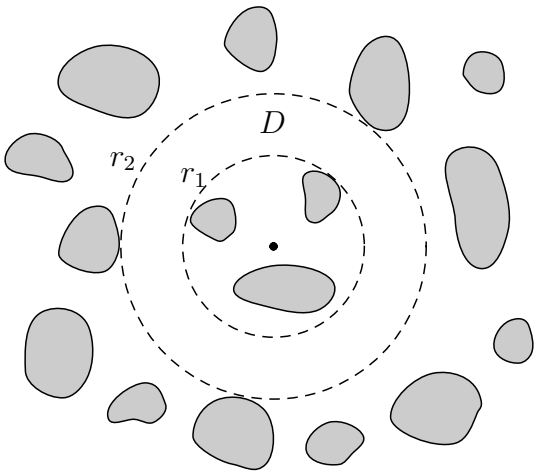

Figure 2.4. – In a homogeneous domain D bounded by two spherical surfaces, every solution of the homogeneous Maxwell's equations can be expanded in spherical waves.

- bounded by two spherical surfaces centered at $\mathbf{r} = \mathbf{0}$, i.e., $D = \{\mathbf{r} | r_1 \leq r \leq r_2\}$ with $0 \leq r_1 < r_2 \leq \infty$,
- source-free and homogeneous, i.e., filled with a material (or vacuum) of constant refractive index,

and $\mathbf{E}(\mathbf{r})$ is a field that

- is divergence-free,
- fulfills the Helmholtz equation for $\mathbf{r} \in D$,

then there exist two sequences a_{plm} and b_{plm} such that for $\mathbf{r} \in D$

$$\mathbf{E}(\mathbf{r}) = \sum_{p=1}^{2} \sum_{l=1}^{\infty} \sum_{m=-l}^{l} \left(a_{plm} \mathbf{\Psi}_{plm}^{(1)}(\mathbf{r}) + b_{plm} \mathbf{\Psi}_{plm}^{(3)}(\mathbf{r}) \right). \tag{2.42}$$

In the following, I will use a multi-index notation $(plm) \to n$,

$$\mathbf{E}(\mathbf{r}) = \sum_{n=1}^{\infty} \left(a_n \mathbf{\Psi}_n^{(1)}(\mathbf{r}) + b_n \mathbf{\Psi}_n^{(3)}(\mathbf{r}) \right). \tag{2.43}$$

For a proof of the completeness of the SVWFs, see for example [134].

If $r_1 = 0$, i.e., when representing the electric field *inside a sphere*, the coefficients b_n must vanish, as the outgoing SVWFs are singular at $\mathbf{r} = \mathbf{0}$, which would lead to unphysical fields. On the contrary, if $r_2 = \infty$, i.e., when representing the electric field *outside a sphere*, the Silver-Müller radiation condition requires $a_n = 0$ for all n.

2.3.2.2. Expansion of the dyadic Green's function in SVWFs

The dyadic Green's function (2.12) can be written as a series of SVWFs [132, 133, 135]:

$$\mathbf{G}(\mathbf{r},\mathbf{r}') = \frac{\mathrm{i}k}{\pi}\sum_n \begin{cases} \mathbf{\Psi}^{(3)}_{p,l,m}(\mathbf{r}) \otimes \mathbf{\Psi}^{(1)}_{p,l,-m}(\mathbf{r}') & |\mathbf{r}| < |\mathbf{r}'| \\ \mathbf{\Psi}^{(1)}_{p,l,m}(\mathbf{r}) \otimes \mathbf{\Psi}^{(3)}_{p,l,-m}(\mathbf{r}') & |\mathbf{r}| > |\mathbf{r}'| \end{cases} \tag{2.44}$$

2.3.3. Transformations and translations

As a consequence of the completeness, a PVWF can be expressed in terms of SVWFs and vice versa. I will need the following formulae (compare [132]):

$$\mathbf{\Psi}^{(3)}_n(\mathbf{r}) = \frac{1}{2\pi}\sum_{j=1}^{2}\int_{\mathbb{R}^2}\frac{\mathrm{d}^2\mathbf{k}_\parallel}{k_z k}\mathrm{e}^{\mathrm{i}m\alpha}B_{nj}(\pm k_z/k)\mathbf{\Phi}^{\pm}_j(\kappa,\alpha;\mathbf{r}) \text{ for } z \gtrless 0 \tag{2.45}$$

and

$$\mathbf{\Phi}^{\pm}_j(\kappa,\alpha;\mathbf{r}) = 4\sum_n \mathrm{e}^{-\mathrm{i}m\alpha}B^{\dagger}_{nj}(\pm k_z/k)\mathbf{\Psi}^{(1)}_n(\mathbf{r}) \tag{2.46}$$

with

$$B_{nj}(x) = -\frac{1}{\mathrm{i}^{l+1}}\frac{1}{\sqrt{2l(l+1)}}(\mathrm{i}\delta_{j1}+\delta_{j2})\Big(\delta_{pj}\tau^{|m|}_l(x) + (1-\delta_{pj})m\pi^{|m|}_l(x)\Big). \tag{2.47}$$

The operator $B^{\dagger}$ has all explicit i in (2.47) changed to $-\mathrm{i}$.

A translation of the coordinate origin is just a trivial phase shift in the case of PVWFs:

$$\mathbf{\Phi}^{\pm}_j(\mathbf{r}+\mathbf{d}) = \mathrm{e}^{\mathrm{i}\mathbf{k}^{\pm}\cdot\mathbf{d}}\mathbf{\Phi}^{\pm}_j(\mathbf{r}). \tag{2.48}$$

In the case of SVWFs, I will make use of the following translation formula which is also called the *SVWF addition theorem*:

$$\mathbf{\Psi}^{(3)}_n(\mathbf{r}+\mathbf{d}) = \sum_{n'} A_{nn'}(\mathbf{d})\mathbf{\Psi}^{(1)}_{n'}(\mathbf{r}) \qquad \text{for } |\mathbf{r}| < |\mathbf{d}|. \tag{2.49}$$

As the translation operator $A_{nn'}$ involves quite messy expressions, I have postponed its definition to the appendix, see Appendix B. It can be constructed either from explicit expressions involving Wigner-3j symbols [135], or from an iterative scheme [133]. Another useful compilation of transformation properties can be found in [132].

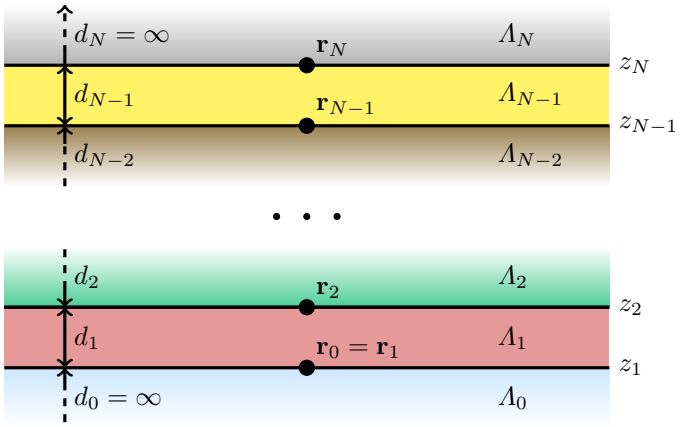

Figure 2.5. – A planarly layered (stratified) medium with layer anchor points $\mathbf{r}_i$.

2.4. Stratified media

A *stratified medium*, or *planarly layered medium*, is a collection of $N+1$ layers $\Lambda_i \subset \mathbb{R}^3$, $i = 0, \ldots, N$. The layers are separated by N z-surfaces, (i.e., planes parallel to the xy-plane), located at $z_1 < \ldots < z_N$. The outermost layers are semi-infinite in size. Each layer is filled with a homogeneous medium such that it is characterized by its thickness d_i and refractive index n_i. If there are no sources or inhomogeneities, the electric field can be expanded in terms of PVWFs inside each layer:

$$\mathbf{E}(\mathbf{r}) = \sum_{j=1}^{2} \int_{\mathbb{R}^2} \mathrm{d}^2\mathbf{k}_\parallel \left[\mathbf{\Phi}_j^+(\kappa,\alpha;\mathbf{r}-\mathbf{r}_i), \mathbf{\Phi}_j^-(\kappa,\alpha;\mathbf{r}-\mathbf{r}_i)\right] \cdot \begin{bmatrix} g_{i,j}^+(\kappa,\alpha) \\ g_{i,j}^-(\kappa,\alpha) \end{bmatrix} \text{ for } \mathbf{r} \in \Lambda_i, \quad (2.50)$$

i.e., $g_{i,j}^{\pm}(\kappa,\alpha)$ are the coefficients of an expansion in terms of forward and backward-going PVWFs relative to the *layer anchor point* $\mathbf{r}_i = (0,0,z_i)$ for $i \geq 1$ and $\mathbf{r}_0 = \mathbf{r}_1$, see Fig. 2.5. Reflection and transmission at the plane interfaces only couple partial waves with identical polarization and in-plane wavevector, i.e., with identical j and (κ,α), such that the propagation through the layered system can be studied separately for each pair of forward and backward propagating partial waves.

2.4.1. Transfer Matrix Scheme

The value of the PVWF-coefficients $g_{i,j}^{\pm}(\kappa,\alpha)$ for neighboring layers are linked by transfer matrices, which are constructed to meet the boundary conditions for the parallel components of the electromagnetic fields (2.10):

$$\begin{bmatrix} g_{i,j}^+(\kappa,\alpha) \\ g_{i,j}^-(\kappa,\alpha) \end{bmatrix} = I_j^{i,i+1}(\kappa) \begin{bmatrix} g_{i+1,j}^+(\kappa,\alpha) \\ g_{i+1,j}^-(\kappa,\alpha) \end{bmatrix} \quad (2.51)$$

where [136]

$$I_j^{i,i+1}(\kappa) = \begin{cases} D_j^{i,i+1}(\kappa) & \text{for } i = 0 \\ P^i(\kappa)\, D_j^{i,i+1}(\kappa) & \text{else,} \end{cases} \tag{2.52}$$

$$D_j^{i,i+1}(\kappa) = \frac{1}{t_{i,i+1,j}(\kappa)} \begin{bmatrix} 1 & r_{i,i+1,j}(\kappa) \\ r_{i,i+1,j}(\kappa) & 1 \end{bmatrix}, \tag{2.53}$$

and

$$P^i(\kappa) = \begin{bmatrix} \exp(-\mathrm{i}k_{z,i}d_i) & 0 \\ 0 & \exp(\mathrm{i}k_{z,i}d_i) \end{bmatrix}. \tag{2.54}$$

The z-component of the wave vector depends on the refractive index in the respective layer, and can be complex: $k_{z,i} = \sqrt{k_i^2 - \kappa}$ where $k_i = n_i\omega/c$. The Fresnel amplitude reflection and transmission coefficients read

$$r_{i,i+1,1}(\kappa) = \frac{k_{z,i} - k_{z,i+1}}{k_{z,i} + k_{z,i+1}} \tag{2.55}$$

$$r_{i,i+1,2}(\kappa) = \frac{n_{i+1}^2 k_{z,i} - n_i^2 k_{z,i+1}}{n_{i+1}^2 k_{z,i} + n_i^2 k_{z,i+1}} \tag{2.56}$$

$$t_{i,i+1,1}(\kappa) = \frac{2k_{z,i}}{k_{z,i} + k_{z,i+1}} \tag{2.57}$$

$$t_{i,i+1,2}(\kappa) = \frac{2n_i n_{i+1} k_{z,i}}{n_{i+1}^2 k_{z,i} + n_i^2 k_{z,i+1}}, \tag{2.58}$$

respectively.

The forward and backward propagating field coefficients of any two layers $i_1 < i_2$ are related via

$$\begin{bmatrix} g_{i_1,j}^+(\kappa,\alpha) \\ g_{i_1,j}^-(\kappa,\alpha) \end{bmatrix} = I_j^{i_1,i_1+1}(\kappa) \ldots I_j^{i_2-1,i_2}(\kappa) \begin{bmatrix} g_{i_2,j}^+(\kappa,\alpha) \\ g_{i_2,j}^-(\kappa,\alpha) \end{bmatrix} \tag{2.59}$$

$$= I_j^{i_1,i_2}(\kappa) \begin{bmatrix} g_{i_2,j}^+(\kappa,\alpha) \\ g_{i_2,j}^-(\kappa,\alpha) \end{bmatrix} \tag{2.60}$$

The above formula defines the so called transfer matrix of the layer subsystem $\Lambda_{i_1}, ..., \Lambda_{i_2}$. However, for larger film thicknesses, it is known to be numerically unstable for evanescent field propagation, see figure 2.6. Then, the slightly more complicated scattering matrix formalism can lead to a better stability.

2.4.2. Scattering Matrix Scheme

For two layers $i_1 < i_2$, the scattering matrix is defined by the relation

$$\begin{bmatrix} g_{i_2,j}^+(\kappa,\alpha) \\ g_{i_1,j}^-(\kappa,\alpha) \end{bmatrix} = S_j^{i_1,i_2}(\kappa) \begin{bmatrix} g_{i_1,j}^+(\kappa,\alpha) \\ g_{i_2,j}^-(\kappa,\alpha) \end{bmatrix}. \tag{2.61}$$

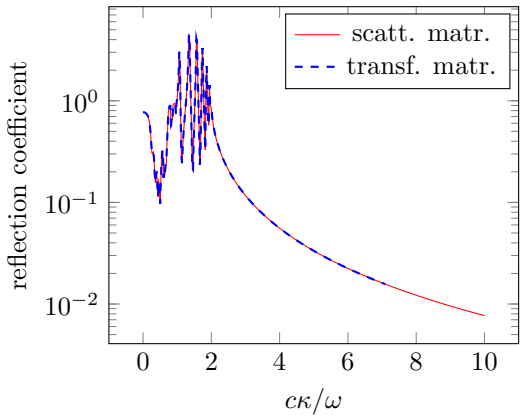

Figure 2.6. – Reflectivity of an examplary layered medium consisting of eleven layers with thickness 1 µm and alterning refractive index of 1 and $2 + 0.01\mathrm{i}$, respectively. The vacuum wavelength is 550 nm. The transfer matrix scheme (dashed blue) breaks down at an in-plane wavenumber of 7 times the vacuum wavenumber. The scattering matrix scheme (solid red) is stable also for large in-plane wavenumbers.

In contrast to the transfer matrix, it links the incoming fields of the layer system between z_{i_1} and z_{i_2}, represented by the forward propagating wave coefficients of Λ_{i_1} and the backward propagating wave coefficient of Λ_{i_2} to the 'outgoing' fields, given by the backward propagating wave in Λ_{i_1} and the forward propagating wave in Λ_{i_2}. The construction of the scattering matrix follows an iterative scheme presented in [137], see also [138]. Starting from

$$S_j^{i_1,i_1}(\kappa) = \begin{bmatrix} 1 & 0 \\ 0 & 1 \end{bmatrix}, \tag{2.62}$$

we successively construct the scattering matrix $S' = S_j^{i_1,i+1}(\kappa)$ from the preceding scattering matrix $S = S_j^{i_1,i}(\kappa)$ by using the relations

$$S'_{11} = \frac{S_{11}}{I_{11} - S_{12}I_{21}} \tag{2.63}$$

$$S'_{12} = \frac{S_{12}I_{22} - I_{12}}{I_{11} - S_{12}I_{21}} \tag{2.64}$$

$$S'_{21} = S_{22}I_{21}S'_{11} + S_{21} \tag{2.65}$$

$$S'_{22} = S_{22}I_{21}S'_{12} + S_{22}I_{22}, \tag{2.66}$$

for $i = i_1, \ldots, i_2 - 1$. In the above, I denotes the layer transition matrix between the layers Λ_i and Λ_{i+1}, i.e. $I_j^{i,i+1}(\kappa)$.

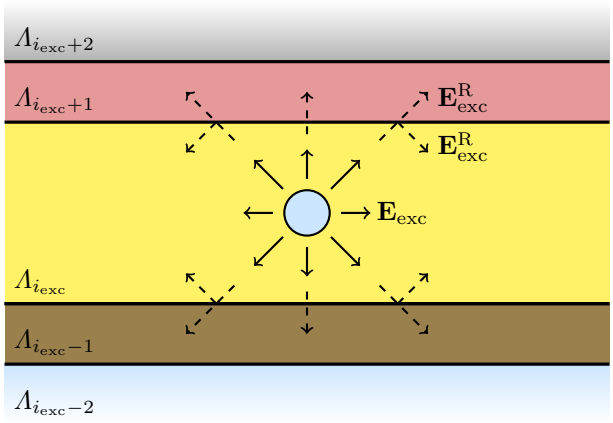

Figure 2.7. – An excitation (source or scattering center) in a layered medium.

2.4.3. Excitation and response

I now turn to the case that an electromagnetic radiation source or a scattering center is located in a domain D_{exc} inside one of the layers (say, layer number i_{exc}): $D_{\text{exc}} \subset \Lambda_{i_{\text{exc}}}$, see Fig. 2.7. For layer i_{exc}, the conditions for (2.18) are not fulfilled and consequently, there exists no expansion of $\mathbf{E}$ in PVWFs that holds everywhere in $\Lambda_{i_{\text{exc}}}$.

However, the transfer matrix scheme and the scattering matrix scheme are based on the continuity conditions at the layer interfaces, and it is sufficient to have the electric field's PVWF expansion there. The idea is to split up the electric field into the *excitation* $\mathbf{E}_{\text{exc}}$ and the *layer system response* $\mathbf{E}^{\text{R}}_{\text{exc}}$:

$$\mathbf{E}(\mathbf{r}) = \delta_{ii_{\text{exc}}}\mathbf{E}_{\text{exc}}(\mathbf{r}) + \mathbf{E}^{\text{R}}_{\text{exc}}(\mathbf{r}) \qquad \text{for } \mathbf{r} \in \Lambda_i, \tag{2.67}$$

One can think of $\mathbf{E}_{\text{exc}}(\mathbf{r})$ as the solution of the Maxwell equations if the radiation source was placed in an infinite homogeneous medium of refractive index $n_{i_{\text{exc}}}$, whereas $\mathbf{E}^{\text{R}}_{\text{exc}}$ refers to the reflection/transmission of $\mathbf{E}_{\text{exc}}$ from/through the layer system interfaces. For a formal definition of $\mathbf{E}_{\text{exc}}$ and $\mathbf{E}^{\text{R}}_{\text{exc}}$, see Appendix C. The expansion of the exciting field in PVWFs defines the coefficients $g^{\pm}_{\text{exc},j}(\kappa,\alpha)$

$$\mathbf{E}_{\text{exc}}(\mathbf{r}) = \sum_{j=1}^{2}\int_{\mathbb{R}^2} \mathrm{d}^2\mathbf{k}_{\parallel} \begin{cases} \mathbf{\Phi}^{+}_{j}(\kappa,\alpha;\mathbf{r}-\mathbf{r}_{i_{\text{exc}}})g^{+}_{\text{exc},j}(\kappa,\alpha) & \text{for } \mathbf{r}\in\Lambda_{i_{\text{exc}}} \text{ and } z \geq z^{\uparrow} \\ \mathbf{\Phi}^{-}_{j}(\kappa,\alpha;\mathbf{r}-\mathbf{r}_{i_{\text{exc}}})g^{-}_{\text{exc},j}(\kappa,\alpha) & \text{for } \mathbf{r}\in\Lambda_{i_{\text{exc}}} \text{ and } z \leq z^{\downarrow}, \end{cases} \tag{2.68}$$

where z^{+} bounds the excitation from above and z^{-} bounds the excitation from below, see Figure C.1. On the other hand, the expansion of the response field in PVWFs defines the coefficients $g^{\text{R}\pm}_{\text{exc},i,j}(\kappa,\alpha)$

$$\mathbf{E}^{\text{R}}_{\text{exc}}(\mathbf{r}) = \sum_{j=1}^{2}\int_{\mathbb{R}^2} \mathrm{d}^2\mathbf{k}_{\parallel} \left[\mathbf{\Phi}^{+}_{j}(\kappa,\alpha;\mathbf{r}-\mathbf{r}_i), \mathbf{\Phi}^{-}_{j}(\kappa,\alpha;\mathbf{r}-\mathbf{r}_i)\right] \cdot \begin{bmatrix} g^{\text{R}+}_{\text{exc},i,j}(\kappa,\alpha) \\ g^{\text{R}-}_{\text{exc},i,j}(\kappa,\alpha) \end{bmatrix} \quad \text{for } \mathbf{r}\in\Lambda_i \tag{2.69}$$

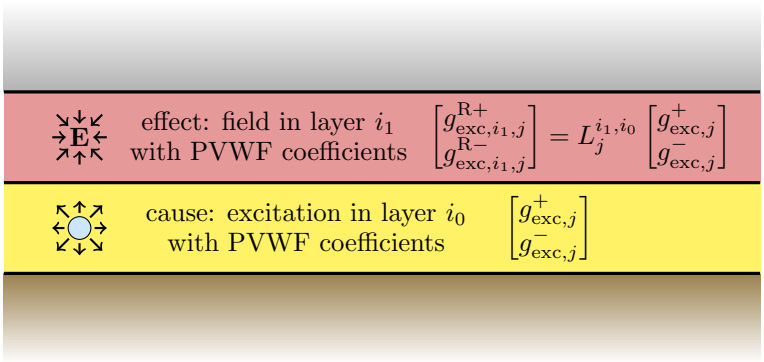

Figure 2.8. – Cause and effect: The layer response matrix

2.4.3.1. The layer system response matrix

Due to the (assumed) linearity of all materials, the propagated electric field must be a linear function of the excitation, such that we can define the matrix $L_j^{i,i_{\mathrm{exc}}}(\kappa)$ by the relation

$$\begin{bmatrix} g^{\mathrm{R},+}_{\mathrm{exc},i,j}(\kappa,\alpha) \\ g^{\mathrm{R},-}_{\mathrm{exc},i,j}(\kappa,\alpha) \end{bmatrix} = L_j^{i,i_{\mathrm{exc}}}(\kappa) \begin{bmatrix} g^{+}_{\mathrm{exc},j}(\kappa,\alpha) \\ g^{-}_{\mathrm{exc},j}(\kappa,\alpha) \end{bmatrix}, \tag{2.70}$$

see figure 2.8.

In order to determine the layer system response matrix, I employ the scattering matrix formalism for the layer subsystems consisting of the layers $\Lambda_0, \ldots, \Lambda_{i_{\mathrm{exc}}}$ and $\Lambda_{i_{\mathrm{exc}}}, \ldots, \Lambda_N$, respectively. For the lower subsystem, the incident partial waves from $\Lambda_{i_{\mathrm{exc}}}$ are given by the PVWF expansion that is valid below the excitation (more precisely, in $D^{\downarrow}$, see Appendix C), such that

$$\begin{bmatrix} g^{\mathrm{R},+}_{\mathrm{exc},i_{\mathrm{exc}},j}(\kappa,\alpha) \\ g^{\mathrm{R},-}_{\mathrm{exc},0,j}(\kappa,\alpha) \end{bmatrix} = S_j^{0,i_{\mathrm{exc}}}(\kappa) \begin{bmatrix} 0 \\ g^{-}_{\mathrm{exc}}(\kappa,\alpha) + g^{\mathrm{R},-}_{\mathrm{exc},i_{\mathrm{exc}},j}(\kappa,\alpha) \end{bmatrix}. \tag{2.71}$$

In other words, the fields that are incident on the lower subsystem consist of the direct field from the excitation, as well as the (still unknown) total reflections from the upper subsystem. Both terms are incident from $\Lambda_{i_{\mathrm{exc}}}$ and propagating downwards.

On the other hand, for the upper subsystem the PVWF expansion valid in $D^{\uparrow}$ is used, such that

$$\begin{bmatrix} g^{\mathrm{R},+}_{\mathrm{exc},0,j}(\kappa,\alpha) \\ g^{\mathrm{R},-}_{\mathrm{exc},i_{\mathrm{exc}},j}(\kappa,\alpha) \end{bmatrix} = S_j^{i_{\mathrm{exc}},N}(\kappa) \begin{bmatrix} g^{+}_{\mathrm{exc}}(\kappa,\alpha) + g^{\mathrm{R},+}_{\mathrm{exc},i_{\mathrm{exc}},j}(\kappa,\alpha) \\ 0 \end{bmatrix}. \tag{2.72}$$

Solving (2.71) and (2.72) for $g^{\mathrm{R},\pm}_{\mathrm{exc},i_{\mathrm{exc}},j}(\kappa,\alpha)$ yields the expansion coefficients of the layer system response in the excitation layer.

$$\begin{bmatrix} g^{\mathrm{R},+}_{\mathrm{exc},i_{\mathrm{exc}},j}(\kappa,\alpha) \\ g^{\mathrm{R},-}_{\mathrm{exc},i_{\mathrm{exc}},j}(\kappa,\alpha) \end{bmatrix} = \left(1 - \begin{bmatrix} 0 & S_{12}^{0,i_{\mathrm{exc}}} \\ S_{21}^{i_{\mathrm{exc}},N} & 0 \end{bmatrix}\right)^{-1} \begin{bmatrix} 0 & S_{12}^{0,i_{\mathrm{exc}}} \\ S_{21}^{i_{\mathrm{exc}},N} & 0 \end{bmatrix} \begin{bmatrix} g^{+}_{\mathrm{exc},j}(\kappa,\alpha) \\ g^{-}_{\mathrm{exc},j}(\kappa,\alpha) \end{bmatrix}, \tag{2.73}$$

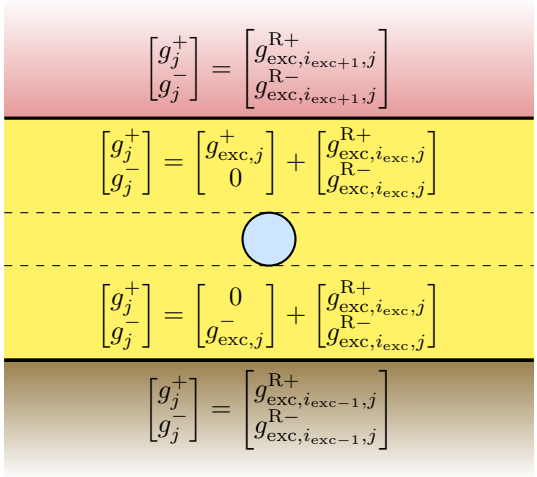

Figure 2.9. – Plane wave expansion coefficients of the electric field below and above the particle.

where the polarization index j and the parallel wave vector dependency κ were suppressed for a clearer notation. By comparison to (2.70), one finds

$$L_j^{i_{\mathrm{exc}}}(\kappa) = \left(1 - \begin{bmatrix} 0 & S_{12}^{0,i_{\mathrm{exc}}} \\ S_{21}^{i_{\mathrm{exc}},N} & 0 \end{bmatrix}\right)^{-1} \begin{bmatrix} 0 & S_{12}^{0,i_{\mathrm{exc}}} \\ S_{21}^{i_{\mathrm{exc}},N} & 0 \end{bmatrix}. \tag{2.74}$$

Here, L_j^i abbreviates the layer system transition matrix from layer i into itself, i.e., $L_j^{i,i}$.

To evaluate the response in layer $i \neq i_{\mathrm{exc}}$, the field coefficients need to be propagated into that layer, e.g. by means of the transfer matrix relation (2.59):

$$L_j^{i,i_{\mathrm{exc}}}(\kappa) = \begin{cases} \left(I_j^{i_{\mathrm{exc}},i}(\kappa)\right)^{-1} \left(L_j^{i_{\mathrm{exc}}}(\kappa) + \begin{bmatrix} 1 & 0 \\ 0 & 0 \end{bmatrix}\right) & \text{for } i > i_{\mathrm{exc}} \\ I_j^{i,i_{\mathrm{exc}}}(\kappa) \left(L_j^{i_{\mathrm{exc}}}(\kappa) + \begin{bmatrix} 0 & 0 \\ 0 & 1 \end{bmatrix}\right) & \text{for } i < i_{\mathrm{exc}}. \end{cases} \tag{2.75}$$

2.4.4. Waveguide modes

Waveguide modes in planarly layered media (slab waveguides) are solutions of Maxwell's equations that decay exponentially for $z \to \pm\infty$, see figure 1.5. A waveguide mode of polarization j_{wg} and in-plane propagation vector $\mathbf{k}_{\parallel,\mathrm{wg}}$ can be constructed by setting

$$\begin{bmatrix} g_{0,j}^+(\kappa,\alpha) \\ g_{0,j}^-(\kappa,\alpha) \end{bmatrix} = \delta_{j,j_{\mathrm{wg}}} \delta^2(\mathbf{k}_\parallel - \mathbf{k}_{\parallel,\mathrm{wg}}) \begin{bmatrix} 0 \\ 1 \end{bmatrix}. \tag{2.76}$$

In order to decay exponentially for $z \to +\infty$, also

$$g^{-}_{N,j_{\mathrm{wg}}}\left(\mathbf{k}_{\parallel,\mathrm{wg}}\right) = 0 \tag{2.77}$$

needs to be fulfilled. Equations (2.76) and (2.77) can be rephrased as the condition that the amplitude reflection coefficient

$$R_{j_{\mathrm{wg}}}(\kappa) = \frac{g^{+}_{N,j_{\mathrm{wg}}}(\kappa,\alpha)}{g^{-}_{N,j_{\mathrm{wg}}}(\kappa,\alpha)} \tag{2.78}$$

of the layer system has a singularity at $\kappa = \left|\mathbf{k}_{\parallel,\mathrm{wg}}\right|$. A robust algorithm to detect waveguide modes through the usage of Cauchy's theorem was proposed in [139].

3. Scattering particles in planarly layered media

This chapter introduces a framework to describe and compute electromagnetic scattering by particles inside a planarly layered medium on the basis of the so called T-matrix method, in combination with the analytical treatment of wave propagation in stratified media as described in chapter 2. Sections 3.1 and 3.2 precise the statement of the problem and the definition of important concepts such as the incoming field, the scattered field and the initial field. The T-matrix formalism is introduced in section 3.3. Section 3.4 can be viewed as the theoretical centerpiece of the multiple scattering derivations: It yields the coupling operators that are then used in sections 3.5 and 3.6 for the computation of the initial field coefficients and the particle interaction coefficients, respectively. Gathering all derivations up to this point, section 3.7 collects the linear system of equations that need to be solved in order to compute the scattered field coefficients. The post processing of the scattered field coefficients into the actual quantities of interest like the electric field distribution or the radiated far field intensity are discussed in sections 3.8 and 3.9, respectively. Finally, section 3.10 provides a discussion about aspects of numerical efficiency.

3.1. Statement of the problem

The following constituents define the scattering problem:

1. A stratified medium, consisting of $N+1$ layers $\Lambda_i \subset \mathbb{R}^3$, $i = 0, \ldots, N$. The layers are separated by N planes which are parallel to the xy-plane and located at $z_1 < \ldots < z_N$. The outermost layers are semi-infinite in size. Each layer is filled by a homogeneous medium such that it is characterized by its thickness d_i and refractive index n_i.

2. A set of scattering particles. N_S denotes the total number of particles. The symbol S (in italic) will be used as an index that refers to each particle. In that sense, $D_S \subset \mathbb{R}^3$ denotes the volume occupied by scattering particle particle S, $\mathbf{r}_S$ is the center of its circumscribing sphere, which has a radius of $r_{\max,S} = \limsup_{\mathbf{r}\in D_S} |\mathbf{r} - \mathbf{r}_S|$, and n_S is the refractive index (which is constant

in D_S). In other words, the refractive index as a function of position reads

$$n(\mathbf{r}) = \begin{cases} n_S & \text{if there is some } S \text{ such that } \mathbf{r} \in D_S \\ n_i & \text{otherwise, with } \mathbf{r} \in \Lambda_i. \end{cases} \tag{3.1}$$

Each particle S is located entirely in one layer i_S, i.e., $D_S \subset \Lambda_{i_S}$. Further, the particles do not overlap with each other's circumscribing spheres: $|\mathbf{r} - \mathbf{r}_{S'}| > r_{\max,S'}$ for $\mathbf{r} \in D_S$.

3. An initial field $\mathbf{E}_{\text{init}}$, originating from layer i_{init} and feeding energy into the system. It can be given either by an explicit field expression (like a plane wave or a Gaussian beam coming from infinity), or it can be caused by a source current distribution $\mathbf{j}(\mathbf{r})$ located inside one or several layers. In this work, I will consider point dipole sources, representing luminescent molecules. However, in that case I require that the source current vanishes inside the particles' circumscribing spheres, unless it is located in a different layer than the respective particle,

$$\mathbf{j}(\mathbf{r}) = \mathbf{0} \qquad \text{if } \mathbf{r} \in \Lambda_{i_S} \text{ and } |\mathbf{r} - \mathbf{r}_S| < r_{\max,S} \text{ for some } S. \tag{3.2}$$

The task is to determine the electric field $\mathbf{E}(\mathbf{r})$ that fulfills the wave equation and boundary conditions[1] specified in section 2.1.

3.2. Initial field, incoming field and scattered field

An important concept used throughout the rest of this chapter is that the total electric field in layer i can be decomposed into a sum of four constituents, the *initial field* $\mathbf{E}_{\text{init}}$, the *scattered field* $\mathbf{E}_{\text{scat}}$ and the *layer system response* $\mathbf{E}^{\text{R}}_{\text{init}}$ and $\mathbf{E}^{\text{R}}_{\text{scat}}$ to each of them:

$$\mathbf{E}(\mathbf{r}) = \delta_{ii_{\text{init}}}\mathbf{E}_{\text{init}}(\mathbf{r}) + \mathbf{E}^{\text{R}}_{\text{init}}(\mathbf{r}) + \sum_S \left(\delta_{ii_S}\mathbf{E}^S_{\text{scat}}(\mathbf{r}) + \mathbf{E}^{\text{R},S}_{\text{scat}}(\mathbf{r})\right), \qquad \mathbf{r} \in \Lambda_i. \tag{3.3}$$

The initial field $\mathbf{E}_{\text{init}}$ is known a priori. It is the primary excitation that feeds energy into the system and is part of the problem definition. It can either be a field coming from infinity, like a plane wave or a beam, or it can be the field excited by a current distribution. Further, $\mathbf{E}^{\text{R}}_{\text{init}}$ is the layer system response to the initial field in the sense of section 2.4.3. According to the definitions given there, $\mathbf{E}_{\text{init}}(\mathbf{r}) = 0$ for $\mathbf{r} \notin \Lambda_{i_{\text{exc}}}$, because $\mathbf{E}^{\text{R}}_{\text{init}}(\mathbf{r})$ includes the field transmitted through the layer interfaces. The initial field together with the layer system response would solve the wave equation and boundary conditions if the particles were absent.

[1] If the initial field is given by a field expression $\mathbf{E}_{\text{init}}(\mathbf{r})$ (e.g., a plane wave or a Gaussian beam) rather than a source current, the radiation boundary condition is required for $\mathbf{E}(\mathbf{r}) - \mathbf{E}_{\text{init}}(\mathbf{r})$.

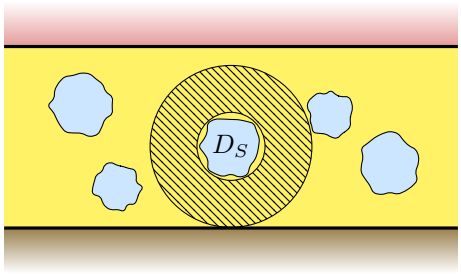

Figure 3.1. – The shaded area indicates the domain $\tilde{D}_S$ in which (3.4) is valid.

The scattered field on the other hand is, heuristically speaking, the reaction of a specific particle on the *incoming field* approaching it. A more precise definition of the scattered field relies on the expansion of the electric field in a spherical shell $\tilde{D}_S$ around some particle S such that no other particle or layer interface intersects, see figure 3.1. Using the completeness of the SVWFs (compare section 2.3.2.1), the electric field can be written as

$$\mathbf{E}\left(\mathbf{r}\right) = \sum_n \left(a_n^S \boldsymbol{\Psi}_n^{(1)}\left(\mathbf{r}-\mathbf{r}_S\right) + b_n^S \boldsymbol{\Psi}_n^{(3)}\left(\mathbf{r}-\mathbf{r}_S\right)\right) \qquad \text{for } \mathbf{r} \in \tilde{D}_S. \tag{3.4}$$

Then, the direct scattered field of particle S is the outgoing part of this expansion,

$$\mathbf{E}_{\mathrm{scat}}^S\left(\mathbf{r}\right) = \sum_n b_n^S \boldsymbol{\Psi}_n^{(3)}\left(\mathbf{r}-\mathbf{r}_S\right), \tag{3.5}$$

whereas $\mathbf{E}_{\mathrm{scat}}^{\mathrm{R},S}$ is the layer system response to $\mathbf{E}_{\mathrm{scat}}^S$ as defined in section 2.4.3.

Finally, the *incoming field* $\mathbf{E}_{\mathrm{inc}}^S$ of each particle S is defined as the regular part of the expansion (3.4).

$$\mathbf{E}_{\mathrm{inc}}^S\left(\mathbf{r}\right) = \sum_n a_n^S \boldsymbol{\Psi}_n^{(1)}\left(\mathbf{r}-\mathbf{r}_S\right) \tag{3.6}$$

It includes:

- the initial field
- the layer system response to the initial field
- the (direct) scattered field from the other particles $S' \neq S$
- the layer system response for the scattered field of all particles, including the selected particle S

$$\mathbf{E}_{\mathrm{inc}}^{S}(\mathbf{r}) = \delta_{i_S i_{\mathrm{init}}}\mathbf{E}_{\mathrm{init}}(\mathbf{r}) + \mathbf{E}_{\mathrm{init}}^{\mathrm{R}}(\mathbf{r}) + \sum_{S'\neq S}\delta_{i_S i_{S'}}\mathbf{E}_{\mathrm{scat}}^{S'}(\mathbf{r}) + \sum_{S'}\mathbf{E}_{\mathrm{scat}}^{\mathrm{R},S'}(\mathbf{r}) \tag{3.7}$$

Accordingly, the expansion coefficients are written as a sum of four contributions:

$$a_n^S = a_n^{S,\mathrm{init}} + a_n^{S,\mathrm{R},\mathrm{init}} + \sum_{S'}\left(a_n^{S,S'} + a_n^{S,\mathrm{R},S'}\right) \tag{3.8}$$

with $a_n^{S,S} = 0$. The superscript notation should be interpreted by reading from right to left, for example, $a_n^{S,\mathrm{R},S'}$ is the coefficient that corresponds to the field scattered by particle S', then propagated through (or reflected by) the layer system (R), and finally received by particle S.

Note that unlike the *initial field*, the *incoming field* is defined separately for each sphere and is not known a priori.

3.3. The T-matrix

The T-matrix [2] was at first introduced in the context of single particle scattering in a homogeneous background medium, and later its use was extended to the case of multiple particles [4] and to particles near planar interfaces [5, 6]. It maps the expansion coefficients a_n of the incoming field to the expansion coefficients b_n of the scattered field:

$$b_n^S = \sum_{n'=1}^{\infty} T_{nn'}^S a_{n'}^S. \tag{3.9}$$

Therefore, the T-matrix incorporates the complete information about the scattering behaviour of the scatterer, and its knowledge enables the solution of any scattering problem involving S. Due to the convergence of (3.4), T can in praxis always be approximated by a finite matrix, i.e., (3.9) can be truncated at some $n = n_{\mathrm{trunc}}$ that corresponds to some cut-off multipole order $l = l_{\mathrm{trunc}}$. In this sense, we can regard the T-matrix as an economical, encapsulated (i.e., modular) representation of the scattering behaviour of each scatterer.

The computation of the T-matrix for a general scattering particle is a difficult task, but this is not part of this thesis. In fact, after a short overview on the most common methods for its computation in section 3.3.1, I will treat the T-matrix in the following as a "black box" and just assume that it is precisely known.

3.3.1. Computing the T-matrix

Traditionally, the T-matrix method is associated with the so called *null field method* for its computation[2], but in fact, any numerical method for the solution of Maxwell's equation can be used to construct the T-matrix, by solving the single particle scattering problem with particle S in a homogeneous background medium with refractive index $n = n_{i_S}$ and with $\mathbf{E}_{\text{init}}(\mathbf{r}) = \mathbf{\Psi}_{n'}^{(1)}$ as the initial field, then expressing the resulting scattered field in terms of outgoing SVWFs. This means that in total n_{trunc} scattering problems need to be solved.

A comprehensive database of papers that deal with the T-matrix method can be found in [140–146]. Methods that are used to compute the T-matrix include (but are not restricted to) the Mie formulae (in the case of spherical particles), the Null field method (NFM) [2], the Null field method with discrete sources (NFM-DS) [133, 147], the Discrete dipole approximation (DDA) [148] or Volume integral equation method (VIEM) [149] and the Finite element method (FEM) [150].

In the following, I will briefly sketch the Mie solution, the NFM and the NFM-DS. The latter is very important for this thesis, as all T-matrices for non-spherical particles in the application examples presented in chapters 4 and 5 are computed with that method.

Mie's solution for spheres In case of spherical scattering particles, the T-matrix method reduces to the famous Mie solution [151, 152]. The T-matrix is then diagonal and only depends on l and p, but not on m:

$$T_{nn'} = \delta_{pp'}\delta_{mm'}\delta_{ll'}Q_{pl} \tag{3.10}$$

with

$$\begin{aligned} Q_{1l} &= \frac{j_l(kR)\,\partial_{k_SR}(k_SRj_l(k_SR)) - j_l(k_SR)\,\partial_{kR}(kRj_l(kR))}{j_l(k_SR)\,\partial_{kR}(kRh_l(kR)) - h_l(kR)\,\partial_{k_SR}(k_SRj_l(k_SR))} \\ Q_{2l} &= \frac{k^2 j_l(kR)\,\partial_{k_SR}(k_SRj_l(k_SR)) - k_S^2 j_l(k_SR)\,\partial_{k_MR}(kRj_l(kR))}{k_S^2 j_l(k_SR)\,\partial_{kR}(kRh_l(kR)) - k^2 h_l(kR)\,\partial_{k_SR}(k_SRj_l(k_SR))}. \end{aligned} \tag{3.11}$$

In the above, R is the radius of the sphere and k_S and k are the wavenumbers inside and outside the scattering particle, respectively, whereas j_l and h_l denote the spherical Bessel and spherical Hankel function of the first kind.

[2] Often, the terms T-matrix method and null field method are used synonymously. Here, we stick to the broader definition of the term "T-matrix method" according to [140].

Null field method The Null field method (NFM, also called the *extended boundary condition method*, EBCM) was introduced by Waterman [2] and relies on an expansion of the internal field inside the particle as well as the scattered field and the incoming field in SVWFs:

$$\mathbf{E}^S_{\text{int}}(\mathbf{r}) = \sum_n c^S_n \boldsymbol{\Psi}^{(1)}_{1lm}(\mathbf{r}_{S'} - \mathbf{r}_S). \tag{3.12}$$

Exploiting the boundary conditions (2.10) at the surface of the scattering particle and using the so called *vector Green's identity*, linear relations can be derived between the expansion coefficients for the incoming field and the internal field as well as for the scattered field and the internal field:

$$a^S_n = \sum_{n'} Q^S_{n,n'} c^S_{n'} \tag{3.13}$$

$$b^S_n = \sum_{n'} -\text{Rg}Q^S_{n,n'} c^S_{n'} \tag{3.14}$$

such that the T-matrix can be computed as

$$T^S = -\text{Rg}Q^S \left(Q^S\right)^{-1}. \tag{3.15}$$

Null field method with discrete sources The Null field method with discrete sources (NFM-DS) [133, 147] is an extension of the Null field method, aiming at an improved stability in the case of particles that deviate strongly from the shape of a sphere, e.g., spheroids with large aspect ratios. To this end, the fields are approximated by equivalent sources outside the respective domain where the solution is sought. In this respect, it is related to the class of *generalized multipole methods*. In order to exploit axial symmetry, the discrete sources for oblate particles can be placed on the *imaginary continuation* of the z-axis.

3.4. The incoming field

As defined in section 3.2, the incoming field includes the initial field and the scattered field from all other particles, as well as the layer system response to the initial field and the scattered field from all particles. In the context of the T-matrix method (see section 3.3), the incoming field needs to be expanded in terms of regular SVWFs. We will face the following task:

> *Given a source (an excitation) of an electromagnetic field located at position* $\mathbf{r}_{\text{exc}}$ *(or at infinity, as in the case of an initial plane wave), construct the total electric field* $\mathbf{E}$ *caused by that excitation as an expansion in regular spherical vector wave functions relative to a receiver location* $\mathbf{r}_{\text{rec}}$ *which can be in the same or a different layer than* $\mathbf{r}_{\text{exc}}$.

Here, the excitation can either be given in terms of a plane wave expansion, or in terms of an outgoing spherical wave expansion relative to $\mathbf{r}_{\mathrm{exc}}$. The goal of this section is thus to derive coupling operators V, V^{R}, W and W^{R} which do this job:

- The PWE to SWE coupling operators V and V^{R} map the plane wave expansion coefficients of an excitation (e.g., located at infinity) to the regular spherical wave expansion coefficients of the direct and layer system mediated resulting field relative to $\mathbf{r}_{\mathrm{rec}}$.
- The SWE to SWE coupling operators W and W^{R} map the outgoing spherical wave expansion coefficients of a localized excitation to the regular spherical wave expansion coefficients of the direct and layer system mediated resulting field relative to $\mathbf{r}_{\mathrm{rec}}$.

As a starting point, the electric field at $\mathbf{r}_{\mathrm{rec}}$ is written as

$$\mathbf{E}(\mathbf{r}_{\mathrm{rec}}) = \delta_{i_{\mathrm{rec}},i_{\mathrm{exc}}}\mathbf{E}_{\mathrm{exc}}(\mathbf{r}_{\mathrm{rec}}) + \mathbf{E}^{\mathrm{R}}_{\mathrm{exc}}(\mathbf{r}_{\mathrm{rec}}), \tag{3.16}$$

compare (2.67), where $\mathbf{E}_{\mathrm{exc}}$ denotes the exciting field and $\mathbf{E}^{\mathrm{R}}_{\mathrm{exc}}$ denotes the layer system response whereas i_{exc} and i_{rec} refer to the layers containing the excitation ("exc") and the receiver ("rec"), respectively.

Expanding[3] the field in regular SVWFs around $\mathbf{r}_{\mathrm{rec}}$,

$$\mathbf{E}_{\mathrm{exc}}(\mathbf{r}) = \sum_n a_n^{\mathrm{rec,exc}}\boldsymbol{\Psi}_n^{(1)}(\mathbf{r}-\mathbf{r}_{\mathrm{rec}}) \tag{3.17}$$

$$\mathbf{E}^{\mathrm{R}}_{\mathrm{exc}}(\mathbf{r}) = \sum_n a_n^{\mathrm{rec,R,exc}}\boldsymbol{\Psi}_n^{(1)}(\mathbf{r}-\mathbf{r}_{\mathrm{rec}}), \tag{3.18}$$

the task is now to construct the coefficients $a_n^{\mathrm{rec,R,exc}}$ (the *response coefficients*) and, if $\mathbf{r}_{\mathrm{rec}}$ is located in the same layer as $\mathbf{r}_{\mathrm{exc}}$, also $a_n^{\mathrm{rec,exc}}$ (the *direct coefficients*).

3.4.1. Excitation as plane wave expansion

One relevant case (mostly for sources located at infinity, $z_{\mathrm{exc}} = \pm\infty$) is that the excitation is given in terms of a plane wave expansion with coefficients $g^{\pm}_{\mathrm{exc},j}(\kappa,\alpha)$:

$$\mathbf{E}_{\mathrm{exc}}(\mathbf{r}) = \sum_{j=1}^{2}\int_{\mathbb{R}^2}\mathrm{d}^2\mathbf{k}_{\parallel}\begin{cases}\boldsymbol{\Phi}_j^{+}(\kappa,\alpha;\mathbf{r}-\mathbf{r}_{i_{\mathrm{exc}}})g^{+}_{\mathrm{exc},j}(\mathbf{k}_{\parallel}) & \text{for } z \geq z_{\mathrm{exc}}\\ \boldsymbol{\Phi}_j^{-}(\kappa,\alpha;\mathbf{r}-\mathbf{r}_{i_{\mathrm{exc}}})g^{-}_{\mathrm{exc},j}(\mathbf{k}_{\parallel}) & \text{for } z \leq z_{\mathrm{exc}}.\end{cases} \tag{3.19}$$

[3] In general, this expansion is valid only in the vicinity of $\mathbf{r}_{\mathrm{rec}}$.

3.4.1.1. Direct coefficients

If $\mathbf{r}$ is in the same layer as $\mathbf{r}_{\mathrm{exc}}$, the direct coefficients can be constructed with the following procedure: First, the reference point of the PVWF is translated to $\mathbf{r}_{\mathrm{rec}}$ using (2.48),

$$\mathbf{\Phi}_j^{\pm}(\kappa,\alpha;\mathbf{r}-\mathbf{r}_{i_{\mathrm{exc}}}) = \mathrm{e}^{\mathrm{i}\mathbf{k}_{i_{\mathrm{exc}}}^{\pm}\cdot(\mathbf{r}_{i_{\mathrm{exc}}}-\mathbf{r}_{\mathrm{rec}})}\mathbf{\Phi}_j^{\pm}(\kappa,\alpha;\mathbf{r}-\mathbf{r}_{\mathrm{rec}}). \tag{3.20}$$

Then, (2.46) is used to expand the PVWFs in regular SVWFs, which leads to (3.17) with

$$a_n^{\mathrm{rec,exc}} = 4\sum_{j=1}^{2}\int_{\mathbb{R}^2}\mathrm{d}^2\mathbf{k}_{\parallel}\, g_{\mathrm{exc},j}^{\pm}\big(\mathbf{k}_{\parallel}\big)\mathrm{e}^{-\mathrm{i}m\alpha}\mathrm{e}^{\mathrm{i}\mathbf{k}_{i_{\mathrm{exc}}}^{\pm}\cdot(\mathbf{r}_{i_{\mathrm{exc}}}-\mathbf{r}_{\mathrm{rec}})}B_{nj}^{\dagger}\left(\frac{\pm k_{z,i_{\mathrm{exc}}}}{k_{i_{\mathrm{exc}}}}\right), \tag{3.21}$$

where from $\pm$ the plus sign is to be selected if $z_{\mathrm{rec}} > z_{\mathrm{exc}}$ and the minus sign is to be selected if $z_{\mathrm{rec}} < z_{\mathrm{exc}}$.

Introducing the PWE to SWE coupling operator $V_{n,j}^{\pm,\mathrm{rec,exc}}\big(\mathbf{k}_{\parallel}\big)$, the above can be rewritten as

$$a_n^{\mathrm{rec,exc}} = \sum_{j=1}^{2}\int_{\mathbb{R}^2}\mathrm{d}^2\mathbf{k}_{\parallel}\left[V_{n,j}^{+}\big(\mathbf{r}_{\mathrm{rec}},\mathbf{r}_{\mathrm{exc}};\mathbf{k}_{\parallel}\big), V_{n,j}^{-}\big(\mathbf{r}_{\mathrm{rec}},\mathbf{r}_{\mathrm{exc}};\mathbf{k}_{\parallel}\big)\right]\cdot\begin{bmatrix} g_{\mathrm{exc},j}^{+}\big(\mathbf{k}_{\parallel}\big) \\ g_{\mathrm{exc},j}^{-}\big(\mathbf{k}_{\parallel}\big), \end{bmatrix}, \tag{3.22}$$

with

$$V_{n,j}^{\pm}\big(\mathbf{r}_{\mathrm{rec}},\mathbf{r}_{\mathrm{exc}};\mathbf{k}_{\parallel}\big) = \begin{cases} 4\mathrm{e}^{-\mathrm{i}m\alpha}\mathrm{e}^{\mathrm{i}\mathbf{k}_{i_{\mathrm{exc}}}^{\pm}\cdot(\mathbf{r}_{i_{\mathrm{exc}}}-\mathbf{r}_{\mathrm{rec}})}B_{nj}^{\dagger}\left(\frac{\pm k_{z,i_{\mathrm{exc}}}}{k_{i_{\mathrm{exc}}}}\right) & \text{if } z_{\mathrm{rec}} \gtrless z_{\mathrm{exc}} \\ 0 & \text{else} \end{cases} \tag{3.23}$$

Note that in the above derivation, the order of two limiting processes (the sum over n and the integral over $\mathrm{d}^2\mathbf{k}_{\parallel}$) was changed which I assume for the moment to be a valid operation.

3.4.1.2. Response coefficients

First, the layer system response to (3.17) is written as (compare (2.69))

$$\mathbf{E}_{\mathrm{exc}}^{\mathrm{R}}(\mathbf{r}) = \sum_{j=1}^{2}\int_{\mathbb{R}^2}\mathrm{d}^2\mathbf{k}_{\parallel}\left[\mathbf{\Phi}_j^{+}\big(\mathbf{k}_{\parallel};\mathbf{r}-\mathbf{r}_{i_{\mathrm{rec}}}\big), \mathbf{\Phi}_j^{-}\big(\mathbf{k}_{\parallel};\mathbf{r}-\mathbf{r}_{i_{\mathrm{rec}}}\big)\right]\cdot\begin{bmatrix} g_{\mathrm{exc},i_{\mathrm{rec}},j}^{\mathrm{R}+}\big(\mathbf{k}_{\parallel}\big) \\ g_{\mathrm{exc},i_{\mathrm{rec}},j}^{\mathrm{R}-}\big(\mathbf{k}_{\parallel}\big) \end{bmatrix}, \tag{3.24}$$

where the coefficients $g_{\mathrm{exc},i_{\mathrm{rec}},j}^{\mathrm{R}\pm}(\kappa,\alpha)$ are constructed according to

$$\begin{bmatrix} g_{\mathrm{exc},i_{\mathrm{rec}},j}^{\mathrm{R}+}\big(\mathbf{k}_{\parallel}\big) \\ g_{\mathrm{exc},i_{\mathrm{rec}},j}^{\mathrm{R}-}\big(\mathbf{k}_{\parallel}\big) \end{bmatrix} = L_j^{i_{\mathrm{rec}},i_{\mathrm{exc}}}(\kappa)\begin{bmatrix} g_{\mathrm{exc},j}^{+}\big(\mathbf{k}_{\parallel}\big) \\ g_{\mathrm{exc},j}^{-}\big(\mathbf{k}_{\parallel}\big) \end{bmatrix}. \tag{3.25}$$

using the layer system response matrix, see section 2.4.3.1. In analogy to section 3.4.1.1, the reference point of the PVWFs in (3.24) is translated from $\mathbf{r}_{i_{\mathrm{rec}}}$ to $\mathbf{r}_{\mathrm{rec}}$ using (2.48) and then the PVWFs are expanded in SVWFs using (2.46) to yield (3.18) with

$$a_n^{\mathrm{rec,R,exc}} = 4\sum_{j=1}^{2}\int_{\mathbb{R}^2} \mathrm{d}^2\mathbf{k}_\parallel \mathrm{e}^{-\mathrm{i}m\alpha}\left[\mathrm{e}^{\mathrm{i}\mathbf{k}^+_{i_{\mathrm{rec}}}\cdot(\mathbf{r}_{\mathrm{rec}}-\mathbf{r}_{i_{\mathrm{rec}}})} B^\dagger_{nj}\left(\frac{k_{z,i_{\mathrm{rec}}}}{k_{i_{\mathrm{rec}}}}\right),\right.$$
$$\left.\mathrm{e}^{\mathrm{i}\mathbf{k}^-_{i_{\mathrm{rec}}}\cdot(\mathbf{r}_{\mathrm{rec}}-\mathbf{r}_{i_{\mathrm{rec}}})} B^\dagger_{nj}\left(\frac{-k_{z,i_{\mathrm{rec}}}}{k_{i_{\mathrm{rec}}}}\right)\right]$$
$$\cdot L_j^{i_{\mathrm{rec}},i_{\mathrm{exc}}}(\kappa)\cdot\begin{bmatrix} g^+_{\mathrm{exc},j}\left(\mathbf{k}_\parallel\right)\\ g^-_{\mathrm{exc},j}\left(\mathbf{k}_\parallel\right)\end{bmatrix}. \tag{3.26}$$

For convenience, I define the symbols

$$\beta^{\pm}_{\mathrm{exc},n,j}(\kappa) = \mathrm{e}^{\mp\mathrm{i}k_{z,i_{\mathrm{exc}}}(z_{\mathrm{exc}}-z_{i_{\mathrm{exc}}})} B_{nj}(\pm k_{z,i_{\mathrm{exc}}}/k_{i_{\mathrm{exc}}}) \tag{3.27}$$
$$\beta^{\pm,\dagger}_{\mathrm{rec},n,j}(\kappa) = \mathrm{e}^{\pm\mathrm{i}k_{z,i_{\mathrm{rec}}}(z_{\mathrm{rec}}-z_{i_{\mathrm{rec}}})} B^\dagger_{nj}(\pm k_{z,i_{\mathrm{rec}}}/k_{i_{\mathrm{rec}}}) \tag{3.28}$$

to rewrite the above as

$$a_n^{\mathrm{rec,R,exc}} = 4\sum_{j=1}^{2}\int_{\mathbb{R}^2} \mathrm{d}^2\mathbf{k}_\parallel \mathrm{e}^{-\mathrm{i}m\alpha}\mathrm{e}^{\mathrm{i}\mathbf{k}_\parallel\cdot\mathbf{r}_{\mathrm{rec},\parallel}} \tag{3.29}$$
$$\times\left[\beta^{+,\dagger}_{\mathrm{rec},n,j}(\kappa),\beta^{-,\dagger}_{\mathrm{rec},n,j}(\kappa)\right]\cdot L_j^{i_{\mathrm{rec}},i_{\mathrm{exc}}}(\kappa)\cdot\begin{bmatrix} g^+_{\mathrm{exc},j}\left(\mathbf{k}_\parallel\right)\\ g^-_{\mathrm{exc},j}\left(\mathbf{k}_\parallel\right)\end{bmatrix},$$

where $\mathbf{r}_{\parallel,i_{\mathrm{rec}}} = \mathbf{0}$ was used, or, introducing the layer system mediated PWE to SWE coupling operator $V^{\mathrm{R},\pm}_{n,j}\left(\mathbf{r}_{\mathrm{rec}},\mathbf{r}_{\mathrm{exc}};\mathbf{k}_\parallel\right)$, as

$$a_n^{\mathrm{rec,R,exc}} = \sum_{j=1}^{2}\int_{\mathbb{R}^2} \mathrm{d}^2\mathbf{k}_\parallel \left[V^{\mathrm{R},+}_{n,j}\left(\mathbf{r}_{\mathrm{rec}},\mathbf{r}_{\mathrm{exc}};\mathbf{k}_\parallel\right),V^{\mathrm{R},-}_{n,j}\left(\mathbf{r}_{\mathrm{rec}},\mathbf{r}_{\mathrm{exc}};\mathbf{k}_\parallel\right)\right]\cdot\begin{bmatrix} g^+_{\mathrm{exc},j}\left(\mathbf{k}_\parallel\right)\\ g^-_{\mathrm{exc},j}\left(\mathbf{k}_\parallel\right)\end{bmatrix}, \tag{3.30}$$

with

$$\left[V^{\mathrm{R},+}_{n,j}\left(\mathbf{r}_{\mathrm{rec}},\mathbf{r}_{\mathrm{exc}};\mathbf{k}_\parallel\right),V^{\mathrm{R},-}_{n,j}\left(\mathbf{r}_{\mathrm{rec}},\mathbf{r}_{\mathrm{exc}};\mathbf{k}_\parallel\right)\right] = 4\mathrm{e}^{-\mathrm{i}m\alpha}\mathrm{e}^{\mathrm{i}\mathbf{k}_\parallel\cdot\mathbf{r}_{\mathrm{rec},\parallel}} \tag{3.31}$$
$$\times\left[\beta^{+,\dagger}_{\mathrm{rec},n,j}(\kappa),\beta^{-,\dagger}_{\mathrm{rec},n,j}(\kappa)\right]\cdot L_j^{i_{\mathrm{rec}},i_{\mathrm{exc}}}(\kappa).$$

3.4.2. Excitation as spherical wave expansion

The other relevant case is when the excitation is given in terms of a spherical wave expansion with coefficients b_n^{exc}:

$$\mathbf{E}_{\mathrm{exc}}\left(\mathbf{r}\right) = \sum_{n'} b^{\mathrm{exc}}_{n'}\boldsymbol{\Psi}^{(3)}_{n'}(\mathbf{r}-\mathbf{r}_{\mathrm{exc}}) \tag{3.32}$$

3.4.2.1. Direct coefficients

If $\mathbf{r}$ is in the same layer as $\mathbf{r}_{\mathrm{exc}}$, the direct coefficients can be computed using the SVWF addition theorem (2.49):

$$\mathbf{E}_{\mathrm{exc}}(\mathbf{r}) = \sum_{n'} b_{n'}^{\mathrm{exc}} \sum_{n} A_{n'n}(\mathbf{r}_{\mathrm{rec}} - \mathbf{r}_{\mathrm{exc}}) \boldsymbol{\Psi}_{n}^{(1)}(\mathbf{r} - \mathbf{r}_{\mathrm{rec}}) \qquad \text{for } |\mathbf{r} - \mathbf{r}_{\mathrm{rec}}| < |\mathbf{r}_{\mathrm{exc}} - \mathbf{r}_{\mathrm{rec}}|. \tag{3.33}$$

which, by comparison to (3.17) yields

$$a_{n}^{\mathrm{rec,exc}} = \sum_{n'} W_{n,n'}(\mathbf{r}_{\mathrm{rec}}, \mathbf{r}_{\mathrm{exc}}) b_{n'}^{\mathrm{exc}} \tag{3.34}$$

with the direct coupling matrix

$$W_{n,n'}(\mathbf{r}_{\mathrm{rec}}, \mathbf{r}_{\mathrm{exc}}) = A_{n'n}(\mathbf{r}_{\mathrm{rec}} - \mathbf{r}_{\mathrm{exc}}) \tag{3.35}$$

3.4.2.2. Response coefficients

The first step is to transform the SVWFs in (3.32) to a PVWFs by using (2.45), and to translate the reference point of the PVWFs to the layer anchor point $\mathbf{r}_{i_{\mathrm{exc}}}$:

$$\mathbf{E}_{\mathrm{exc}}(\mathbf{r}) = \sum_{n'} b_{n'} \boldsymbol{\Psi}_{n'}^{(3)}(\mathbf{r} - \mathbf{r}_{\mathrm{exc}}) \tag{3.36}$$

$$= \frac{1}{2\pi} \sum_{j=1}^{2} \sum_{n'} b_{n'} \int_{\mathbb{R}^2} \frac{\mathrm{d}^2\mathbf{k}_{\parallel}}{k_{z,i_{\mathrm{exc}}} k_{i_{\mathrm{exc}}}} \mathrm{e}^{\mathrm{i}m'\alpha} B_{n'j}(\pm k_{z,i_{\mathrm{exc}}}/k_{i_{\mathrm{exc}}}) \tag{3.37}$$

$$\times \mathrm{e}^{-\mathrm{i}\mathbf{k}_{i_{\mathrm{exc}}}^{\pm} \cdot (\mathbf{r}_{\mathrm{exc}} - \mathbf{r}_{i_{\mathrm{exc}}})} \boldsymbol{\Phi}_{j}^{\pm}(\kappa, \alpha; \mathbf{r} - \mathbf{r}_{i_{\mathrm{exc}}}) \qquad \text{for } z \gtrless z_{\mathrm{exc}}.$$

Inserting (3.28) yields

$$\mathbf{E}_{\mathrm{exc}}(\mathbf{r}) = \frac{1}{2\pi} \sum_{j=1}^{2} \sum_{n'} b_{n'} \int_{\mathbb{R}^2} \frac{\mathrm{d}^2\mathbf{k}_{\parallel}}{k_{z,i_{\mathrm{exc}}} k_{i_{\mathrm{exc}}}} \mathrm{e}^{\mathrm{i}m'\alpha} \mathrm{e}^{-\mathrm{i}\mathbf{k}_{\parallel} \cdot (\mathbf{r}_{\mathrm{exc},\parallel} - \mathbf{r}_{i_{\mathrm{exc}},\parallel})} \tag{3.38}$$

$$\times \beta_{\mathrm{exc},n',j}^{\pm}(\kappa) \boldsymbol{\Phi}_{j}^{\pm}(\kappa, \alpha; \mathbf{r} - \mathbf{r}_{i_{\mathrm{exc}}}) \qquad \text{for } z \gtrless z_{\mathrm{exc}},$$

and recognizing that (3.38) has the form of (3.19) with

$$g_{\mathrm{exc},j}^{\pm}(\kappa, \alpha) = \frac{1}{2\pi} \frac{\mathrm{e}^{-\mathrm{i}\mathbf{k}_{\parallel} \cdot \mathbf{r}_{\mathrm{exc},\parallel}}}{k_{z,i_{\mathrm{exc}}} k_{i_{\mathrm{exc}}}} \sum_{n'} b_{n'} \mathrm{e}^{\mathrm{i}m'\alpha} \beta_{\mathrm{exc},n',j}^{\pm}(\kappa) \tag{3.39}$$

allows us to follow the derivation presented in section 3.4.1.2 to find

$$a_{n}^{\mathrm{rec,R,exc}} = \frac{2}{\pi} \sum_{j=1}^{2} \sum_{n'} b_{n'} \int_{\mathbb{R}^2} \frac{\mathrm{d}^2\mathbf{k}_{\parallel}}{k_{z,i_{\mathrm{exc}}} k_{i_{\mathrm{exc}}}} \mathrm{e}^{\mathrm{i}(m'-m)\alpha} \mathrm{e}^{\mathrm{i}\mathbf{k}_{\parallel} \cdot (\mathbf{r}_{\mathrm{rec},\parallel} - \mathbf{r}_{\mathrm{exc},\parallel})} \tag{3.40}$$

$$\times \left[\beta_{\mathrm{rec},n,j}^{+,\dagger}(\kappa), \beta_{\mathrm{rec},n,j}^{-,\dagger}(\kappa) \right] \cdot L_{j}^{i_{\mathrm{rec}}, i_{\mathrm{exc}}}(\kappa) \cdot \begin{bmatrix} \beta_{\mathrm{exc},n',j}^{+}(\kappa) \\ \beta_{\mathrm{exc},n',j}^{-}(\kappa) \end{bmatrix}$$

which can be rewritten as

$$a_n^{\mathrm{R}} = \sum_{n'} W_{n,n'}^{\mathrm{R}}(\mathbf{r}_{\mathrm{rec}}, \mathbf{r}_{\mathrm{exc}}) b_{n'}^{\mathrm{exc}}, \tag{3.41}$$

with the response coupling matrix

$$\begin{aligned} W_{n,n'}^{\mathrm{R}}(\mathbf{r}_{\mathrm{rec}}, \mathbf{r}_{\mathrm{exc}}) = \frac{2}{\pi} \sum_{j=1}^{2} \int_{\mathbb{R}^2} \frac{\mathrm{d}^2\mathbf{k}_\parallel}{k_{z,i_{\mathrm{exc}}} k_{i_{\mathrm{exc}}}} \mathrm{e}^{\mathrm{i}(m'-m)\alpha} \mathrm{e}^{\mathrm{i}\mathbf{k}_\parallel \cdot \left(\mathbf{r}_{\mathrm{rec},\parallel} - \mathbf{r}_{\mathrm{exc},\parallel}\right)} \\ \times \left[\beta_{\mathrm{rec},n,j}^{+,\dagger}(\kappa), \beta_{\mathrm{rec},n,j}^{-,\dagger}(\kappa)\right] \cdot L_j^{i_{\mathrm{rec}}, i_{\mathrm{exc}}}(\kappa) \cdot \begin{bmatrix} \beta_{\mathrm{exc},n',j}^{+}(\kappa) \\ \beta_{\mathrm{exc},n',j}^{-}(\kappa) \end{bmatrix} \end{aligned} \tag{3.42}$$

Substituting $\mathrm{d}^2\mathbf{k}_\parallel = \mathrm{d}\kappa\, \kappa\, \mathrm{d}\alpha$, and using

$$\mathbf{k}_\parallel \cdot \left(\mathbf{r}_{\parallel,\mathrm{rec}} - \mathbf{r}_{\parallel,\mathrm{exc}}\right) = \kappa \rho_{\mathrm{exc,rec}} \cos\left(\alpha - \phi_{\mathrm{exc,rec}}\right) \tag{3.43}$$

where $(\rho_{\mathrm{exc,rec}}, \phi_{\mathrm{exc,rec}})$ denote the polar coordinates of $\mathbf{r}_{\mathrm{rec},\parallel} - \mathbf{r}_{\mathrm{exc},\parallel}$, as well as

$$\int_0^{2\pi} \mathrm{d}\alpha\, \mathrm{e}^{\mathrm{i}\nu\alpha} \mathrm{e}^{\mathrm{i}x\cos(\alpha-\phi)} = 2\pi \mathrm{i}^{|\nu|} J_{|\nu|}(x) \mathrm{e}^{\mathrm{i}\nu\phi}, \tag{3.44}$$

where $J_n(x)$ denotes the Bessel function of the first kind and order n, the α-dependent part of the integral can be split off and evaluated analytically:

$$\begin{aligned} W_{n,n'}^{\mathrm{R}}(\mathbf{r}_{\mathrm{rec}}, \mathbf{r}_{\mathrm{exc}}) &= \frac{2}{\pi} \sum_{j=1}^{2} \int_0^{\infty} \frac{\mathrm{d}\kappa\, \kappa}{k_{z,i_{\mathrm{exc}}} k_{i_{\mathrm{exc}}}} \qquad (3.45) \\ &\quad \times \left[\beta_{\mathrm{rec},n,j}^{+,\dagger}(\kappa), \beta_{\mathrm{rec},n,j}^{-,\dagger}(\kappa)\right] \cdot L_j^{i_{\mathrm{rec}}, i_{\mathrm{exc}}}(\kappa) \cdot \begin{bmatrix} \beta_{\mathrm{exc},n',j}^{+}(\kappa) \\ \beta_{\mathrm{exc},n',j}^{-}(\kappa) \end{bmatrix} \\ &\quad \times \int_0^{2\pi} \mathrm{d}\alpha\, \mathrm{e}^{\mathrm{i}(m'-m)\alpha} \mathrm{e}^{\mathrm{i}\mathbf{k}_\parallel \cdot \left(\mathbf{r}_{\parallel,\mathrm{rec}} - \mathbf{r}_{\parallel,\mathrm{exc}}\right)} \\ &= 4\mathrm{i}^{|m'-m|} \mathrm{e}^{\mathrm{i}(m'-m)\phi_{\mathrm{exc,rec}}} \sum_{j=1}^{2} \int_0^{\infty} \frac{\mathrm{d}\kappa\, \kappa}{k_{z,i_{\mathrm{exc}}} k_{i_{\mathrm{exc}}}} J_{|m'-m|}(\kappa \rho_{\mathrm{exc,rec}}) \qquad (3.46) \\ &\quad \times \left[\beta_{\mathrm{rec},n,j}^{+,\dagger}(\kappa), \beta_{\mathrm{rec},n,j}^{-,\dagger}(\kappa)\right] L_j^{i_{\mathrm{rec}}, i_{\mathrm{exc}}}(\kappa) \begin{bmatrix} \beta_{\mathrm{exc},n',j}^{+}(\kappa) \\ \beta_{\mathrm{exc},n',j}^{-}(\kappa) \end{bmatrix}. \end{aligned}$$

3.5. Initial field coefficients

The direct and the layer system mediated initial field coefficients are derived for the cases of plane wave excitation ($\mathrm{exc} = \mathrm{init} = P$), focused beam excitation ($\mathrm{exc} = \mathrm{init} = G$, "Gaussian beam") and point dipole excitation ($\mathrm{exc} = \mathrm{init} = D$). In either case, the formalism derived in section 3.4 is applied ot obtain the expansion of the initial field in terms of regular SVWFs around $\mathbf{r}_S$.

3.5.1. Plane wave excitation

A plane wave is incident either from the bottom layer ($i_P = 0$) or from the top layer ($i_P = N$), with a linear polarization j_P, an amplitude A_P and a propagation direction given by the polar and azimuth angle (β_P, α_P). The wavevector of the incident field is

$$\mathbf{k}_{P,i_P} = \begin{cases} \begin{pmatrix} \kappa_P \cos\alpha_P \\ \kappa_P \sin\alpha_P \\ -k_{P,z,i_P} \end{pmatrix} & \text{for top illumination, } i_P = N \\ \begin{pmatrix} \kappa_P \cos\alpha_P \\ \kappa_P \sin\alpha_P \\ k_{P,z,i_P} \end{pmatrix} & \text{for bottom illumination, } i_P = 0, \end{cases} \tag{3.47}$$

where $\kappa_P = k_{i_P} \sin\beta_P$ and $k_{P,z,i_P} = \sqrt{k_{i_P}^2 - \kappa_P^2}$. The initial field reads

$$\mathbf{E}_P(\mathbf{r}) = A_P \begin{cases} \mathbf{\Phi}_{j_P}^-(\kappa_P, \alpha_P; \mathbf{r}) & i_P = N \\ \mathbf{\Phi}_{j_P}^+(\kappa_P, \alpha_P; \mathbf{r}) & i_P = 0, \end{cases} \qquad \text{for } \mathbf{r} \in \Lambda_{i_P} \tag{3.48}$$

which has the form of (2.68) for

$$z^+ = z^- = \begin{cases} +\infty & i_P = N \\ -\infty & i_P = 0 \end{cases} \tag{3.49}$$

$$\begin{bmatrix} g_{P,j}^+(\kappa,\alpha) \\ g_{P,j}^-(\kappa,\alpha) \end{bmatrix} = A_P \delta_{j,j_P} \delta^2\big(\mathbf{k}_\parallel, \mathbf{k}_{P,\parallel}\big) \mathrm{e}^{\mathrm{i}\mathbf{k}_{P,i_P}\cdot\mathbf{r}_{i_P}} \begin{bmatrix} 1 \\ 1 \end{bmatrix} \tag{3.50}$$

Inserting this into (3.22) and (3.30) yields

$$a_n^{S,P} = A_P \mathrm{e}^{\mathrm{i}\mathbf{k}_{P,i_P}\cdot\mathbf{r}_{i_P}} \big(V_{n,j_P}^+\big(\mathbf{r}_S, \mathbf{r}_P; \mathbf{k}_{P,\parallel}\big), + V_{n,j_P}^-\big(\mathbf{r}_S, \mathbf{r}_P; \mathbf{k}_{P,\parallel}\big)\big) \tag{3.51}$$

and

$$a_n^{S,\mathrm{R},P} = A_P \mathrm{e}^{\mathrm{i}\mathbf{k}_{P,i_P}\cdot\mathbf{r}_{i_P}} \Big(V_{n,j_P}^{\mathrm{R},+}\big(\mathbf{r}_S, \mathbf{r}_P; \mathbf{k}_{P,\parallel}\big), + V_{n,j_P}^{\mathrm{R},-}\big(\mathbf{r}_S, \mathbf{r}_P; \mathbf{k}_{P,\parallel}\big)\Big) \tag{3.52}$$

for $\mathbf{r}_P = (0, 0, \pm\infty)$ for the case of top and bottom illumination, respectively.

3.5.2. Focused beam excitation

A beam with Gaussian footprint (see section 2.3.1.4) is defined through its complex amplitude A_G, the direction of propagation (β_G, α_G) with $0 \leq \beta_G < \pi/2$ for beams incident from the bottom layer ($i_G = 0$) and $\pi/2 < \beta_G \leq \pi$ for beams incident from

the top layer ($i_G = N$) and finally the polarization j_G. In the layer of excitation, i.e., for $\mathbf{r} \in \Lambda_{i_G}$, the initial field takes the form of (2.68) for

$$z^+ = z^- = \begin{cases} +\infty & i_G = N \\ -\infty & i_G = 0 \end{cases} \tag{3.53}$$

and $g^{\pm}_{G,j}(\kappa, \alpha)$ as defined in (2.34). Inserting into (3.22) and (3.30) yields

$$a_n^{S,G} = \sum_{j=1}^{2} \int_{\mathbb{R}^2} \mathrm{d}^2\mathbf{k}_\parallel \left(V^+_{n,j}(\mathbf{r}_S, \mathbf{r}_G; \mathbf{k}_\parallel) g^+_{G,j}(\mathbf{k}_\parallel) + V^-_{n,j}(\mathbf{r}_S, \mathbf{r}_G; \mathbf{k}_\parallel) g^-_{G,j}(\mathbf{k}_\parallel) \right) \tag{3.54}$$

and

$$a_n^{S,\mathrm{R},G} = \sum_{j=1}^{2} \int_{\mathbb{R}^2} \mathrm{d}^2\mathbf{k}_\parallel \left(V^{\mathrm{R},+}_{n,j}(\mathbf{r}_S, \mathbf{r}_G; \mathbf{k}_\parallel) g^+_{G,j}(\mathbf{k}_\parallel) + V^{\mathrm{R},-}_{n,j}(\mathbf{r}_S, \mathbf{r}_G; \mathbf{k}_\parallel) g^-_{G,j}(\mathbf{k}_\parallel) \right) \tag{3.55}$$

for $\mathbf{r}_P = (0, 0, \pm\infty)$ for the case of top and bottom illumination, respectively. The right hand sides of (3.54) and (3.55) are evaluated by means of numerical integration.

3.5.3. Point dipole sources

The radiative decay of excited molecular states is modeled by means of electric point dipole sources, see section 1.3.2.2. For an emitter with a transition dipole moment of $\mathbf{d}_{eg}$ at location $\mathbf{r}_D$ in layer i_D one has:

$$\mathbf{j}(\mathbf{r}) = -\mathrm{i}\omega\delta(\mathbf{r} - \mathbf{r}_D)\mathbf{d}_{eg} \tag{3.56}$$

The field excited by this source can be evaluated using the dyadic Green function (2.12)

$$\mathbf{E}_D(\mathbf{r}) = \omega^2\mu_0 \mathbf{G}(\mathbf{r}, \mathbf{r}_D) \cdot \mathbf{d}_{eg}. \tag{3.57}$$

Expanding the dyadic Green function in terms of SVWFs (see (2.44)),

$$\mathbf{G}(\mathbf{r}, \mathbf{r}_D) = \mathbf{G}(\mathbf{r} - \mathbf{r}_D, \mathbf{0}) \tag{3.58}$$

$$= \frac{\mathrm{i}k}{\pi} \sum_n \mathbf{\Psi}^{(3)}_{p,l,m}(\mathbf{r} - \mathbf{r}_D) \otimes \mathbf{\Psi}^{(1)}_{p,l,-m}(\mathbf{0}) \tag{3.59}$$

such that (3.57) has the form of (3.32) with

$$b_n^D = \omega^2\mu_0 \frac{\mathrm{i}k}{\pi} \mathbf{\Psi}^{(1)}_{p,l,-m}(\mathbf{0}) \cdot \mathbf{d}_{eg} \tag{3.60}$$

and the direct and layer system mediated initial field coefficients read

$$a_n^{S,D} = \sum_{n'} W_{n,n'}(\mathbf{r}_S, \mathbf{r}_D) b^D_{n'}, \tag{3.61}$$

$$a_n^{S,\mathrm{R},D} = \sum_{n'} W^{\mathrm{R}}_{n,n'}(\mathbf{r}_S, \mathbf{r}_D) b^D_{n'}, \tag{3.62}$$

3.6. Multiple scattering coefficients

Multiple scattering implies that the scattered field (including the layer system response) from some particle S' acts as an incoming field at another particle S. As the scattered field is in general represented in terms of an outgoing spherical wave expansion, the SWE to SWE coupling operator as constructed in section 3.4.2 can directly be applied. In the vicinity of $\mathbf{r}_S$,

$$\mathbf{E}_{\mathrm{scat}}^{S'}(\mathbf{r}) = \sum_n a_n^{S,S'} \boldsymbol{\Psi}_n^{(1)}(\mathbf{r} - \mathbf{r}_S) \qquad S \neq S' \tag{3.63}$$

$$\mathbf{E}_{\mathrm{scat}}^{\mathrm{R},S'}(\mathbf{r}) = \sum_n a_n^{S,\mathrm{R},S'} \boldsymbol{\Psi}_n^{(1)}(\mathbf{r} - \mathbf{r}_S) \tag{3.64}$$

with

$$a_n^{S,S'} = \sum_{n'} W_{nn'}(\mathbf{r}_S, \mathbf{r}_{S'}) \qquad S \neq S' \tag{3.65}$$

$$a_n^{S,\mathrm{R},S'} = \sum_{n'} W_{nn'}^{\mathrm{R}}(\mathbf{r}_S, \mathbf{r}_{S'}), \tag{3.66}$$

compare (3.34) and (3.41).

3.7. Linear system

A priori, both the incoming field coefficients a_n^S and the scattered field coefficients b_n^S are unknown. For the solution of the scattering problem, it is necessary to truncate the series expansions in SVWFs at some multipole order $l_{\max}$:

$$\sum_{l=1}^{\infty} \rightarrow \sum_{l=1}^{l_{\max}} \tag{3.67}$$

This yields a finite set of unknowns $a_1^1, \ldots, a_{n_{\max}}^{N_{\mathrm{S}}}$ and $b_1^1, \ldots, b_{n_{\max}}^{N_{\mathrm{S}}}$ with $n_{\max} = 2l_{\max}(l_{\max}+2)$ such that the total number of unknowns is $4N_{\mathrm{S}}l_{\max}(l_{\max}+2)$. On the other hand, we have the same number of equations connecting the coefficients a_n^S and b_n^S, namely the T-matrix equation (3.9)

$$b_n^S = \sum_{n'} T_{nn'}^S a_{n'}^S, \tag{3.68}$$

where $T_{nn'}^S$ is the T-matrix of particle S, and the incoming field equation (3.8)

$$a_n^S = a_n^{S,\mathrm{init}} + a_n^{S,\mathrm{R},\mathrm{init}} + \sum_{S'} \sum_{n'} \left(W_{n,n'}(\mathbf{r}_S, \mathbf{r}_{S'}) + W_{n,n'}^{\mathrm{R}}(\mathbf{r}_S, \mathbf{r}_{S'}) \right) b_{n'}^{S'}. \tag{3.69}$$

Inserting (3.69) into (3.68), the incoming field coefficients a_n^S are eliminiated to end up with one set of equations for the scattered field coefficients as unknowns:

$$\sum_{S'}\sum_{n'} M_{n,n'}^{S,S'} b_{n'}^{S'} = \sum_{n'} T_{n,n'}^{S} \left(a_{n'}^{S,\mathrm{init}} + a_{n'}^{S,\mathrm{R,init}} \right) \tag{3.70}$$

with

$$M_{n,n'}^{S,S'} = \delta_{SS'}\delta_{nn'} - \sum_{n''} T_{n,n''}^{S} \left(W_{n'',n'}(\mathbf{r}_S, \mathbf{r}_{S'}) + W_{n'',n'}^{\mathrm{R}}(\mathbf{r}_S, \mathbf{r}_{S'}) \right). \tag{3.71}$$

Thereby, the multiple scattering problem has been reduced to the solution of a linear set of $2N_{\mathrm{S}} l_{\max}(l_{\max}+2)$ equations.

The solution of (3.70) provides us with the scattered field coefficients b_n^S from which all quantities of interest (electric near- and far-field, power flux, cross sections) can be derived.

3.8. Scattered far field

The far field intensity distribution of the scattered field in the top and bottom layer can be evaluated according to (compare (2.26))

$$I_{\Omega,j}(\beta,\alpha) = \frac{2\pi^2}{\omega\mu_0} k k_z^2 \begin{cases} \left| g_{\mathrm{scat},j}^{+\infty}(\kappa,\alpha) \right|^2 & \text{for } \beta \in \left[0, \frac{\pi}{2}\right] \\ \left| g_{\mathrm{scat},j}^{-\infty}(\kappa,\alpha) \right|^2 & \text{for } \beta \in \left[\frac{\pi}{2}, \pi\right] \end{cases}, \tag{3.72}$$

where $g_{\mathrm{scat},j}^{\pm\infty}(\kappa,\alpha)$ are the PVWF expansion coefficients of the scattered field at $z \to \pm\infty$. They read

$$g_{\mathrm{scat},j}^{+\infty}(\kappa,\alpha) = \sum_S \left(\delta_{Ni_S} g_{S,j}^{+}(\kappa,\alpha) + g_{S,N,j}^{\mathrm{R},+}(\kappa,\alpha) \right) \tag{3.73}$$

$$g_{\mathrm{scat},j}^{-\infty}(\kappa,\alpha) = \sum_S \left(\delta_{0i_S} g_{S,j}^{-}(\kappa,\alpha) + g_{S,0,j}^{\mathrm{R},-}(\kappa,\alpha) \right), \tag{3.74}$$

with (compare (3.39))

$$g_{S,j}^{\pm}(\kappa,\alpha) = \frac{1}{2\pi} \frac{\mathrm{e}^{-\mathrm{i}\mathbf{k}_\parallel \cdot \mathbf{r}_{S,\parallel}}}{k_{z,i_S} k_{i_S}} \sum_{n'} b_{n'}^S \mathrm{e}^{\mathrm{i}m'\alpha} \beta_{S,n',j}^{\pm}(\kappa) \tag{3.75}$$

and (compare 2.70)

$$\begin{bmatrix} g_{S,i,j}^{\mathrm{R}+}(\kappa,\alpha) \\ g_{S,i,j}^{\mathrm{R}-}(\kappa,\alpha) \end{bmatrix} = L_j^{i,i_S}(\kappa) \begin{bmatrix} g_{S,j}^{+}(\kappa,\alpha) \\ g_{S,j}^{-}(\kappa,\alpha) \end{bmatrix}. \tag{3.76}$$

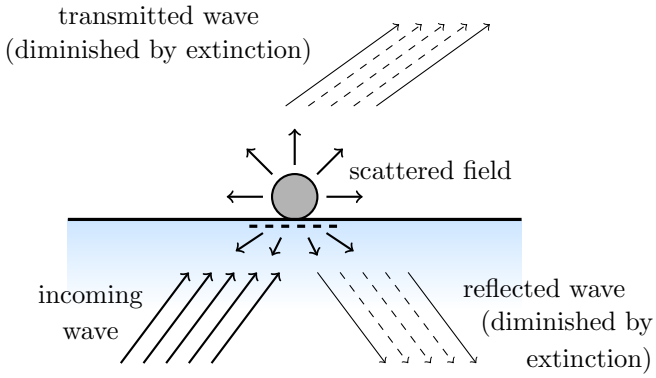

Figure 3.2. – Extinction of a plane wave by a particle on a substrate: The transmitted and the reflected wave are diminished due to scattering in other directions. The dashed line indicates the projected area A (bottom interface area).

3.8.1. Cross sections

If the initial excitation is given by a plane wave, it is natural to discuss the far field properties of a scattering structure in terms of the differential and total *scattering cross section*, as the incoming wave is specified by an intensity (power per area), whereas the scattered field is characterized by a power, such that the scattered signal divided by the initial signal yields an area. Without loss of generality I assume that the initial plane wave is incident from the (dielectric) bottom layer and propagating in the forward direction, see figure 3.2:

$$i_P = 0 \tag{3.77}$$

$$\beta_P < \frac{\pi}{2} \tag{3.78}$$

$$k_0 \in \mathbb{R} \tag{3.79}$$

3.8.1.1. Scattering cross section

The power of the plane wave per bottom interface area reads

$$I_{A,\mathrm{init}} = \frac{\mathrm{d}P_{\mathrm{init}}}{\mathrm{d}A} = \frac{k_0}{2\omega\mu_0}\cos\beta_P |A_P|^2. \tag{3.80}$$

The differential scattering cross section (DSC) can then be defined as

$$\begin{aligned}\sigma_{\Omega,\mathrm{scat}}(\beta,\alpha) &= I_{A,\mathrm{init}}^{-1}\frac{\mathrm{d}\left\langle \Phi_{\mathrm{scat},i_\beta}\right\rangle}{\mathrm{d}\Omega} \\ &= I_{A,\mathrm{init}}^{-1}\sum_{j=1}^{2} I_{\Omega,j}(\beta,\alpha),\end{aligned} \tag{3.81}$$

where $i_\beta = N$ for $\beta < \pi/2$ and $i_\beta = 0$ for $\beta > \pi/2$ and $\langle \Phi_{\mathrm{scat},i} \rangle$ is the time-averaged radiant flux of the scattered field in layer i, compare (2.25).

If the top layer is absorbing, no far field exists in that layer, such that

$$\sigma_{\Omega,\mathrm{scat}}(\beta, \alpha) = 0 \qquad \text{for } \beta < \frac{\pi}{2} \tag{3.82}$$

The total scattering cross section is simply the integral over the differential cross section:

$$\sigma_{\mathrm{scat}} = \int \mathrm{d}^2\Omega \sigma_{\Omega,\mathrm{scat}}(\beta, \alpha) \tag{3.83}$$

The above definitions are similar to the usual definition of the scattering cross section for particles in free space. The most important difference is that the intensity of the initial wave refers to the area of the planar interfaces and not to the area of the incoming wave fronts, such that an additional factor of $\cos\beta_P$ appears. Note that other publications might employ a different definition [153].

3.8.1.2. Extinction cross section

Usually, the extinction cross section is defined as the sum of scattering and absorption cross section. However, the definition or evaluation of the latter is not straightforward in the context of particles inside a planarly layered medium. I therefore prefer to use what is commonly referred to as the "optical theorem" for the definition of the extinction cross section. It also comes closer to the very meaning of extinction which is to take away[4] power from the initial wave. The starting point is expression (2.24) for the bottom far field power:

$$\langle P_{\mathrm{bot}} \rangle = -\frac{2\pi^2}{\omega\mu_0} \sum_{j=1}^{2} \int_{|\mathbf{k}_\parallel| \le k_0} \mathrm{d}^2\mathbf{k}_\parallel k_{z,0} \left| g_j^{-\infty}(\kappa, \alpha) \right|^2, \tag{3.84}$$

where $g_j^{-\infty}$ denotes the plane wave expansion coefficients of the *total downgoing field* in the bottom layer. It is the sum of the reflected initial wave and the scattered field propagated to the bottom layer:

$$g_j^{-\infty}(\kappa, \alpha) = g_{P,j}^{\mathrm{R}-}(\kappa, \alpha) + g_{\mathrm{scat},j}^{-\infty}(\kappa, \alpha) \tag{3.85}$$

Accordingly,

$$\left| g_j^{-\infty}(\kappa, \alpha) \right|^2 = \left| g_{P,j}^{\mathrm{R}-}(\kappa, \alpha) \right|^2 + \left| g_{\mathrm{scat},j}^{-\infty}(\kappa, \alpha) \right|^2 + 2\,\mathrm{Re}\left(g_{P,j}^{\mathrm{R}-}(\kappa, \alpha) g_{\mathrm{scat},j}^{-\infty *}(\kappa, \alpha) \right), \tag{3.86}$$

[4] It turns out that in the context of lossy layered media, the extinction can be negative such that the scattering particles lead to more reflection compared to the pure layered medium without the particles.

with the asterisk denoting complex conjugation. The first two terms in the right hand side of (3.86) correspond to the reflected initial wave and to the scattered field's radiant intensity, respectively. The third term ("cross term"), on the other hand, correspond to the extinction of the reflected initial wave through scattering. For the reflected initial wave, we have

$$g^{\mathrm{R}-}_{P,j}(\kappa,\alpha) = r_{j_P}(\kappa_P) A_P \delta_{j,j_P} \delta^2\big(\mathbf{k}_\parallel, \mathbf{k}_{P,\parallel}\big) \mathrm{e}^{\mathrm{i}\mathbf{k}_{P,i_P}\cdot\mathbf{r}_{i_P}}, \tag{3.87}$$

compare (3.50), where $r_{j_P}(\kappa)$ denotes the amplitude reflection coefficient of the planarly layered medium for a plane wave incident from the bottom. It can be computed by means of the scattering matrix algorithm, compare section 2.4.2. Thus, the contribution of the cross terms to the right hand side of (3.84) evaluates to

$$\langle P_{\mathrm{bot,extinct}}\rangle = -\frac{4\pi^2 k_{z,0}}{\omega\mu_0} \operatorname{Re}\left(A_P\, r_{j_P}(\kappa_P)\, \mathrm{e}^{\mathrm{i}\mathbf{k}_{P,i_P}\cdot\mathbf{r}_{i_P}} g^{-\infty *}_{\mathrm{scat},j}(\kappa_P,\alpha_P)\right). \tag{3.88}$$

If the top layer is lossless, too, the concept of extinction can also be applied to the transmitted wave. We start from the top layer far field power:

$$\langle P_{\mathrm{top}}\rangle = \frac{2\pi^2}{\omega\mu_0} \sum_{j=1}^{2} \int_{|\mathbf{k}_\parallel|\le k_N} \mathrm{d}^2\mathbf{k}_\parallel k_{z,N} \left|g^{+\infty}_j(\kappa,\alpha)\right|^2 \tag{3.89}$$

with

$$\left|g^{+\infty}_j(\kappa,\alpha)\right|^2 = \left|g^{\mathrm{R}+}_{P,N,j}(\kappa,\alpha)\right|^2 + \left|g^{+\infty}_{\mathrm{scat},j}(\kappa,\alpha)\right|^2 + 2\operatorname{Re}\left(g^{\mathrm{R}+}_{P,N,j}(\kappa,\alpha) g^{+\infty *}_{\mathrm{scat},j}(\kappa,\alpha)\right), \tag{3.90}$$

where this time

$$g^{\mathrm{R}-}_{P,N,j}(\kappa,\alpha) = t_{j_P}(\beta_P) A_P \delta_{j,j_P} \delta^2\big(\mathbf{k}_\parallel, \mathbf{k}_{P,\parallel}\big) \mathrm{e}^{\mathrm{i}\mathbf{k}_{P,i_P}\cdot\mathbf{r}_{i_P}}, \tag{3.91}$$

corresponds to the transmitted initial wave with $t_{j_P}(\kappa_P)$ denoting the layer system's amplitude transmission coefficient which can again be evaluated with the scattering matrix formalism.

The extinction of the transmitted wave thus reads in analogy to (3.88)

$$\langle P_{\mathrm{top,extinct}}\rangle = \frac{4\pi^2 k_{z,N}}{\omega\mu_0} \operatorname{Re}\left(A_P\, t_{j_P}(\kappa_P)\, \mathrm{e}^{\mathrm{i}\mathbf{k}_{P,i_P}\cdot\mathbf{r}_{i_P}} g^{+\infty *}_{\mathrm{scat},j}(\kappa_P,\alpha_P)\right). \tag{3.92}$$

This allows us to finally define the *reflection extinction cross section*

$$\sigma_{\mathrm{refl}} = I^{-1}_{A,\mathrm{init}} \langle P_{\mathrm{bot,extinct}}\rangle \tag{3.93}$$

and the *transmission extinction cross section*

$$\sigma_{\mathrm{transm}} = I^{-1}_{A,\mathrm{init}} \langle P_{\mathrm{top,extinct}}\rangle. \tag{3.94}$$

In the case of scattering in free space, the conservation of energy for a lossless scattering particle implies that the extinction cross section equals the scattering cross section. This is not the case in the presence of a planarly layered medium. Even if all materials are lossless, the incoupling of power into waveguide modes can cause an effective absorption. However, in the case lossless materials and a layer system that does not support waveguide modes, the conservation of energy yields

$$\sigma_{\mathrm{scat}} = \sigma_{\mathrm{refl}} + \sigma_{\mathrm{transm}} \tag{3.95}$$

3.9. Scattered near field

The total electric field at any point $\mathbf{r}$ (the *fieldpoint*, located in layer i) is given by the sum of the initial field (propagated through the layer system) plus the scattered field of all particles (also propagated through the layer system). If the fieldpoint is in the same layer as the source of the initial excitation or the scattering particles, the respective direct term has to be added, compare (3.3).

Whereas the direct scattered field $\mathbf{E}^S_{\mathrm{scat}}(\mathbf{r})$ of each particle is directly evaluated from b^S_n using (3.5), the layer system mediated scattered field $\mathbf{E}^{\mathrm{R},S}_{\mathrm{scat}}(\mathbf{r})$ is evaluated through its PVWF expansion

$$\mathbf{E}^{\mathrm{R}}_S(\mathbf{r}) = \sum_{j=1}^{2} \int_{\mathbb{R}^2} \mathrm{d}^2\mathbf{k}_\parallel \left[\boldsymbol{\Phi}^+_j\left(\mathbf{k}_\parallel; \mathbf{r}-\mathbf{r}_i\right), \boldsymbol{\Phi}^-_j\left(\mathbf{k}_\parallel; \mathbf{r}-\mathbf{r}_i\right)\right] \cdot \begin{bmatrix} g^{\mathrm{R}+}_{S,i,j}\left(\mathbf{k}_\parallel\right) \\ g^{\mathrm{R}-}_{S,i,j}\left(\mathbf{k}_\parallel\right) \end{bmatrix}, \tag{3.96}$$

with $g^{\mathrm{R}\pm}_{S,i,j}\left(\mathbf{k}_\parallel\right)$ computed according to (3.75) and (3.76).

The so computed scattered near field is valid everywhere except inside the circumscribing sphere of the particles, where (3.5) does in general not converge.

3.10. Numerical considerations

In the simulation of scattering layers with a large number of scattering centers, the time that is needed obtain a solution of (3.70), as well as its accuracy, critically depend on a numerically favorable implementation. Consider for example a scattering layer model including $N_{\mathrm{S}} = 5000$ spheres and a truncation multipole order of $l_{\max} = 3$ which corresponds to $n_{\max} = 30$. Accordingly, the master matrix M is of dimension $N_{\mathrm{S}} n_{\max} = 150,000$. However, the computation of each entry involves the numerical quadrature of a one-dimensional integral (compare (3.46)) such that in total 22.5 billion so called Sommerfeld integrals would have to be evaluated, resulting in a considerable computational effort. Another complication arises from memory limitations: the full matrix M, stored in (complex) single precision, would already require $180\,\mathrm{GB}$.

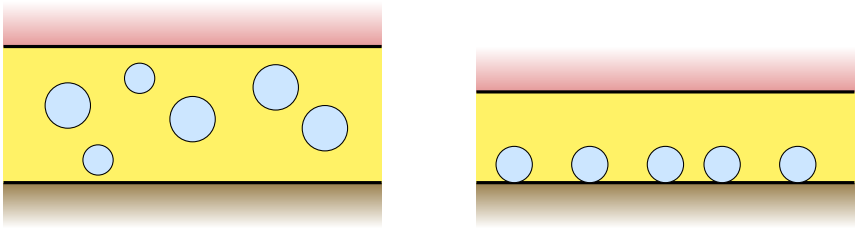

Figure 3.3. – Single volumetric (left) and flat (right) scattering layer.

3.10.1. Lookup table for particle coupling matrices

The layer system mediated coupling matrix $W_{n,n'}^{S,\mathrm{R},S'}$ depends on the positions of both particles, S and S', in the layer system. Due to the lateral translation symmetry, only the relative lateral displacement counts, such that $W_{n,n'}^{S,\mathrm{R},S'}$ depends on four position parameters: $\rho_{S'S}$, $\phi_{S'S}$ (the polar coordinates of $\mathbf{r}_{\parallel,S} - \mathbf{r}_{\parallel,S'}$), z_S and $z_{S'}$. In fact, it can be written as

$$W_{n,n'}^{S,\mathrm{R},S'} = 4\mathrm{i}^{|m'-m|}\mathrm{e}^{\mathrm{i}(m-m')\phi_{S'S}} \sum_{j=1}^{2} I_{j,n,n'}\left(\rho_{S'S}, z_S, z_{S'}\right) \tag{3.97}$$

with the Sommerfeld integral

$$I_{j,n,n'}\left(\rho_{S'S}, z_S, z_{S'}\right) = \int_0^\infty \frac{\mathrm{d}\kappa\,\kappa}{k_{z,i_{S'}} k_{i_{S'}}} J_{|m'-m|}(\kappa\rho_{S'S}) \times \left[\beta_{S,n,j}^{+,\dagger}, \beta_{S,n,j}^{-,\dagger}\right] L_j^{i_S,i_{S'}}(\kappa) \begin{bmatrix}\beta_{S',n',j}^{+}(\kappa)\\ \beta_{S',n',j}^{-}(\kappa)\end{bmatrix}, \tag{3.98}$$

compare (3.46).

3.10.1.1. Single volumetric scattering layers

If we assume that the particles S and S' are located in the same layer $i_S = i_{S'}$, the Sommferfeld integral can be split into two parts, depending on $z_S + z_{S'}$ and $z_S - z_{S'}$, respectively:

$$I_{j,n,n'}\left(\rho_{S'S}, z_S, z_{S'}\right) = I_{j,n,n'}^{+}\left(\rho_{S'S}, z_S + z_{S'}\right) + I_{j,n,n'}^{-}\left(\rho_{S'S}, z_S - z_{S'}\right) \tag{3.99}$$

with

$$I_{j,n,n'}^{\pm}\left(\rho, z\right) = \int_0^\infty \frac{\mathrm{d}\kappa\,\kappa}{k_{z,i_S} k_{i_S}} J_{|m'-m|}(\kappa\rho) f_{j,n,n'}^{\pm}(z) \tag{3.100}$$

and

$$f^{+}_{j,n,n'}(z) = \left[L_j^{i_S}(\kappa)\right]_{1,2} B^{\dagger}_{n,j}(k_{z,i_S}/k_{i_S}) B_{n',j}(-k_{z,i_S}/k_{i_S}) \mathrm{e}^{\mathrm{i}k_{z,i_S}\left(z-2z_{i_S}\right)} + \left[L_j^{i_S}(\kappa)\right]_{2,1} B^{\dagger}_{n,j}(-k_{z,i_S}/k_{i_S}) B_{n',j}(k_{z,i_S}/k_{i_S}) \mathrm{e}^{-\mathrm{i}k_{z,i_S}\left(z-2z_{i_S}\right)} \tag{3.101}$$

$$f^{-}_{j,n,n'}(z) = \left[L_j^{i_S}(\kappa)\right]_{1,1} B^{\dagger}_{n,j}(k_{z,i_S}/k_{i_S}) B_{n',j}(k_{z,i_S}/k_{i_S}) \mathrm{e}^{\mathrm{i}k_{z,i_S}z} + \left[L_j^{i_S}(\kappa)\right]_{2,2} B^{\dagger}_{n,j}(-k_{z,i_S}/k_{i_S}) B_{n',j}(-k_{z,i_S}/k_{i_S}) \mathrm{e}^{-\mathrm{i}k_{z,i_S}z}. \tag{3.102}$$

The integrals $I^{\pm}_{n,n'}$ thus only depend on two parameters each, which allows to compute them on a grid (ρ_i, z_i) and then evaluate the actual Sommerfeld integrals by means of interpolation from the so generated lookup table. This approach can greatly reduce the number of integrals that needs to be computed and thereby enhance the speed of the overall simulation time for scattering layers by orders of magnitude. The dimension of the grid (ρ_i, z_i) is $2d_{i_S}\rho_{\max}/\Delta z\Delta\rho$ such that the lookup table in (complex) single precision occupies $32d_{i_S}\rho_{\max}/\Delta z\Delta\rho$ bytes of the main memory. For example, to model a scattering layer with thickness $d_{i_S} = 5\,\mu\mathrm{m}$ up to a cylindrical radius of $\rho_{\max} = 10\,\mu\mathrm{m}$ with a lookup table resolution $\Delta\rho = \Delta z = 1\,\mathrm{nm}$, $1.6\,\mathrm{GB}$ are required. The size of the lookup table can be a limiting factor if very thick scattering layers are modeled and the calculations are performed on a graphics processing unit, with typically less memory compared to the host RAM.

3.10.1.2. Flat scattering layers

In some applications, all scattering particles are aligned at the same height $z_S = z$. I refer to this case as *flat scattering layers*. Then, the Sommerfeld integrals for the particle coupling only depend on a single parameter, the radial coordinate ρ:

$$I_{j,n,n'}\left(\rho_{S'S}, z_S, z_{S'}\right) = I_{j,n,n'}\left(\rho_{S'S}\right). \tag{3.103}$$

This does not only save memory, but also leads to a much faster evaluation of the particle coupling, as only a one dimensional interpolation is necessary compared to a two dimensional interpolation in the case of volumetric scattering layers.

3.10.2. Evaluation of Sommerfeld integrals

Integrals of type (3.46) are called *Sommerfeld integrals* with reference to a famous article by Arnold Sommerfeld about wireless telegraphy [91].

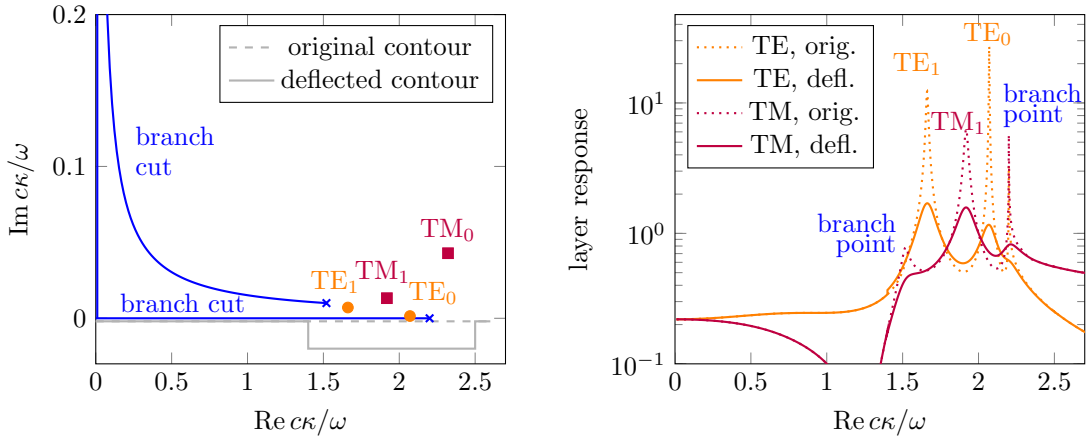

Figure 3.4. – Branch cuts and waveguide mode singularities in the complex κ plane for a 3-layer system comprising a substrate ($n = 1.52 + 0.01\mathrm{i}$), a $300\,\mathrm{nm}$ core layer ($n = 2$) and a metal topping ($n = 1 + 6.6\mathrm{i}$) at a vacuum wavelength of $550\,\mathrm{nm}$.

3.10.2.1. Singularities of the layer system response

A straightforward approach to the numeric integration would be to evaluate the integrand along an equidistant grid $\kappa_i = i\Delta\kappa$ for $i = 0, \ldots, \kappa_{\max}/\Delta\kappa$ and then apply e.g. the trapezoidal rule to compute the integral. However, in the vicinity of waveguide mode and branch point singularities the integrand is a rapidly varying function of κ such that a very fine sampling of the integrand would be required in order to achieve a reasonable accuracy. A simple strategy to avoid the vicinity of the singularities is to integrate along a complex contour $C(\gamma)$ which is deflected away from the real axis into the lower complex half plane, see figure 3.4. As the waveguide mode singularities as well as the branch cuts associated with square roots are located in the upper complex half plane, the integrand is an analytical function in the lower half plane. By virtue of Cauchy's theorem, the integral along the deflected contour thus yields the same result as along the real axis, but it is better suited for numerical evaluation.

The above described approach is easy to implement and suitable from a practical perspective. Note that more sophisticated methods exist, and in fact a large body of literature is devoted to the numerical evaluation of Sommerfeld integrals or their analytical approximation, see for example [127, 154–156]. Some key concepts are the extraction and analytical treatment of singular terms, or the integration along a steepest-descent path to achieve fast convergence. However, these methods require a considerable analytical and programmatic effort, such as book-keeping of singularities. But thanks to the lookup table approach described above, the evaluation of Sommerfeld integrals is not the computational bottleneck during the simulation of scattering layers including many particles. Therefore, the simple deflection of the integral path together with the trapezoidal rule (which can efficiently be implemented in terms of matrix-vector products) is a good choice.

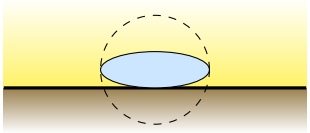

Figure 3.5. – Oblate particle near interface.

3.10.2.2. Truncation of the plane wave expansion

Another issue in the numerical evaluation of Sommerfeld integrals is the decision where to truncate, that is, up to which maximal wavenumber $k_{\max}$ the integrand is considered:

$$\int_0^{\infty} \mathrm{d}\kappa \to \int_0^{k_{\max}} \mathrm{d}\kappa \tag{3.104}$$

The range between $\kappa = 0$ and $\kappa = k_{i_{\mathrm{exc}}}$ (the wavenumber in the excitation layer) corresponds to propagating waves, whereas in-plane wavenumbers $\kappa > k_{i_{\mathrm{exc}}}$ correspond to evanescent waves which are relevant for the excitation's near field. Thus, the integral should not be truncated at a value $\kappa < k_{i_{\mathrm{exc}}}$. Further, if the plane wave expansion is truncated at a too low $\kappa > k_{i_{\mathrm{exc}}}$, the near field of the excitation is not correctly accounted for. This is tolerable, if the nearest interface is not close. However, for particles very close to an interface, a larger portion of the evanescent part of the angular spectrum needs to be accounted for to correctly evaluate the reflection of the field by that interface.

On the other hand, special care has to be taken in the case of oblate particles close to an interface. As the expansion of the scattered field in outgoing SVWFs is in general not valid inside the circumscribing sphere of the particle, the case that the circumscribing sphere intersects with the interface (compare figure 3.5) is critical [157]. Even in this case, the presented formalism can be applied, as in contrast to the expansion in SVWFs, the expansion in PVWFs is valid also in the near field [158]. But the angular spectrum converges only point-wise with increasing multipole order $l_{\max}$. As a consequence, it is important to choose $k_{\max}$ within the regime where convergence of the angular spectrum has already occurred [159]. As a rule of thumb, one can use the estimate [160]

$$k_{\max} = (0.38 l_{\max} + 1) R^{-1} + 0.03 k^2 R, \tag{3.105}$$

where $l_{\max}$ is the SVWF truncation order, R is the radius of the circumscribing sphere of the particle and k is the wavenumber outside the particle.

To conclude, the Sommerfeld integral truncation should not be chosen too small (for fields originating from close to an interface) and not too large (for oblate scattering particles close to an interface) for a fixed SVWF truncation order $l_{\max}$.

3.10.3. Solution of the linear system

For moderate particle numbers, the system of linear equations (3.70) can be solved by means of direct methods, for example using LU-factorization. As the coefficients of the linear system $M_{n,n'}^{S,S'}$ depend only on the T-matrices and the coupling matrices $W_{n,n'}^{S,S'}$ and $W_{n,n'}^{S,\mathrm{R},S'}$, this approach has the advantage that for repeated simulations with modified initial field coefficients $a_{\mathrm{init},n}^{S}$ and $a_{\mathrm{init},n}^{S,\mathrm{R}}$, the LU-factorization can be reused - for example during a sweep over the incident angle of an initial beam or over the position of an initial dipole.

For very large particle numbers, it is favourable to use iterative solvers like the *generalized minimal residual method* (GMRES) which can approximate the solution of the linear system to the required accuracy with fewer operations than would be necessary to exactly solve it. As only matrix-vector products are performed, the linear coefficients can be computed "on the fly" during each iteration. This allows the solution of systems with so many unknowns that the coupling matrices cannot be stored in memory. Clearly, the computational bottleneck of such simulations is the evaluation of matrix-vector products of the type

$$\sum_{S'} \sum_{n'} M_{n,n'}^{S,S'} x_{n'}^{S'} \tag{3.106}$$

and a suitable implementation of this operation is critical for the performance in the case of large particle numbers.

4. The Smuthi software package

This chapter introduces Smuthi, a simulation software for light scattering by particles near planar interfaces. It covers possible use cases, gives an overview on the program structure (section 4.1) and discusses the validation of simulation results (section 4.2)

Smuthi[1] is a free Python package for the simulation of scattering of plane waves, Gaussian beams or point dipole emission by spherical, spheroidal or cylindrical particles near or between planar layer interfaces. It was developed during the doctorate research in preparation of this thesis with the aim to allow the simulation of OLEDs with internal scattering layers – but its use is not restricted to that configuration. Other possible use cases include solar cells with scattering layers, the design of nano structures for surface enhanced Raman spectroscopy, meta-surfaces for a tailored scattering response and any other application with particles on or close to a substrate or inside a system of planar layers.

In fact, Smuthi succeeds an unpublished prototype code that was previously implemented in Matlab and that was used to compute the results published in [78,126,127, 159]. The decision to reimplement the software from the scratch was guided by the aim to make it ...

- accessible: Smuthi requires no proprietary software and can be downloaded from the *Python Package Index* (PyPI) and installed with the *pip package management system* using a single command: `pip install smuthi`.
- easy: The usage should be straightforward also without programming experience. The online documentation [161] contains detailed instructions how to run a simulation.
- transparent: Other programmers should be able to understand the data structure without too much effort. The software is designed following an object oriented programming style. Using the *Sphinx Python Documentation Generator* package [162] with the *autodoc* extension, a detailed documentation of the Smuthi application programming interface (API) is maintained and can be viewed either directly in the source code or from the online documentation [161]. Contributions from other programmers can be added through pull requests to the Git online repository [163].

[1] The acronym stands for "Scattering by multiple particles in thin-film systems"

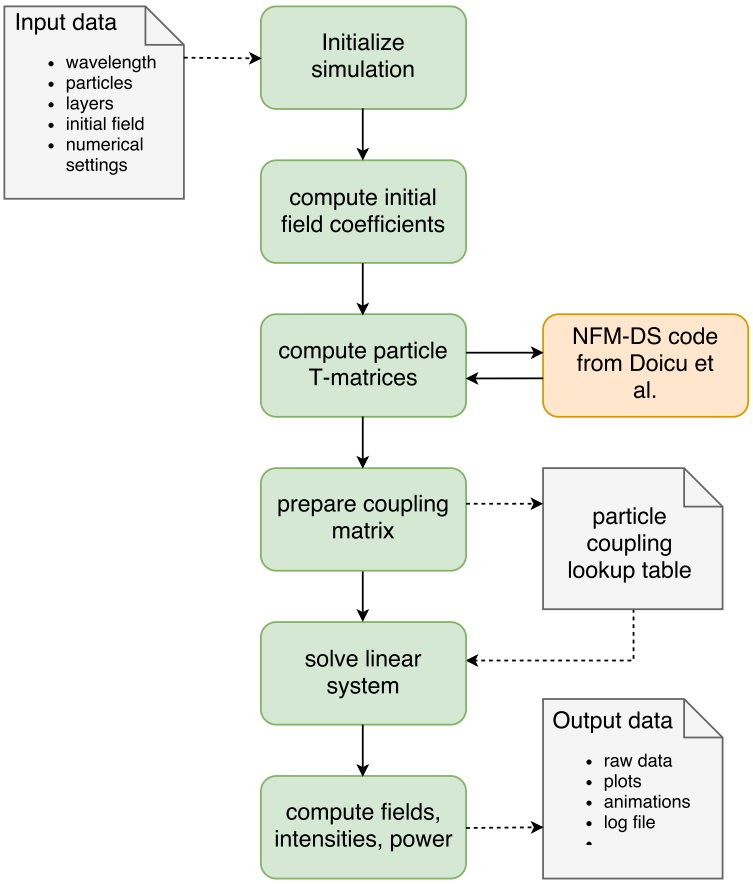

Figure 4.1. – Smuthi flowchart

- reliable: An extensive set of unit tests and system tests ensures that the individual modules behave as expected. However, no software that is complex enough is free of bugs, and I cannot guarantee correct behaviour in all possible cases. In addition, Smuthi does not grant input testing, and sloppy parameter input or the usage out of the intended scope (for example, overlapping particles) lead to wrong simulation results.
- efficient: Especially for the case of many scattering particles, emphasis was laid on an efficient implementation, such that simulations involving several thousand wavelength scale scattering particles in a thin-film system are feasible in a reasonable computation time. Here, the two most important features are the evaluation of particle coupling by interpolation from a precomputed lookup table (see section 3.10.1) and shifting computationally heavy tasks to the graphics processing unit (GPU).
- flexible: Smuthi has a built-in interface to the NFM-DS Fortran code by Adrian

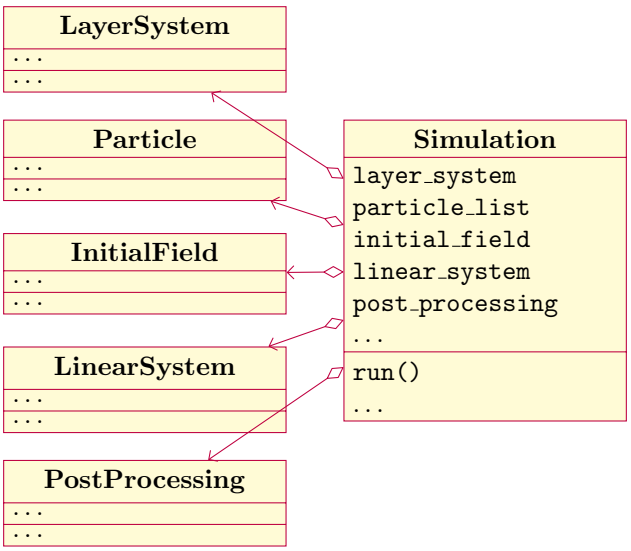

Figure 4.2. – Aggregation of the simulation class. Only a selection of class attributes and methods are shown.

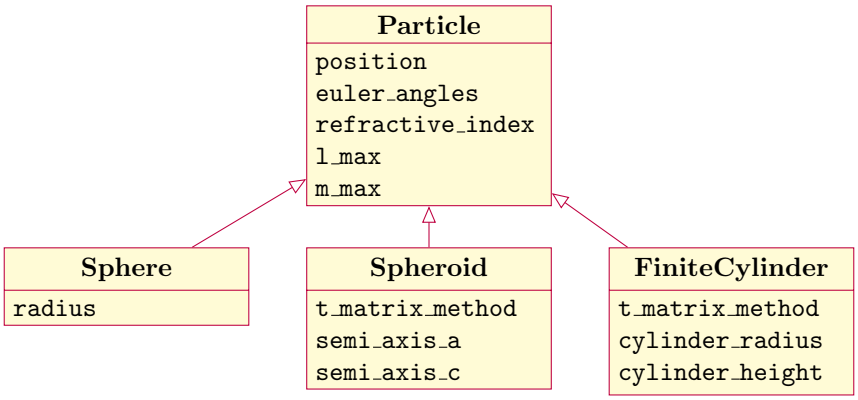

Figure 4.3. – Inheritance structure of the particle classes. Only class attributes are shown, whereas methods are hidden.

Doicu, Thomas Wriedt and Yuri Eremin [133]. This interface was implemented in collaboration with Dominik Theobald (see also his Master thesis [164]) and allows the simulation of speroidally and cylindrically shaped scattering particles. In general, due to Smuthi's object oriented design paradigm (see next section), it is relatively easy to add new functionality (like for example special beam shapes as the initial field).

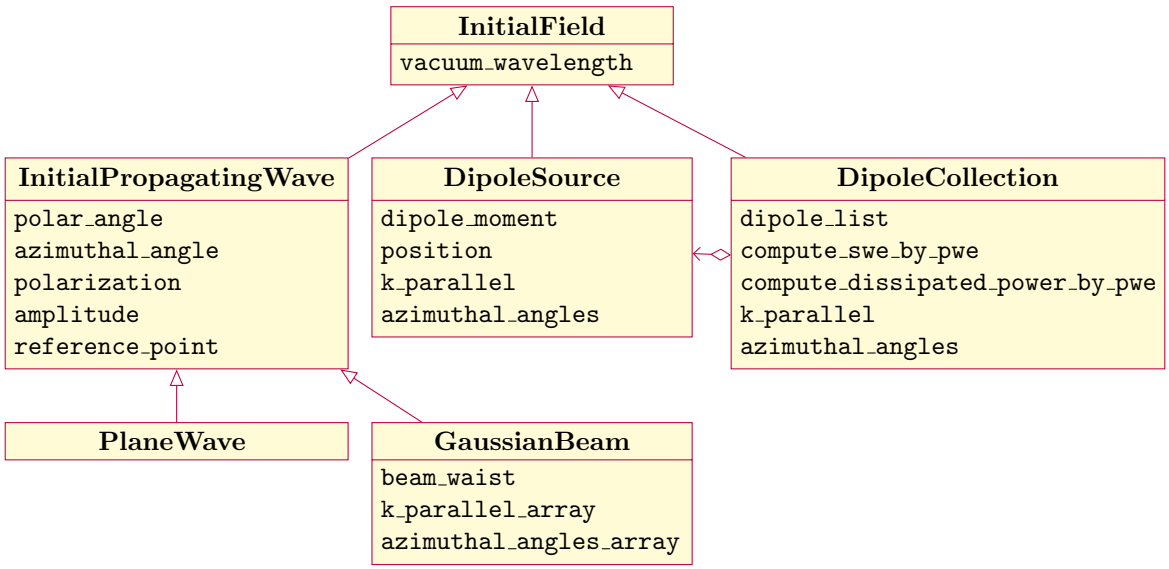

Figure 4.4. – Inheritance structure of the initial field classes. Only class attributes are shown, whereas methods are hidden.

4.1. Program structure

Smuthi was implemented following an object oriented programming style. Its data structure relies on the following classes:

`Simulation`: The central simulation object, gathering all information at one spot. Figure 4.2 shows how this class has instances of other classes as attributes. It has a `run()` method that triggers the the solution of (3.70), and the post processing to yield the desired output quantities like far field power flux, cross sections, near field distribution or dipole dissipated power. Figure 4.1 illustrates the sequence of calculations as a program flowchart.

`LayerSystem`: This class manages everything that has to do with the propagation of fields through the planarly layered background medium. It contains the layer thicknesses and refractive indices as attributes and provides a `response()` method that evaluates the layer system response equation (2.70).

`Particle`: The particle class, which decays into subclasses as shown in figure 4.3, manages all properties of an individual particle. Its attributes include the geometric and material parameters, but also the T-matrix as well as the incoming and scattered field at the particle. The latter are instances of the `SphericalWaveExpansion` class.

`InitialField`: This class also decays into subclasses as shown in figure 4.4. It manages the initial excitation and provides methods to compute a regular `SphericalWaveExpansion`, see section 3.5, as well as a `PlaneWaveExpansion`.

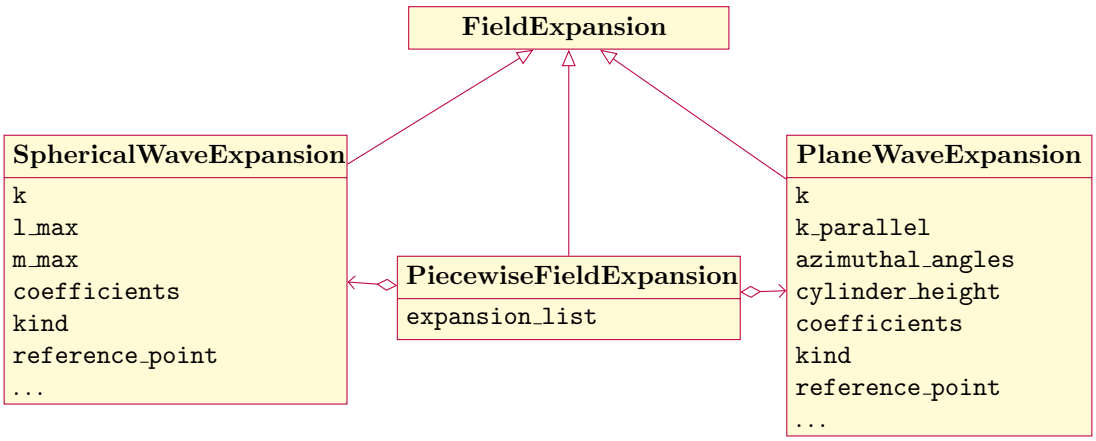

Figure 4.5. – Inheritance structure of the field expansion classes. Only class attributes are shown, whereas methods are hidden.

`FieldExpansion`: This class is an abstract representation of an expansion of the electric field in some basis function. It can be a `SphericalWaveExpansion` like in (2.42) or a plane wave expansion like in (2.18). In either case, an instance of the respective class contains the expansion coefficients as attributes and provides methods to evaluate the electric field at a given point. There also exist functions to convert spherical into plane wave expansions and vice versa, according to the formulas presented in section 2.3.3. In addition, there exist also `PiecewiseFieldExpansion` which reflect the fact that no field expansion is valid everywhere – for example a plane wave expansion is in general valid only in one of the layers. An object of the `PiecewiseFieldExpansion` contains a list of `FieldExpansion` objects as an attribute, together with the information about the respective domains of validity. See figure 4.5 for an inheritance diagram.

`LinearSystem`: This class manages the assembly and the solution of the master equation (3.70). Its attributes include the system `t_matrix` as well as the system `coupling_matrix` which are represented as instances of the `SystemMatrix` class.

`SystemMatrix`: A system matrix is a matrix of full system size, i.e., of dimension $2N_\mathrm{S}l_\mathrm{max}(l_\mathrm{max}+2)$, like for example the master matrix $M^{S,S'}_{n,n'}$ of (3.70). Depending on the simulation geometry (volumetric or flat scattering layer?) and on the solution strategy, a system matrix can either be stored explicitly in memory or as an abstract linear operator providing a matrix vector product method. Accordingly, the `SystemMatrix` class decays in several subclasses which specify to the different solution strategies.

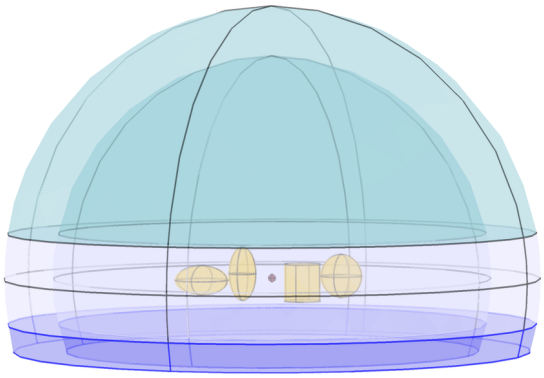

Figure 4.6. – Screenshot of the COMSOL model geometry.

4.2. Validation

The validation process should verify that the software correctly solves Maxwell's equation and returns correct power, near- and far-field figures. This can be done either by testing the internal consistency in terms of energy conservation or by comparison to results from other established software packages.

bottom layer refractive index:	$1 + 6\mathrm{i}$
middle layer refractive index:	2
top layer refractive index:	1.5
particle refractive index:	3 or $1 + 6\mathrm{i}$
vacuum wavelength:	$550\,\mathrm{nm}$
middle layer thickness:	$500\,\mathrm{nm}$
sphere radius:	$120\,\mathrm{nm}$
oblate spheroid horizontal half axis:	$150\,\mathrm{nm}$
oblate spheroid vertical half axis:	$80\,\mathrm{nm}$
prolate spheroid horizontal half axis:	$80\,\mathrm{nm}$
prolate spheroid vertical half axis:	$150\,\mathrm{nm}$
cylinder radius:	$100\,\mathrm{nm}$
cylinder height:	$200\,\mathrm{nm}$

Table 4.1. – Parameters of the validation model.

4.2.1. Conservation of energy

If conservation of energy is fulfilled for a lossless structure, it is still not guaranteed that the solution is correct, but many errors can be ruled out by this consistency check. Note that a lossless structure means that

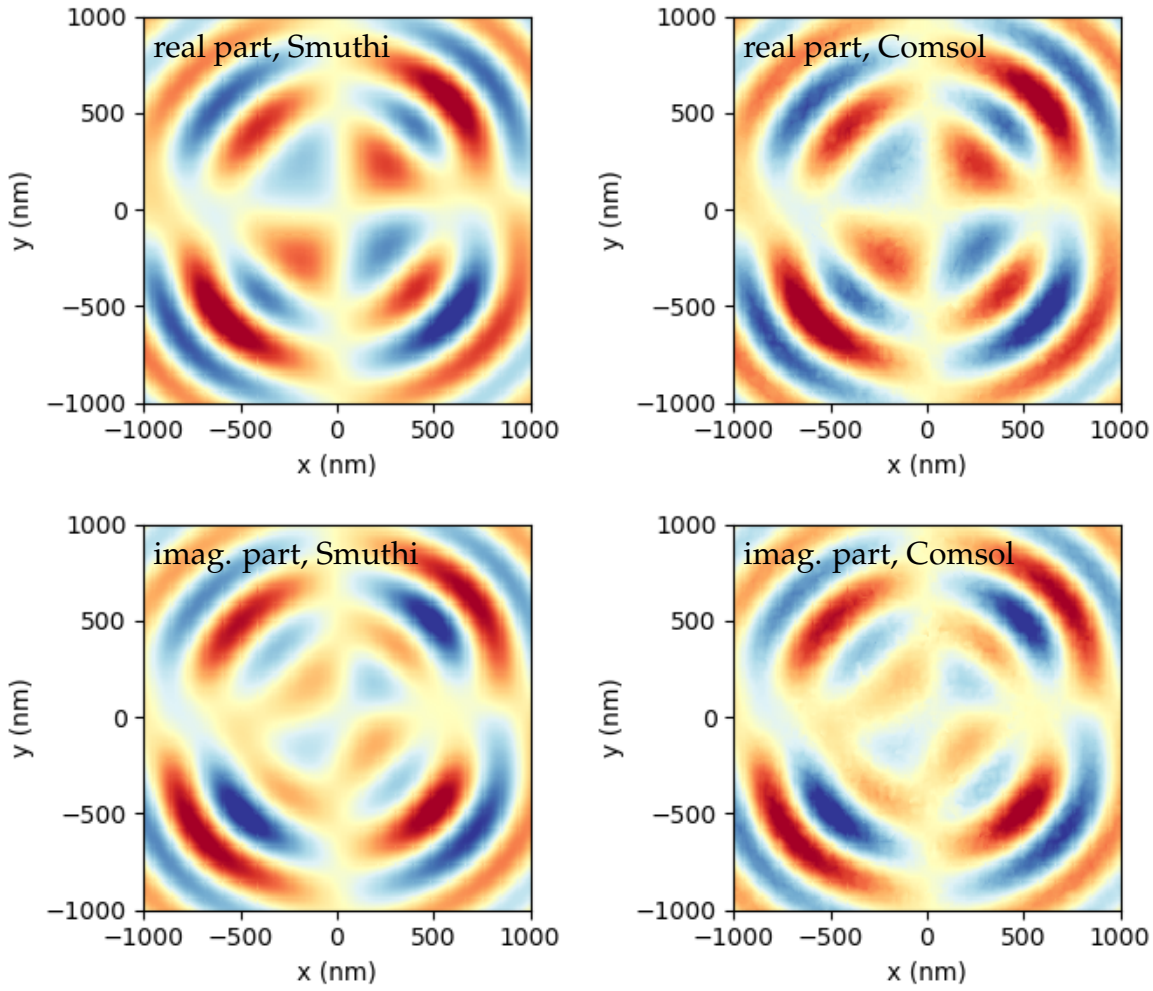

Figure 4.7. – E_y as computed with Smuthi (left) and COMSOL (right) for dielectric scattering particles ($n = 3$).

1. All layers have a real refractive index.
2. All particles have a real refractive index.
3. The layer system does not support waveguiding, because power coupled into waveguide modes does not appear in the far field balance.

In the context of plane wave excitation, conservation of energy means that the extinction cross section equals the scattering cross section (optical theorem), see sections 3.8.1.1 and 3.8.1.2. For Gaussian beam excitation, conservation of energy means that the total reflected power plus the total transmitted power equals the total power of the initial beam. Finally, for a point dipole source or a collection of such, conservation of energy means that the dissipated power equals the integrated radiative power according to Poynting's theorem, see section 1.3.2.2. Three Python test modules that

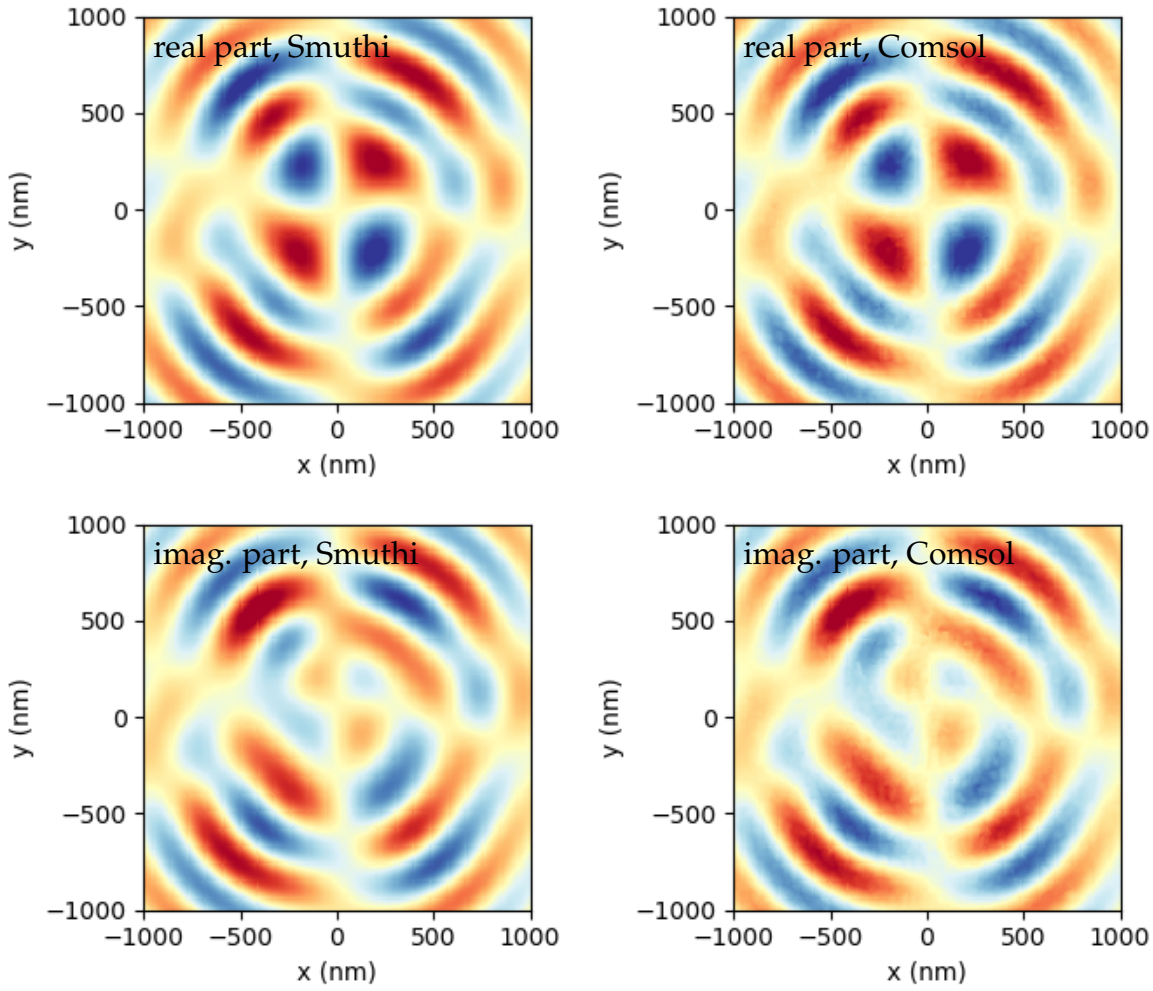

Figure 4.8. – E_y as computed with Smuthi (left) and COMSOL (right) for metallic scattering particles ($n = 1 + 6\mathrm{i}$).

verify the conservation of energy in each case are listed in appendix D. In each case, the conservation of energy is confirmed to very good accuracy.

4.2.2. Comparison to other codes

Another important validation strategy is to simulate the same problem with different tools and compare the results. One comparison of that kind has been conducted in the context of scattering by flat particles on a substrate and published in a journal paper [160]. Smuthi results were compared to results from Yuri Eremin's discrete sources method with excellent agreement.

In addition, we have recently used the finite-element software COMSOL Multiphysics [105] to compute the electromagnetic fields of a more general scattering prob-

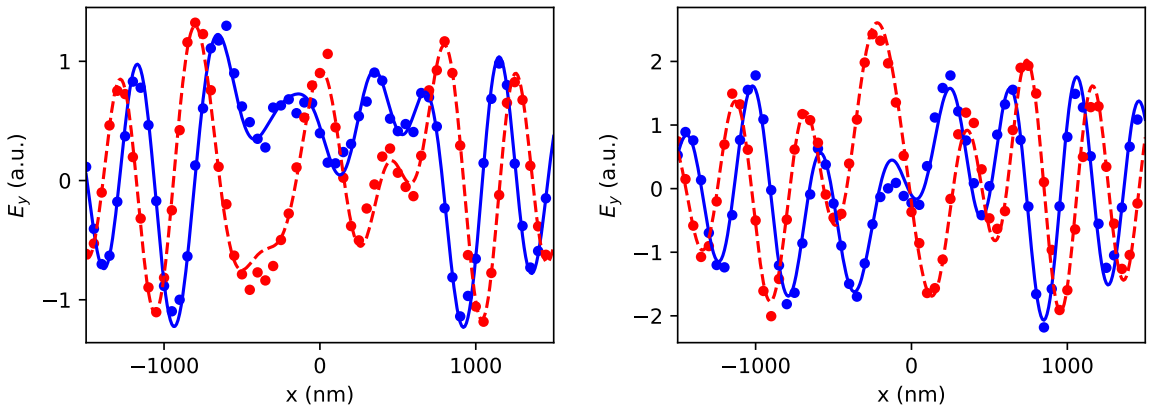

Figure 4.9. – Real part (blue solid line) and imaginary part (red dashed line) of E_y along a probing line computed with Smuthi. The corresponding COMSOL results are shown as filled circles. Left plot: dielectric scattering particles ($n = 3$), right plot: metallic scattering particles ($n = 1 + 6\mathrm{i}$).

lem. Afterwards, the same configuration was simulated using Smuthi. Figure 4.6 shows the scattering configuration which consists of a three-layer geometry incorporating a sphere, a cylinder, an oblate spheroid and a prolate spheroid. The initial excitation is given by a point dipole source located in the middle of the center layer. Table 4.1 lists some of the parameters describing the model.

Figures 4.7 and 4.8 display the y-component of the electric field in a plane parallel to the layer interfaces, $250\,\mathrm{nm}$ inside the top layer, for dielectric scattering particles ($n = 3$) and for metallic scattering particles ($n = 1 + 6\mathrm{i}$), respectively. The y component of the electric field is most interesting because it vanishes for the initial dipole field and is thus most sensitive to a correct treatment of (multiple) scattering. By looking at the figures it is evident that the qualitative features of the scattered field are identical.

Figure 4.9 shows E_y along a line, again $250\,\mathrm{nm}$ inside the top layer, and allows for a quantitative comparison. The agreement between the results is good, although not perfect. Note however that the deviation between Smuthi and COMSOL is within the range of fluctuations of the COMSOL results that occur when varying for example the distance between the so called *perfectly matched layer* and the scattering particles. I suspect that residual reflections from the perfectly matched layer cannot be avoided due to the fact that the layer interfaces intersect it. To conclude, it can be assumed that the agreement is constrained by the accuracy of the COMSOL results and not of the Smuthi results.

5. Simulation of disordered internal scattering layers in OLEDs

This chapter illustrates the application of the formalism presented in chapter 3 to disordered scattering layers in OLEDs. First, a realistic example OLED stack is introduced and optimized with respect to extraction efficiency by tuning the layer thicknesses and the location of the emission zones (section 5.1). In the following, this OLED stack serves as a starting point and as a reference for the simulation of OLEDs with scattering layers, which are described in section 5.2. Section 5.3 is dedicated to an error analysis in order to provide a sense of how reliable simulation results for the given problem can be expected to be. Finally, simulation results for OLEDs with internal disordered scattering layers are presented (section 5.4).

The leading question that I will pursue in this chapter, is the following:

> *How much can the extraction efficiency of OLED stacks that are already optimized with respect to the stack design (see section 5.1) be improved by adding disordered internal scattering layers?*

It is a well-known fact that large relative enhancement factors can be achieved by adding outcoupling structures to an optically "bad OLED", where a high fraction of the generated photons are in waveguide modes. On the contrary, if the OLED is already designed to emit most light into the escape cone of the substrate, the addition of a scattering layer leads to less dramatic enhancement factors. It is important to clarify from a theoretical perspective, what can realistically be expected in that case.

Tuning the optical cavity defined by the OLED thin film system, the extraction pattern can be significantly changed. A reasonable stack design is thus essential for an efficient OLED. The following section will thus discuss the optimization of the layer thicknesses and the emission zone location for two realistic OLED stacks. These optimized stacks will then later on serve as reference devices during the simulation of OLEDs with scattering layer.

5.1. Stack optimization

The example OLED stack is given by a white OLED with isotropically oriented transition dipoles. The thin-film system is modeled as a substrate, a transparent electrode (ITO), a thick layer that gathers the various organic functional layers such as charge

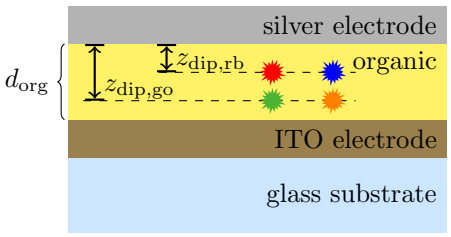

layer	thickness
silver	∞
organic	d_{org}
ITO	120 nm
substrate	incoherent
air	∞

Figure 5.1. – Example OLED stack with variable organic layer thickness and dipole position.

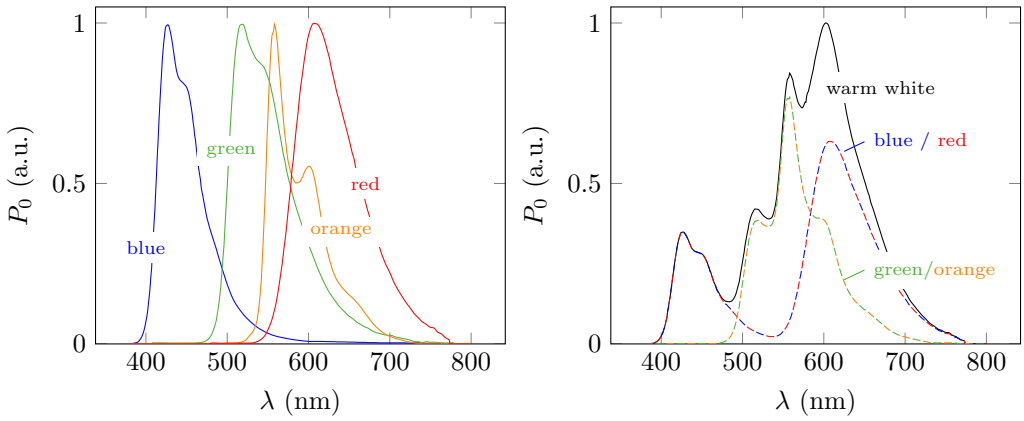

Figure 5.2. – Left: Typical spectra of OLED emitter materials for blue, green orange and red emission. Right: A superposition of the four spectra yields warm-white emission with good color rendering quality. The blue and red, as well as the green and orange portion of the emission are gathered to combined emitter systems, respectively [165].

injection, charge transport and emitter layers, and finally a metallic electrode (silver), see figure 5.1.

With regard to the concept of exciton recycling [165], we assume a system of four emitters (blue, green, orange and red, see figure 5.2) which are grouped in two combined layers of blue/red and green/orange. The relative weight of the respective spectra is tuned such that the overall internal spectrum $P_0(\lambda)$ represents a warm-white color.

With regard to the orientation of the emitter dipoles, it is common praxis to model the isotropic case as the incoherent addition of a horizontal and a vertical dipole, weighted with $2/3$ and $1/3$, respectively [166].

Three parameters are varied to optimize the structure: the total organic thickness d_{org}, and the locations $z_{dip,br}$ and $z_{dip,go}$ of the emitter zone for the blue/red and the green/orange system, respectively (compare the left of figure 5.1). This is a simplification as in a real optimization problem the production process and requirements

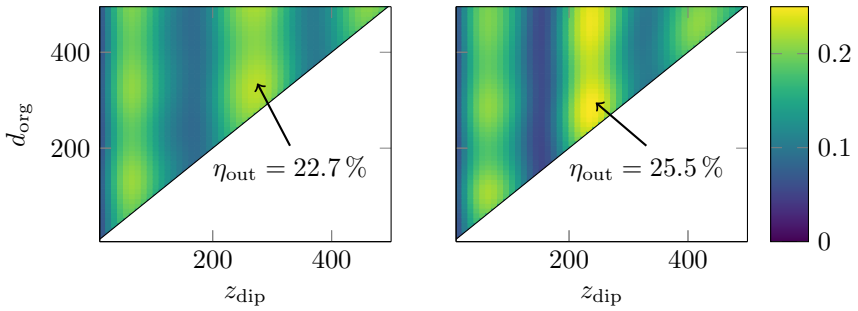

Figure 5.3. – Outcoupling (quantum) efficiency for the blue/red (left) and for the green/orange (right) emitter system, as a function of the total organics thickness and the z-position of the emitter systems.

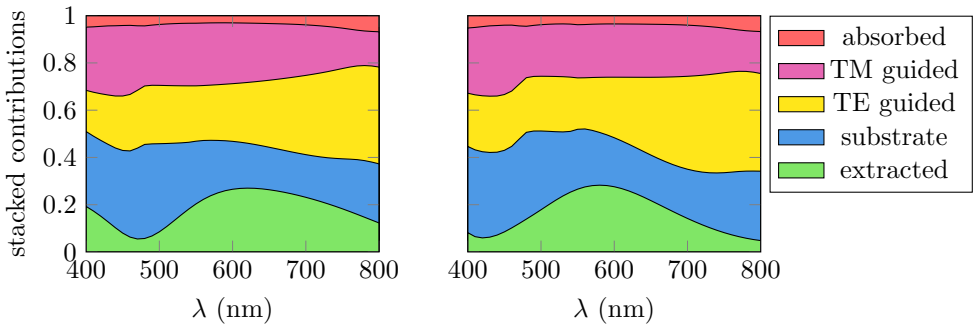

Figure 5.4. – External quantum efficiency and loss channels for the optimized white OLED as a function of the wavelength for the blue/red emitter system (left) and the green/orange emitter system (right), respectively.

connected to the electrical properties would impose restrictions to the variation of these parameters.

The optimization goal is a high outcoupling efficiency. This can be efficiently achieved by first calculating the extraction pattern (see section 1.3.1) as a function of the optimization parameters, $X_j^{\mathrm{air}}\left(d_{\mathrm{org}}, z_{\mathrm{dip,br}}, z_{\mathrm{dip,go}}; \lambda, \beta\right)$, and storing it in a table. Then, the optimal outcoupling efficiency can be evaluated as

$$\eta_{\mathrm{out}}^{\mathrm{max}} = \max_{d_{\mathrm{org}}, z_{\mathrm{dip,br}}, z_{\mathrm{dip,go}}} \sum_{j=1}^{2} \frac{\int \mathrm{d}\lambda\, P_0^{\gamma}\left(\lambda\right) \int \mathrm{d}\beta\, X_j^{\mathrm{air}}\left(d_{\mathrm{org}}, z_{\mathrm{dip,br}}, z_{\mathrm{dip,go}}; \lambda, \beta\right)}{\int \mathrm{d}\lambda\, P_0^{\gamma}\left(\lambda\right)}. \tag{5.1}$$

Figure 5.3 shows η_{out} as a function of d_{org} and z_{dip} for the blue/red and the green/orange emitter system, respectively. It turns out that the optimal outcoupling efficiency is achieved for a total organic thickness of $d_{\mathrm{org}} = 310\,\mathrm{nm}$ with an emission zone of the blue/red emitter system at $z_{\mathrm{dip,br}} = 265\,\mathrm{nm}$ and an emission zone of the green/orange emitter system at $z_{\mathrm{dip,go}} = 235\,\mathrm{nm}$. Then, the overall outcoupling efficiency is $\eta_{\mathrm{out}}^{\mathrm{max}} = 23.6\,\%$.

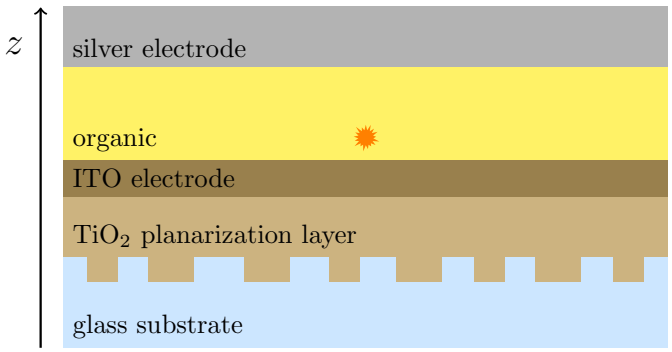

Figure 5.5. – Investigated OLED structure with scattering layer made of cylindrical holes etched into the glass substrate, then planarized with $\mathrm{TiO_2}$.

Figure 5.4 shows the outcoupling efficiency (green area) as well as the contributions to the various optical loss channels as a function of wavelength for the optimized OLED stack. It can be verified that the spectral outcoupling efficiency for the green/orange system roughly coincides with the center of mass of the emitter spectrum, whereas the maximum of the spectral outoupling efficiency for the blue/red system is less pronounced (due to the double-peaked emitter spectrum).

5.2. The scattering layer

In previous papers, we have treated scattering layers comprising high refractive index nano particles embedded in a host polymer layer [78, 126, 127][1], where the particles were modeled as spheres. Here, I want to address the simulation of flat scattering layers comprising a laterally disordered array of nano holes planarized by a material of different refractive index.

Such layers can be fabricated using bottom-up approaches like polymer blend technology [49–57]: Two polymer materials, typically polystyrene (PS) and poly(methyl methacrylate) (PMMA), are dissolved and mixed together in a mutual solvent. A small volume of the mixture is then processed on a substrate. During evaporation of the solvent, the polymers separate and form islands of the one material surrounded by domains of the other material[2]. The morphology of the structure can be tailored by tuning the fabrication process parameters (including material concentrations and molecular weights, annealing temperature, humidity) [50, 52, 56, 57]. After selectively removing one of the materials, either nano pillars or a film with nano holes can be obtained. These structures can either be directly used as scattering layers, or be transferred into a different material using lift-off, etching or stamping processes [50, 56].

[1] These studies were conducted using a prototype Matlab code preceding Smuthi
[2] Other topologies like 2D network structures are possible, too.

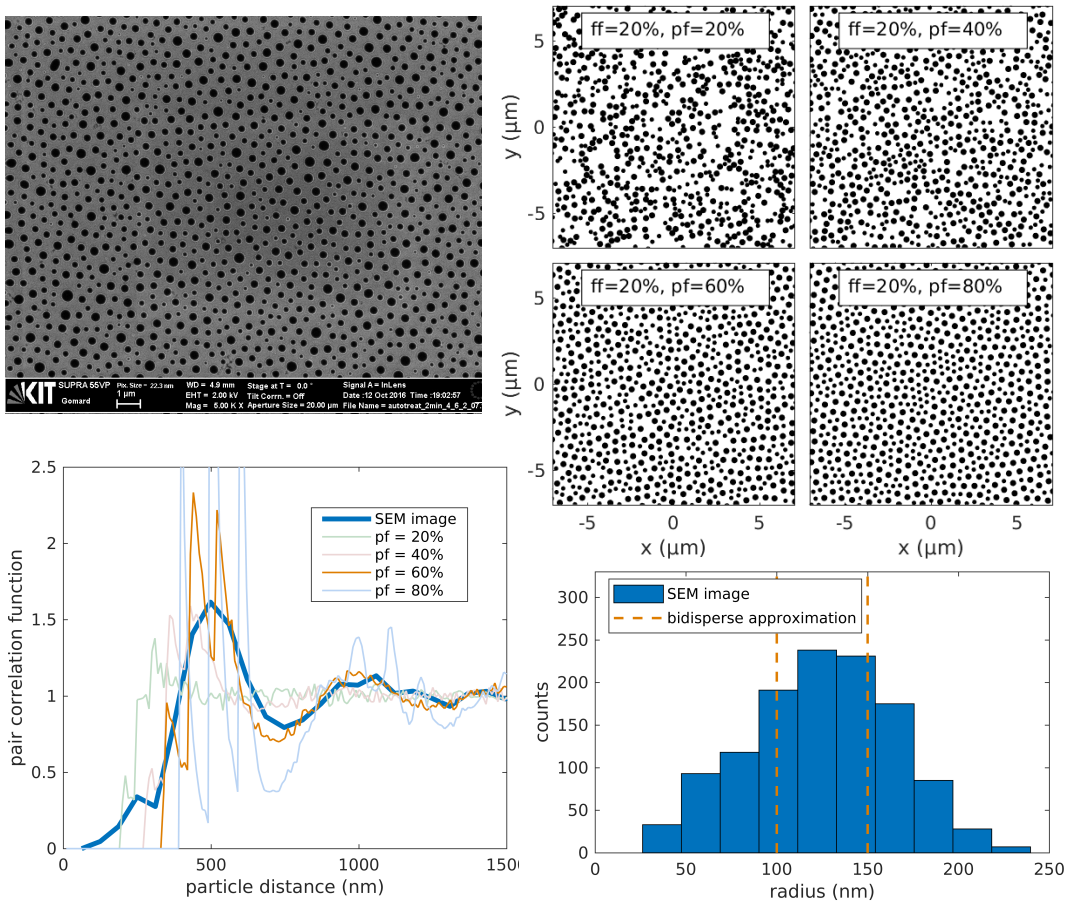

Figure 5.6. – Top left: SEM image of a nano pillar structure fabricated from polymer blend. Top right: Generated bidisperse disc packings with constant filling fraction (ff) of $20\,\%$. The spatial correlation is tuned by varying the packing fraction (pf) between $20\,\%$ and $80\,\%$. Bottom left: Pair correlation function. Bottom right: Pillar radius distribution.

For this study, I assume the following OLED fabrication process that was identified by Christian Stamm [167] as a robust and well feasible route to planarized disordered scattering layers for outcoupling from OLEDs:

1. A PMMA layer with nano holes is fabricated on a glass substrate using polymer blend phase separation.
2. Using dry etching, the nano holes are transferred into a glass substrate, and the remaining PMMA is removed.
3. The glass substrate with nano holes is covered with a titania nanoparticle layer[3]

[3]The optical constants of the titania layer are taken from measurements performed by Jurana Hetterich in collaboration with Christian Stamm. Due to the nano porosity of the titania material, the refractive index is smaller than that of bulk titania [167]. For a wavelength of $550\,\mathrm{nm}$, the refractive

filling up and planarizing the holes.

4. On top, the optimized OLED stacks discussed in section 5.1 are processed.

To model the scattering particles, I assume further that

- the nano holes have a perfectly cylindrical shape and are entirely filled with titania
- the depth of the nano holes can be deliberately tuned through the dry etching dose
- the distribution of hole radii and their lateral spatial distribution follow the same statistics as the structure depicted in the scanning electron microscopy (SEM) image shown in the top left of figure 5.6.

In order to allow simulations with arbitrary particle numbers and scattering layer lateral dimensions, I approximate the distribution of circles displayed in the top left of figure 5.6 with artificially generated disc packings, which were prepared by Lorenzo Pattelli using molecular-dynamics codes provided by Monica Skoge et al. [168] and based on the Lubachevsky-Stillinger algorithm. All packings have a *filling fraction* of $20\,\%$, which is similar to that of the original particle distribution shown in the top left of figure 5.6. Regarding the disc radii, the measured distribution is approximated by a bidisperse distribution of $100\,\mathrm{nm}$ and $150\,\mathrm{nm}$ to equal parts, see the bottom right of figure 5.6. Finally, the pair correlation function of the generated packings are adjusted following the same procedure as described in [169]: during the generation of the point pattern, the excluded volume is tuned by setting larger than the actual disc radii, leading to a *packing fraction* between $20\,\%$ and $80\,\%$. After the algorithm has terminated, the disc radii are "deflated" to their actual values yielding the desired filling fraction but with a pair correlation function corresponding to a higher packing fraction. The top right of figure 5.6 shows the artificially generated bidisperse packings, whereas the bottom left of figure 5.6 shows the pair correlation function estimated for the SEM image using Ilya Valmianski's Matlab code [170] in comparison to that estimated for the artificial samples. For a packing fraction of $60\,\%$, the pair correlation function fairly approximates the one estimated for the SEM image, although it shows some spiky amorphous features lacking in the original curve.

5.3. Accuracy analysis

The idea is to use the simulation approach described in this thesis in order to estimate the outcoupling efficiency from the OLEDs with scattering layers. However, before we can proceed to the simulation results, it is important to assess the reliability of the approach.

index is around ~ 2.04.

Three classes of errors need to be considered: The bare numerical errors of the scattering simulations, the error related to the sample averaging of the random distributions and finally the error implied by considering only a finite number of scattering particles. Each of the following three sections deals with one of these categories.

5.3.1. Numerical errors

Simulation results are not exact, and their accuracy depends on a number of numerical parameters that trade precision with computation time. Table 5.1 lists a selection of these parameters.

symbol	parameter	default	reference
$l_{\max}$	truncation multipole degree	variable	10
$m_{\max}$	truncation multipole order	variable	10
$n_{\text{eff,max}}$	truncation effective refractive index	3	3
$n_{\text{eff,imag}}$	imaginary contour deflection	0.01	0.01
Δn_{eff}	Sommerfeld integral sampling	2×10^{-3}	1×10^{-3}
$\Delta\alpha$	azimuthal angle resolution	$1°$	$0.25°$
$\Delta\beta$	polar angle resolution	$1°$	$0.25°$
$\Delta\rho$	lookup table resolution	$5\,\text{nm}$	$2\,\text{nm}$
tol	iterative solver tolerance	5×10^{-4}	1×10^{-5}

Table 5.1. – Parameters critical for numerical accuracy

A default set of parameters is selected (the third column of table 5.1). In order to confirm that these settings are appropriate, the influence of each parameter on the accuracy for a toy model including $N_{\text{S}} = 1000$ particles is evaluated. Each parameter is varied whereas all other parameters are fixed to their default values (exception: for $l_{\max} < 3$, $m_{\max}$ needs to be reduced because always $m_{\max} \leq l_{\max}$). The relative accuracy of the substrate coupling efficiency[4] is then estimated by comparison to an accurate reference simulation with very conservative parameter settings, see the fourth column of table 5.1.

The most important parameters are the multipole expansion truncation parameters $l_{\max}$ and $m_{\max}$. They strongly influence both the accuracy and the numerical effort as they determine the number of unknowns per particle and thereby the dimension of the linear system (3.70). In the shown example, it turns out that for $l_{\max} \geq 6$ and $m_{\max} \geq 3$ the numerical errors drop below $0.5\,\%$ such that these values seem justified for an acceptable numerical accuracy in the shown example. As a consequence, this choice limits the accuracy to $\sim 10^{-3}$ such that the relative error from all other parameter sweeps cannot be lower than that value. The shown curves merely illustrate in

[4] the electromagnetic power radiated into the substrate, see section 2.3.1.2, divided by the total dissipated dipole power, see section 1.3.2.2

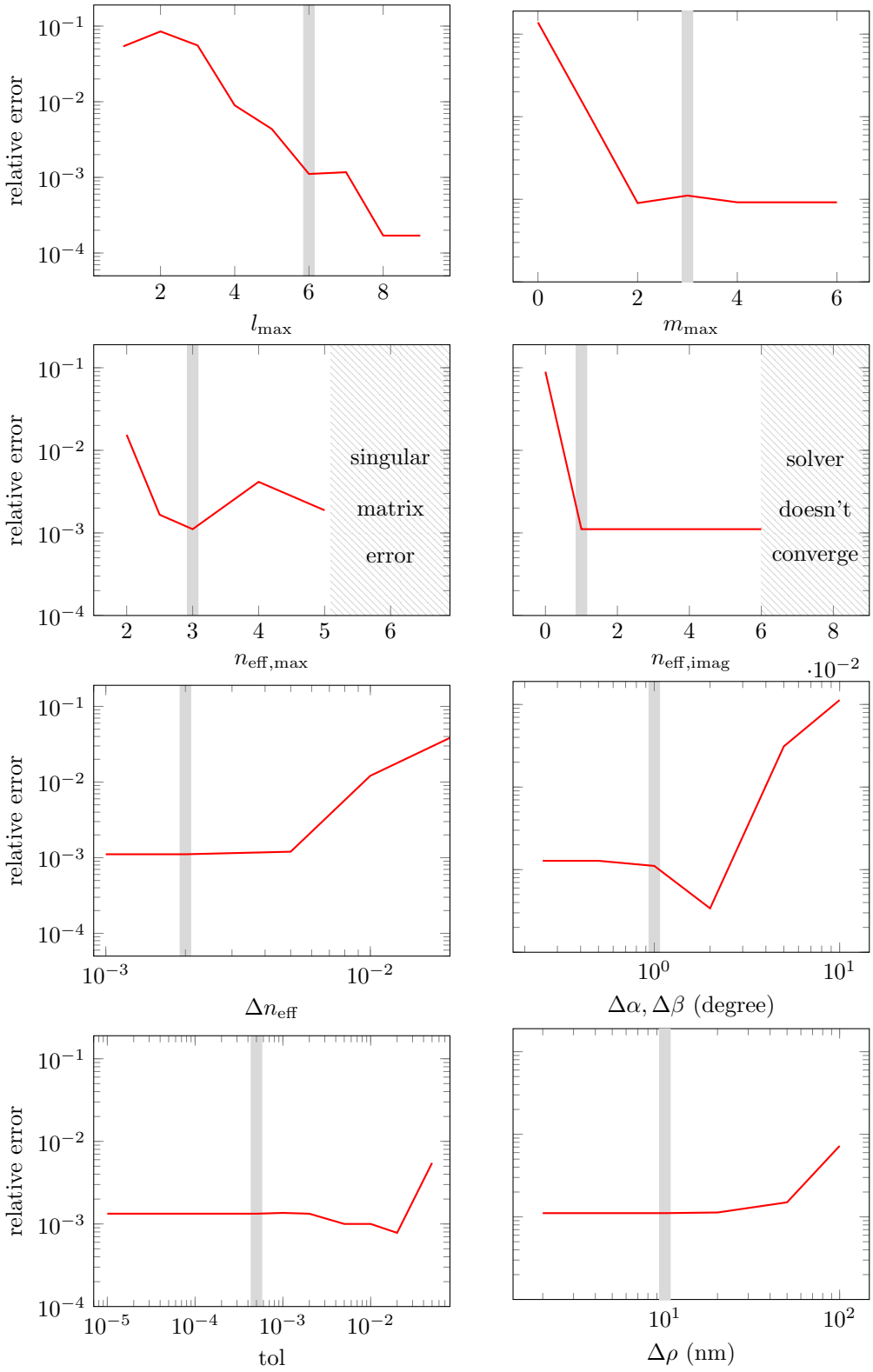

Figure 5.7. – Influence of numerical parameters on the accuracy of the substrate coupling efficiency. The vertical grey line marks the default value of the parameter.

what regime some parameter starts to limit the accuracy to values worse than 10^{-3}, i.e., when a a parameter becomes prohibiting. This way, it can be verified that the selected parameters allow an accuracy better than $0.5\,\%$.

Special care has to be taken when addressing the complex contour truncation $n_{\mathrm{eff,max}}$ and its imaginary deflection $n_{\mathrm{eff,imag}}$, as they don't follow a simple "the-larger-the-more-accurate" logic. For the imaginary deflection, the accuracy for low values is limited because the integrand then passes nearby waveguide mode resonances, see section 3.10.2. On the other hand, when using too large imaginary deflection, the complex Bessel function grows to large values which again limits the numerical accuracy of the integral. For the contour truncation, the issue with too large values is due to a relative convergence phenomenon that occurs for flat particles near a planar interface [159,160].

The choice of a suitable $l_{\max}$ and $m_{\max}$ depends on the size of the nano holes as well as the wavelength. These parameters are thus fixed for each set of simulations individually, whereas the other parameters are globally set to the "default" values as shown in table 5.1.

5.3.2. Sample averaging

One wave optics simulation can cover only a single random realization of an infinite set of possible simulation geometries with different dipole orientation in space, as well as different scattering particle configurations. Therefore, one needs to average over these distributions in order to obtain an estimate for the statistical expectation value of the outcoupling efficiency rather than a random simulation result. In order to do so, I repeat the wave optics simulations several times, and each time draw the dipole orientation from a uniform random distribution of points on the unit sphere, and the dipole position from a uniform random distribution of locations relative to a fixed particle distribution[5]. The resulting substrate coupling efficiency is then averaged incoherently over the random simulations,

$$\overline{\eta}_{\mathrm{sub}} = \frac{1}{N_{\mathrm{sim}}} \sum_{\mathrm{sim}} \eta_{\mathrm{sub,sim}} \qquad\qquad \Delta\eta_{\mathrm{sub}} = \frac{\sigma}{\sqrt{N_{\mathrm{sim}}}}, \tag{5.2}$$

where N_{sim} is the number of simulations, $\sum_{\mathrm{sim}}$ is a sum over all simulations, $\eta_{\mathrm{sub,sim}}$ is the substrate coupling efficiency for one simulation, $\Delta\eta_{\mathrm{sub}}$ is the standard error of the mean substrate coupling efficiency and σ is the standard deviation of $\eta_{\mathrm{sub,sim}}$.

In order to reduce the number of necessary simulations, arrays of point dipole sources can be considered instead of single point dipoles. The advantage is that with many

[5] I assume that this is sufficient to mimic a true averaging over particle distributions, as the randomness of the particle constellation has the strongest influence in the local environment of the dipole source.

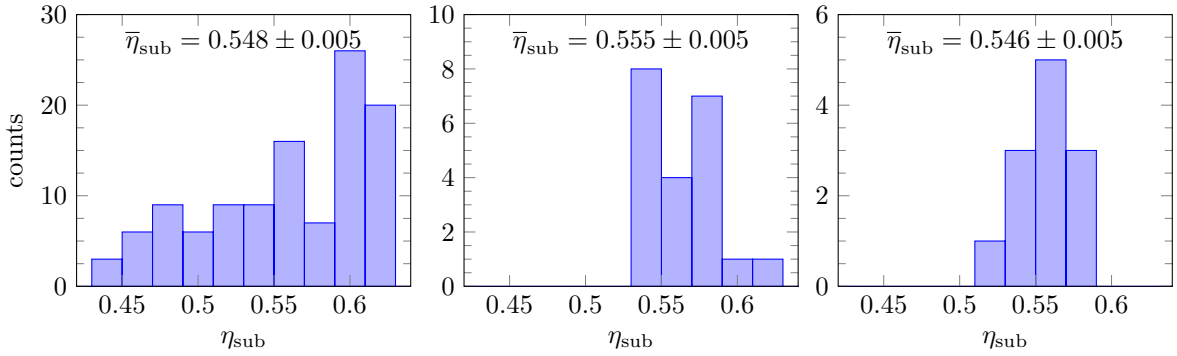

Figure 5.8. – Averaging the substrate coupling efficiency over many random realizations for an isotropic dipole and a scattering domain spanning $20\,\mu\mathrm{m}$ in diameter. Left: single dipole simulations. Middle: simulations with groups of 9 dipoles. Right: Groups of 16 dipoles.

dipoles in a single simulation, the most significant source of fluctuations can already be eliminated: the local configuration of a point dipole with the scattering particle pattern. For example, if the lateral position of a particle coincides with that of the dipole, a different (probably smaller) substrate coupling efficiency must be expected compared to a dipole that is not "covered" with any particle. To approximate an incoherent superposition of dipole sources, the relative phase of each dipole amplitude is also drawn from a random distribution, such that any interference effects between the sources are averaged over [47].

dipoles per simulation	standard deviation σ	N_{sim} to achieve $\Delta\eta_{\mathrm{sub}} = 0.005$	dipoles total
1	0.053	111	111
9	0.023	21	189
16	0.017	12	192

Table 5.2. – With more dipoles per simulation, fewer simulations are needed to achieve the same accuracy of $\overline{\eta}_{\mathrm{sub}}$.

Figure 5.8 shows the distribution of simulation results regarding the substrate coupling efficiency for a scattering domain with a radius of 10 micron. In the left panel, each simulation contained a single dipole source, whereas the middle and right panel correspond to arrays of 9 and 16 dipoles, respectively. It can be verified that the resulting mean values are consistent within the standard error, supporting the assumption that a random initial phase can eliminate any systematic interference effect. In addition, one can see that due to the reduced fluctuation of the results, the same standard error $\Delta\eta_{\mathrm{sub}} = 0.005$ of the mean efficiency can be accomplished with fewer simulations if more dipoles are considered per simulation.

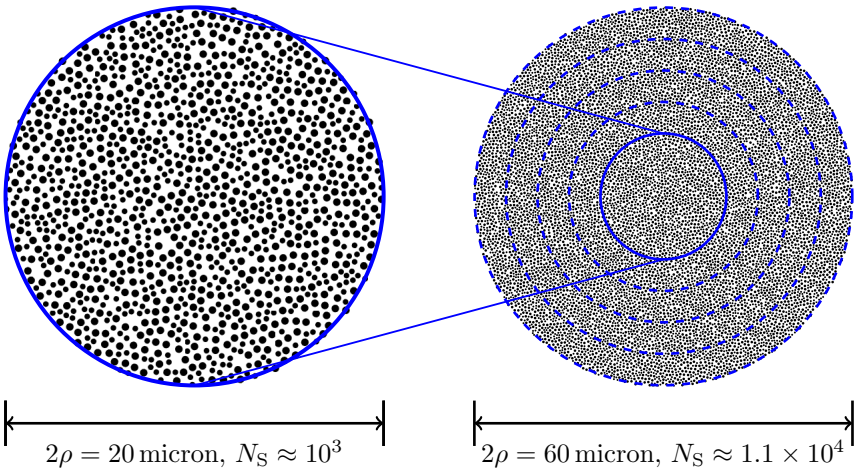

Figure 5.9. – Sweeping the scattering domain radius from $\rho = 10\,\text{micron}$ to $\rho = 30\,\text{micron}$.

5.3.3. Particle number truncation

When a finite number of scattering particles is considered, the scattering sample is restricted to a certain domain, for example a circular area with radius ρ, see figure 5.9. The extraction of power from thin-film guided modes is thus systematically underestimated, as the outcoupling contribution from scattering particles beyond the ensemble domain is not considered in the simulation.

In order to overcome this limitation, a phenomenological model [78,171] can be used to extrapolate the substrate coupling efficiency:

$$\eta_\text{sub}(\rho) = A - B\mathrm{e}^{-C\rho}, \tag{5.3}$$

where C corresponds to an *effective waveguide mode extinction length*. By adapting the model parameters A, B, C such that the model fits the simulation data, the substrate coupling efficiency can be extrapolated to

$$\lim_{\rho\to\infty} \eta_\text{sub} = A, \tag{5.4}$$

compare figure 5.10. Such a sweep over the domain radius can be achieved using only a single wave optics simulation by applying the following trick:

1. Run a full simulation for a large number of particles N_S.
2. Compute the far field power according to (3.72).
3. Approximate the far field power for a consecutive series of smaller subsets Σ_ρ of particles by truncating the sum in (3.73) at the respective particle numbers:

$$\sum_\text{S} \to \sum_{\text{S}\in\Sigma_\rho} \qquad \text{with} \quad \Sigma_\rho = \left\{S | \mathbf{r}_{\parallel,S} \leq \rho\right\} \tag{5.5}$$

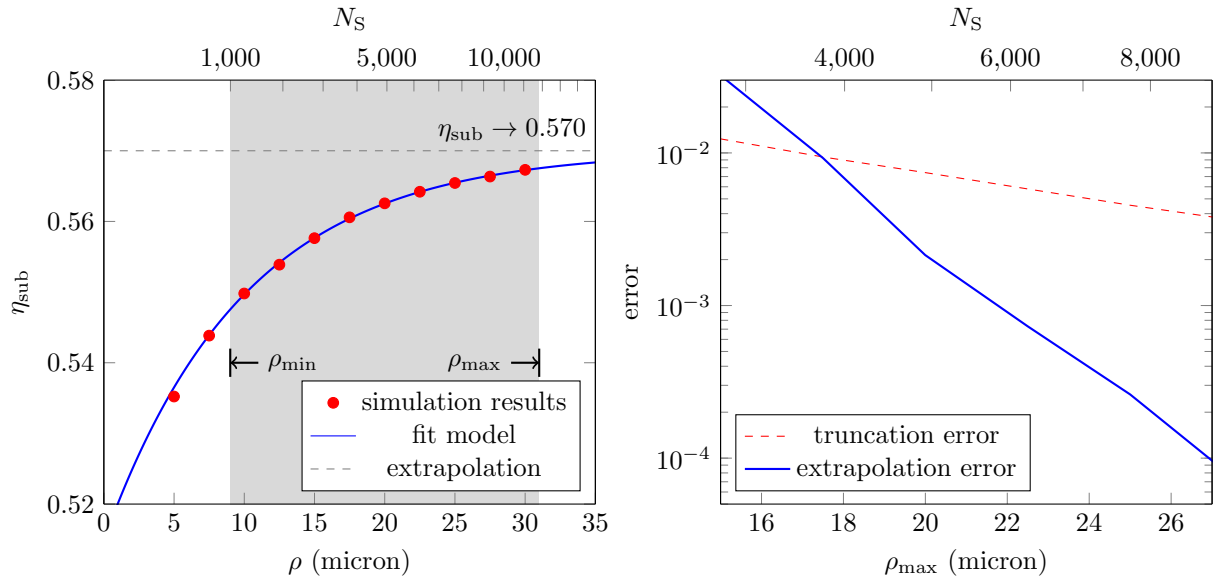

Figure 5.10. – Left: Substrate coupling efficiency as a function of the scattering domain radius for an array of 25 randomly oriented dipoles. The red symbols are simulation results, the blue line is the fit model (5.3). The dashed gray line indicates the extrapolated value for $\rho \to \infty$. The gray rectangle marks the domain $[\rho_{min}, \rho_{max}]$ of domain radii that were used to calibrate the fit model. Right: An estimate of the absolute error introduced by using a finite scattering particle domain truncated at ρ_{max} (red dashed line) or by using the extrapolation calibrated with simulation data for a maximal particle domain ρ_{max} (blue line).

4. Fit the model parameters

As the fit model is not valid for small ρ [78,171], some uncertainty remains regarding the minimal domain radius ρ_{min} above which simulations are used for the calibration of the fit model, and the extrapolated results thus remain somehow vague. Nevertheless, I assume that this extrapolation scheme in general enhances the accuracy of the estimated substrate coupling efficiency compared to simply using the values taken from a finite particle number simulation.

5.4. Results

After the quantitative reliability of the suggested simulation method has been assessed in the previous section, I will now present the results of the example study, which aims at an estimation of the outcoupling efficiency enhancement when inserting a disordered scattering layer into an already optimized white OLED stack. In order to cover the whole emission spectrum, the simulation wavelength is varied from $450\,\mathrm{nm}$ to $750\,\mathrm{nm}$ in steps of $50\,\mathrm{nm}$. In addition, the depth of the nano holes is varied between $h = 220\,\mathrm{nm}$, $h = 260\,\mathrm{nm}$, $300\,\mathrm{nm}$ and $h = 340\,\mathrm{nm}$. The lateral radius of the

scattering sample was limited to $\rho = 20$ micron which corresponds to circa $N_S \sim 5000$ particles.

5.4.1. Radiation into the substrate

For each pair of wavelengths and nano hole dephts, the radiation into the substrate is computed with Smuthi by averaging over five simulations each of which contains a random realization of the scattering configuration and a random realization of 36 isotropically oriented dipole emitters. This has to be done twice – once for the optimal emission zone of the blue/red emitter system and once for the optimal emission zone of the green/orange emitter system, see section 5.1, which leads to a total number of $7 \times 4 \times 5 \times 2 = 280$ simulations.

Figure 5.11 shows the simulated radiation pattern into the substrate for a nano hole depth of $h = 260\,\mathrm{nm}$ as a function of the emission angle. Recall that the radiation pattern corresponds to the power emitted into a polar angle interval and is thus proportional to the emitted intensity times $\sin\beta$, which explains why the curves go to zero for $\beta \to 0$. The scattering layer enhances the efficiency of the initial emission into the substrate significantly. The integral over the radiation pattern with respect to the emission angle yields the substrate coupling efficiency which is depicted in figure 5.12. Due to the coarse sampling of wavelengths in steps of $50\,\mathrm{nm}$, the simulation results need to be interpolated (extrapolated) between (beyond) the simulated wavelengths.

5.4.2. Diffuse and specular reflection

In order to evaluate the polar BRDF $R^{\mathrm{oled}}_{j,j'}(\lambda, \beta, \beta')$ as defined in section 1.3.3, a series of simulations with Gaussian beams as the initial field is performed. The incident propagation angle of the beam hitting the OLED structure from the substrate side is varied from 0 degree to 80 degree in steps of 10 degree. Covering both TE and TM polarization, this leads to a number of 18 simulations per wavelength and scattering layer geometry. The beam waist was set to 10 micron covering many scattering centers, such that the local configuration of the scattering centers is already effectively averaged over in only one simulation shot. Thus, in total $18 \times 7 \times 4 = 504$ Smuthi simulations are done. In addition, I assume that waveguide mode extraction is not critical in the BRDF simulations, because it is only a second order effect: for power to be extracted from a waveguide mode, two scattering events are necessary – one coupling the power into the mode and the other one to extract it[6]. As a consequence, an extrapolation of the reflected power to an infinite scattering domain radius is not necessary. In order to compensate for the intrinsic divergence of the initial beam, a small

[6]This is different from simulations with dipole sources where a substantial part of the initial power is in waveguide modes.

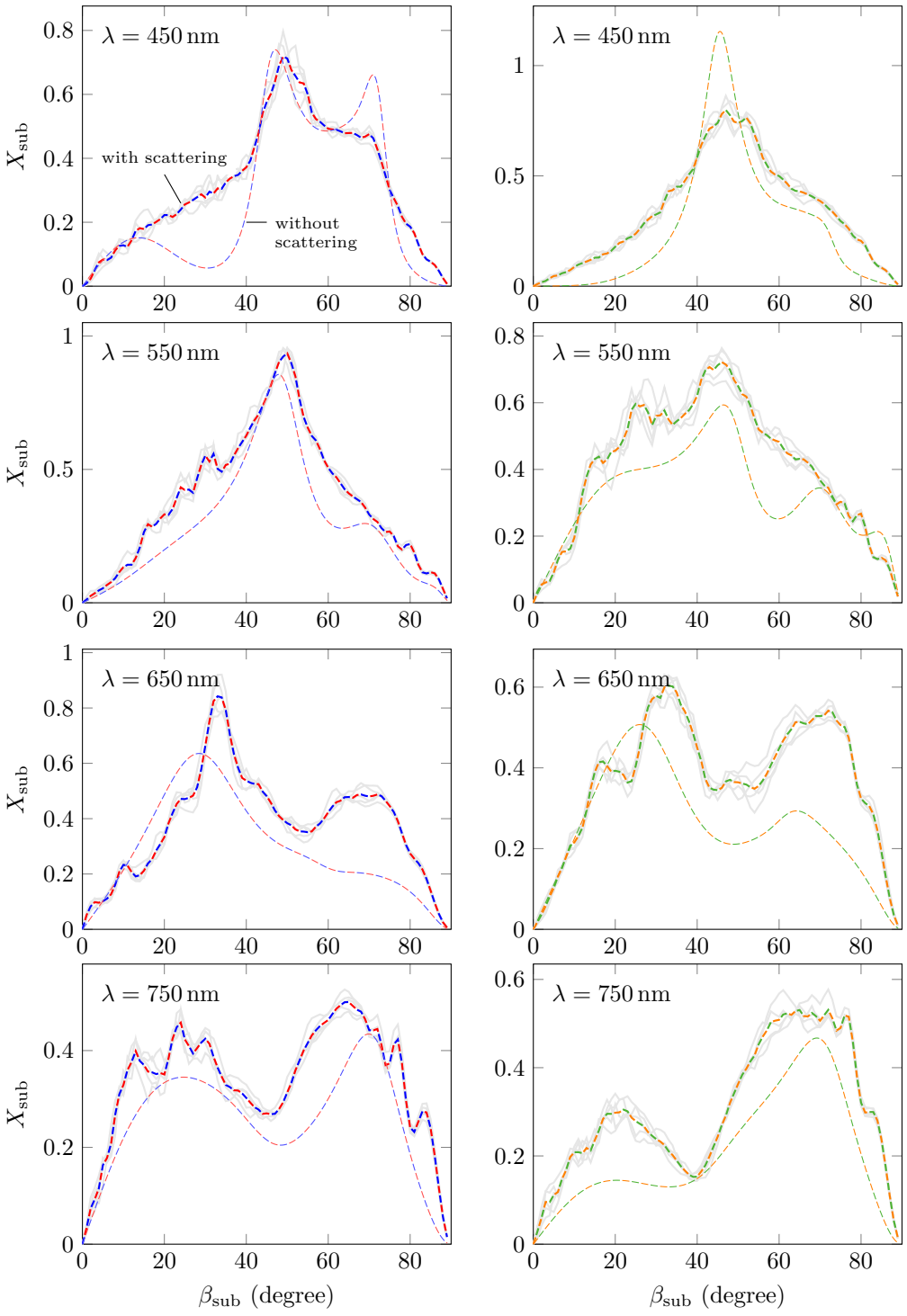

Figure 5.11. – Radiation patterns into the substrate for the white OLED stack with a disordered scattering layer with a nano hole depth of $h = 260\,\mathrm{nm}$ at a packing fraction of $\mathrm{pf} = 60\,\%$. The light grey lines refer to individual simulations, whereas the thick dashed lines are the average over five simulations. The thin dashed lines refer to the bare OLED stack without scattering particles (but with the planarization layer). The left column corresponds to dipoles located at the optimal red/blue emission zone at $z_{\mathrm{dip}} = 265\,\mathrm{nm}$, whereas the right column corresponds to dipoles located at the optimal green/orange emission zone at $z_{\mathrm{dip}} = 235\,\mathrm{nm}$, see section 5.1.

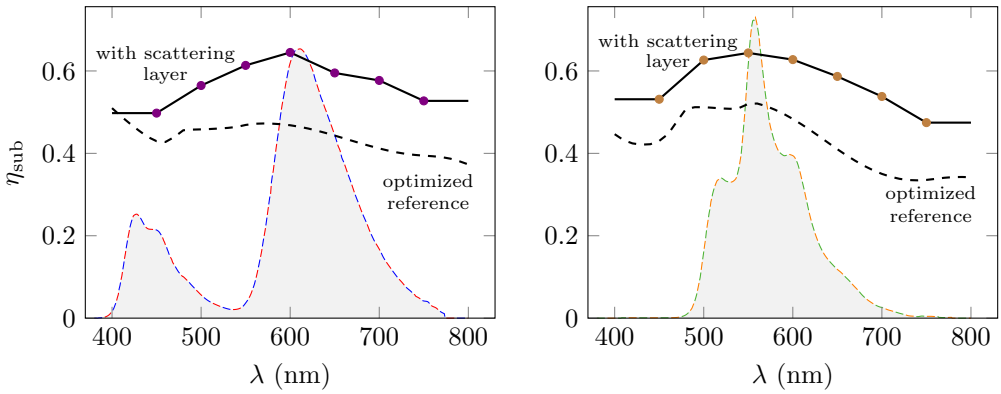

Figure 5.12. – Simulated substrate coupling efficiency (symbols) for isotropic emission from the optimal red/blue (left) and green/orange (right) emission zone for $h = 260\,\mathrm{nm}$ and $\mathrm{pf} = 60\,\%$. Dashed black lines: OLED stack without scattering layer. Shaded areas: internal photon number spectrum P_0^{γ}.

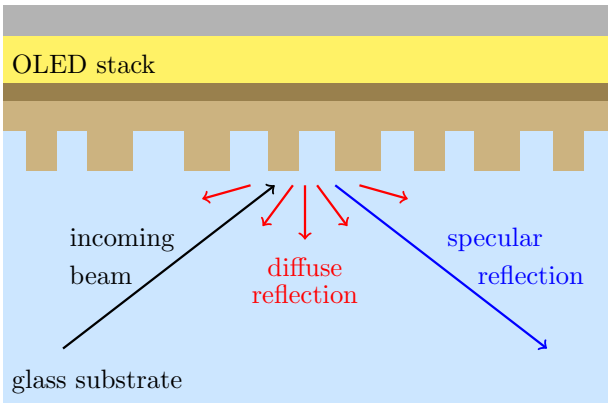

Figure 5.13. – Specular and diffuse reflection from the OLED stack with scattering layer.

but finite solid angle around the specular direction is defined, and light reflected into this solid angle is attributed to specular reflection [78].

Figure 5.14 shows the resulting diffuse and specular reflectivity for the white reference OLED stack with a scattering layer at $\mathrm{pf} = 60\,\%$ packing fraction and a nano hole depth of $h = 260\,\mathrm{nm}$. With growing wavelength the diffuse reflectivity is suppressed because the size of the nano holes becomes smaller compared to the wavelength, which leads to a reduced scattering strength. Further, the total reflectivity is in general smaller than without scattering centers (light gray curves), due to incoupling of light into waveguide modes, leading to an enhanced absorption. Nevertheless, the net effect of scattering for the extraction of light from the substrate is always positive, because it is the diffuse rather than the total reflectivity which enhances the outcoupling.

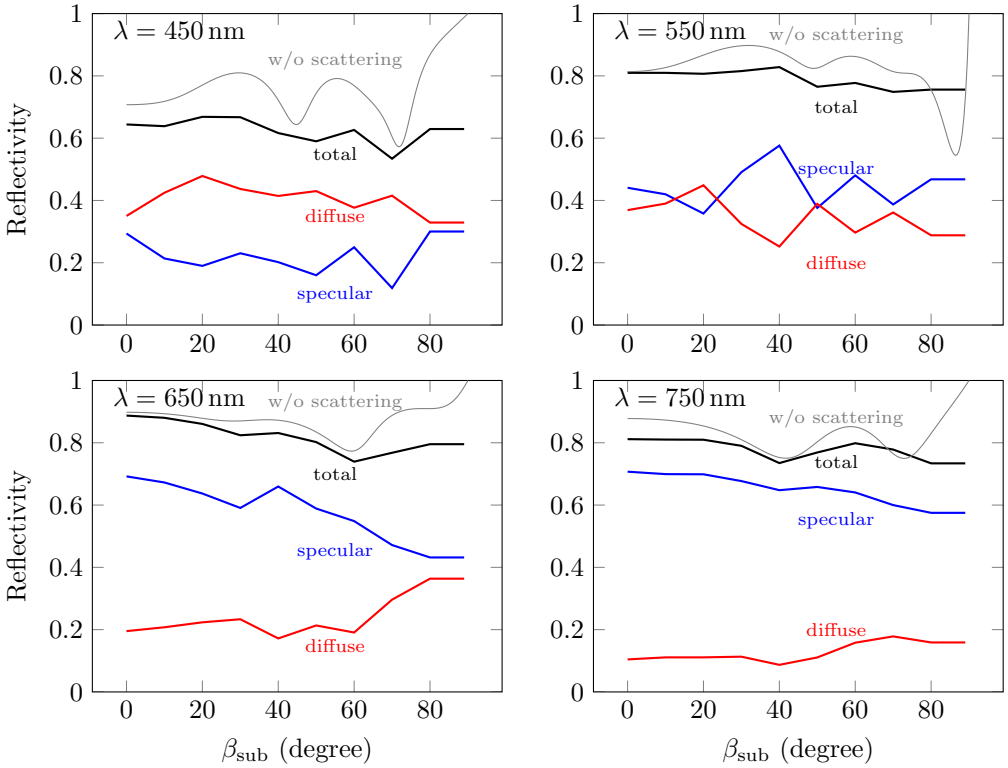

Figure 5.14. – Specular and diffuse unpolarized reflectivity for the white OLED stack with a disordered scattering layer with a nano hole depth of $260\,\mathrm{nm}$ at a packing fraction of $\mathrm{pf} = 60\,\%$. The light grey lines refers to the reflection from the bare OLED stack without scattering centers but with the planarization layer.

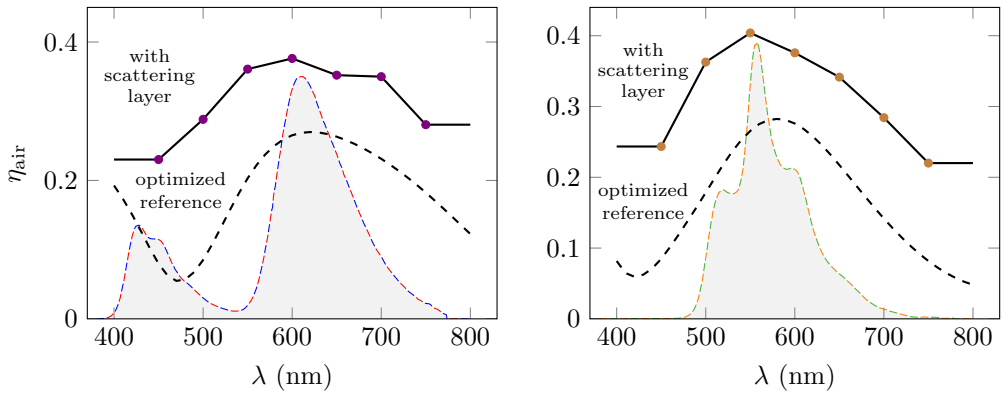

Figure 5.15. – Simulated air coupling efficiency (symbols) for isotropic emission from the optimal red/blue (left) and green/orange (right) emission zone for $h = 260\,\mathrm{nm}$ and $\mathrm{pf} = 60\,\%$. Dashed black lines: OLED stack without scattering layer. Shaded areas: internal photon number spectrum P_0^γ.

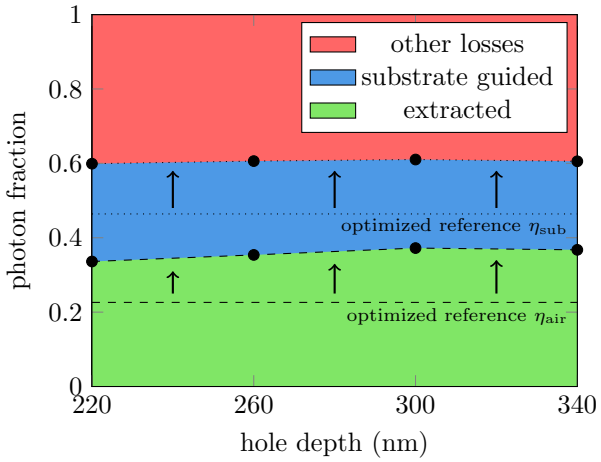

Figure 5.16. – Simulated extraction efficiency and substrate coupling efficiency as a function of nano hole depth. Reference values from the optimized OLED without scattering layer are shown for comparison.

5.4.3. Radiation into the ambient

The initial emission into the substrate, together with the polar BRDF allow the computation of the emission into air by first computing the radiation pattern in the substrate using (1.9) and (1.20), and then using (1.6) to evaluate the radiation pattern in air. The integral over the radiation pattern, weighted with the intrinsic photon number spectrum then yields the final outcoupling (quantum) efficiency for the white OLED with scattering layer. The extraction efficiency as a function of emission wavelength is shown in figure 5.15 for a nano hole depth of $h = 260\,\text{nm}$. A significant enhancement of the extraction efficiency is visible for all wavelengths. Again, the photon number spectrum of internal light generation is illustrated with a shaded area.

Finally, figure 5.16 depicts the spectrally integrated extraction efficiency for nano hole depths of $220\,\text{nm}$, $260\,\text{nm}$, $300\,\text{nm}$ and $340\,\text{nm}$, respectively. It turns out that with the proposed scattering layer, the extraction efficiency can be enhanced by a factor of ~ 1.6 from $\sim 23\,\%$ to $\sim 36\,\%$. It is noteworthy that both internal and external outcoupling contribute to the enhanced efficiency, as can be seen in table 5.3.

The here presented study is meant to be a realistic estimate of *what can be expected* from adding a scattering layer to an already optimized white OLED stack with isotropic dipole orientation. Somewhat higher enhancement factors are probably possible by optimizing the scattering layer and OLED stack parameters together in an extensive experimental or simulative parameter study, instead of first optimizing the OLED stack and then adding a scattering layer.

hole depth	OLED → substrate	substrate → air	OLED → air
reference	46.8 %	50.4 %	23.6 %
220 nm	59.9 %	56.1 %	33.6 %
260 nm	60.6 %	58.4 %	35.4 %
300 nm	61.0 %	61.0 %	37.2 %
340 nm	60.6 %	60.7 %	36.8 %

Table 5.3. – Contribution of the internal and external extraction to the total outcoupling efficiency.

6. Discussion

This PhD project was like a journey. It took me more than five years, and during that time some questions were answered (section 6.1), but at least the same number of questions remained unanswered (section 6.2).

6.1. Conclusions

New insight could be obtained with regard to the following topics:

Modeling of planar OLEDs: For OLEDs without a scattering layer, a semi quantum mechanical modeling approach was compared to the state of the art classical modeling approach. Based on the classical approach, an exemplary white OLED configuration was optimized with regard to layer thickness and emission zones.

Outcoupling efficiency for OLEDs with disordered internal scattering layers: Through an extensive numerical study it was demonstrated that an optimized white OLED with isotropically oriented dipole emitters can be improved by a factor of ~ 1.6 in terms of outcoupling efficiency when adding a flat internal disordered scattering layer.

T-matrix method for particles inside planarly layered media: With the formalism presented in this thesis, the T-matrix method for light scattering by wavelength scale particles has been extended to multiple particles inside planarly layered media. This was achieved by complementing the spherical-wave based approach that is inherent to the T-matrix method with a plane-wave based treatment of the propagation through the stratified background geometry. The transformation of the one field representation into the other builds a cornerstone of the new method.

Flat particles near planar interfaces: Due to the divergence of the spherical wave expansion of the scattered field inside the circumscribing sphere of a particle, it was commonly believed that the T-matrix method cannot be rigorously applied to flat particles near interfaces. By means of an analysis of the underlying convergence properties we have demonstrated that with a careful truncation of the Sommerfeld integrals, valid simulation results can be achieved. This technique has been elaborated in our recent paper [160] and was here applied to the case of disordered ensembles of nano pillars in a thin-film system.

Smuthi: A simulation code was introduced and released for free use. It has been demonstrated to obtain valid simulation results both by checking the conservation of energy to a high precision, as well as by comparison of results to established simulation software. The simulation of OLEDs with scattering layers are only one example of the wide range of possible applications, which also include scattering layers in solar cells, total internal reflection scattering microscopy, surface enhanced Raman spectroscopy, meta-surfaces, photonic crystal slabs and many other systems involving particles near interfaces.

Computational efficiency: The presented formalism was optimized for an efficient treatment of many particles. A significant speedup was achieved by means of a lookup table approach for the evaluation of the Sommerfeld integrals as well as by shifting the arithmetic workload from the central processing unit (CPU) to the graphics processing unit (GPU).

6.2. Outlook

For a continuation of this work, I see the following opportunities:

Periodic structures: Can the proposed formalism and the software be extended to cover periodic systems? The state of the art in the simulation of disordered scattering layers in solar cells and OLEDs is to model the system as a laterally periodic geometry with a large disordered unit cell. The underlying assumption is that if the dimension of the unit cell is chosen large enough, the scattering properties approach that of an infinite disordered scattering layer. While this assumption is for sure reasonable in the case of solar cells, where the initial field is periodic (up to a phase for oblique incidence), one issue with periodic layers for OLEDs is that the source is not periodic. One approach to resolve this issue could be a Floquet decomposition of the dipole field [111]. It would be interesting to study how these concepts can be realized together with the T-matrix method.

Internal plus external scattering: One advantage of disordered internal scattering layers is that they address both, the internal[1] and the external[2] light extraction. An open question is: can the addition of an external structure like a micro lens array at the substrate-air interface improve the extraction efficiency compared to a configuration with only an internal scattering layer? In principle, this could be the case if the scattering strength needed for an efficient external extraction is higher than the scattering strength needed for the internal extraction. It would be interesting to study this with simulations.

[1] Internal extraction: Extracting photons from the OLED thin film system into the substrate.
[2] External extraction: Extracting photons from the substrate into the ambient.

Comparison to other simulation approaches: I believe that the simulation of internal scattering layers by means of the here presented approach is one of the most accurate and best justified simulation strategies, as it was derived from Maxwell's equations with the least amount of additional assumptions compared to other commonly applied approaches. However, despite the efforts to reduce the numerical workload, the full simulation of an OLED with internal scattering layer over the whole emission spectrum involves a considerable numerical effort, scaling in days rather than hours. Other, approximate simulation strategies like for example Monte Carlo ray tracing or approaches based on the radiative transfer transfer equation promise a much faster simulation time. It can be expected that in the limit of thick and dilute volumetric scattering layers, the coherent multiple scattering effects should become negligible such that the above-mentioned approximate methods are justified. A comparison of the here presented rigorous simulation method to these approximate approaches could shed light on the respective range of applicability.

More efficient multiple scattering in the limit of large particle numbers: The computational complexity of the iterative solution of equation (3.70) is proportional to the effort of a matrix-vector product of type $\sum_{S'} \sum_{n'} M_{n,n'}^{S,S'} b_{n'}^{S'}$, which naively scales quadratically with the particle number. So, even with lookup tables for the Sommerfeld integral and with execution on the graphics processing unit, in the limit of very large N_S the solution of (3.70) is no longer feasible. However, there are algorithms that reduce the complexity from N_S^2 to $N_\mathrm{S} \log N_\mathrm{S}$:

1. The *multi-level Fast Multipole Method (FMM)* relies on the hierarchical aggregation of scattering centers to larger units and the expansion of the joint scattered field in SVWFs relative to the center of these aggregates. This algorithm has been applied in various disciplines since the late 1980s [172] and was introduced in the context of the (acoustic) superposition T-matrix method by Gumerov and Duraiswami [173], and later for the electromagnetic superposition T-matrix method by Gimbutas and Greengard [174] and by Markkanen and Yuffa [175]. For flat scattering layers in a planarly layered medium, the FMM has been applied by Pissoort et al. [124], however they used an expansion in cylindrical vector wave functions rather than spherical vector wave functions. It would be interesting to study if and how the FMM can be used in the context of the T-matrix method for many particles inside a stratified medium.

2. Another approach to achieve $N_\mathrm{S} \log N_\mathrm{S}$ scaling is to first translate the particle positions to a regular grid (which is an operation with effort $\sim N_\mathrm{S}$) and to then accelerate the evaluation of the particle interaction by means of the *Fast Fourier Transform*. This approach has been widely applied in the context of the discrete dipole apprixmation (DDA) [176] and was later applied also to the superposition T-matrix method [99, 177]. Although the presence of a planarly layered background medium breaks the translational symmetry of the problem, it was demonstrated in the context of the DDA that the FFT acceleration can still be used, as the layered medium Green's function can be written as the sum of a

term that depends on $z_1 - z_2$ and one term that depends on $z_1 + z_2$ [117, 178] (see also section 3.10.1.1), where z_1 and z_2 are the z-coordinates of the emitter and receiver, respectively. This method should thus be applicable also to the formalism presented in this thesis. It would be interesting to study how much it can accelerate the computing time for systems with many particles.

Appendix

A. PVWF expansion: energy flux

The purpose of this appendix is to derive an expression for the electromagnetic power flux through a planar layer interface. The starting point is an electromagnetic field expanded in PVWFs, such that the electric field reads (compare (2.18)):

$$\mathbf{E}(\mathbf{r}) = \sum_{j=1}^{2} \int_{\mathbb{R}^2} \mathrm{d}^2\mathbf{k}_\parallel \left(g_j^+(\kappa,\alpha)\mathbf{\Phi}_j^+(\kappa,\alpha;\mathbf{r}) + g_j^-(\kappa,\alpha)\mathbf{\Phi}_j^-(\kappa,\alpha;\mathbf{r}) \right). \tag{A.1}$$

The magnetic field then takes the form:

$$\begin{aligned} \mathbf{H} &= \frac{1}{\mathrm{i}\omega\mu_0}\nabla\times\mathbf{E} \\ &= \frac{1}{\omega\mu_0}\sum_{j=1}^{2}\int \mathrm{d}^2\mathbf{k}_\parallel \left(g_j^+(\kappa,\alpha)\mathbf{k}^+\times\mathbf{\Phi}_j^+(\kappa,\alpha;\mathbf{r}) + g_j^-(\kappa,\alpha)\mathbf{k}^-\times\mathbf{\Phi}_j^-(\kappa,\alpha;\mathbf{r})\right) \end{aligned} \tag{A.2}$$

Knowing the electric and magnetic fields, the complex (conjugated) Poynting vector is defined as

$$\mathbf{S}^* = \frac{1}{2}\mathbf{E}^*\times\mathbf{H}. \tag{A.3}$$

It can be used to calculate the time averaged energy flux through an interface $z = z_0$:

$$\begin{aligned} \langle P_z\rangle &= \mathrm{Re}\int \mathrm{d}^2\mathbf{r}_\parallel\, \mathbf{S}^*\cdot\hat{\mathbf{e}}_z \\ &= \mathrm{Re}\,\frac{1}{2\omega\mu_0}\sum_{j,j'}\int \mathrm{d}^2\mathbf{r}_\parallel \int \mathrm{d}^2\mathbf{k}_\parallel \int \mathrm{d}^2\mathbf{k}'_\parallel \\ &\qquad \left(\left(g_{j'}^{+*}(\kappa',\alpha')\mathbf{\Phi}_{j'}^{+*}(\kappa',\alpha';\mathbf{r}) + g_{j'}^{-*}(\kappa',\alpha')\mathbf{\Phi}_{j'}^{-*}(\kappa',\alpha';\mathbf{r})\right)\right. \\ &\qquad \left.\times \left(g_j^+(\kappa,\alpha)\mathbf{k}^+\times\mathbf{\Phi}_j^+(\kappa,\alpha;\mathbf{r}) + g_j^-(\kappa,\alpha)\mathbf{k}^-\times\mathbf{\Phi}_j^-(\kappa,\alpha;\mathbf{r})\right)\right)_z. \end{aligned} \tag{A.4}$$

Inserting the definition of the PVWFs (see (2.15)), one can see that the term depending on $\mathbf{r}_\parallel$ is given by $\exp\left(\mathrm{i}\left(\mathbf{k}_\parallel - \mathbf{k}'_\parallel\right)\cdot\mathbf{r}_\parallel\right)$ and the $\mathbf{r}_\parallel$-integral yields

$$\int \mathrm{d}^2\mathbf{r}_\parallel \exp\left(\mathrm{i}\left(\mathbf{k}_\parallel - \mathbf{k}'_\parallel\right)\cdot\mathbf{r}_\parallel\right) = 4\pi^2\delta^2\left(\mathbf{k}_\parallel - \mathbf{k}'_\parallel\right). \tag{A.5}$$

Carrying out the $\mathbf{k}'_\parallel$ integral then yields

$$\begin{aligned}\langle P_z\rangle = \mathrm{Re}\,\frac{2\pi^2}{\omega\mu_0}\sum_j\sum_{j'}\int \mathrm{d}^2\mathbf{k}_\parallel \Big\{ &\left(g_{j'}^{+*}(\kappa,\alpha)\hat{\mathbf{e}}_{j'}^{+*} + g_{j'}^{-*}(\kappa,\alpha)\hat{\mathbf{e}}_{j'}^{-*}\right) \\ &\times \left(g_j^{+}(\kappa,\alpha)\mathbf{k}^{+}\times\hat{\mathbf{e}}_j^{+} + g_j^{-}(\kappa,\alpha)\mathbf{k}^{-}\times\hat{\mathbf{e}}_j^{-}\right)\Big\}_z .\end{aligned} \tag{A.6}$$

Further, recall that

$$\mathbf{k}^{\pm} = \begin{pmatrix}\kappa\cos\alpha\\ \kappa\sin\alpha\\ \pm k_z\end{pmatrix},\ \hat{\mathbf{e}}_1^{\pm} = \begin{pmatrix}-\sin\alpha\\ \cos\alpha\\ 0\end{pmatrix},\ \hat{\mathbf{e}}_2^{\pm} = \frac{1}{k}\begin{pmatrix}\pm k_z\cos\alpha\\ \pm k_z\sin\alpha\\ -\kappa\end{pmatrix} \tag{A.7}$$

such that

$$\mathbf{k}^{\pm}\times\hat{\mathbf{e}}_1 = -k\hat{\mathbf{e}}_2^{\pm} \tag{A.8}$$

$$\mathbf{k}^{\pm}\times\hat{\mathbf{e}}_2^{\pm} = k\hat{\mathbf{e}}_1 \tag{A.9}$$

$$\hat{\mathbf{e}}_1^{*}\times\hat{\mathbf{e}}_2^{\pm} = -\frac{1}{k}\mathbf{k}^{\pm} \tag{A.10}$$

$$\hat{\mathbf{e}}_2^{\pm *}\times\hat{\mathbf{e}}_1 = \frac{1}{k}\mathbf{k}^{\pm *} \tag{A.11}$$

$$\hat{\mathbf{e}}_1^{*}\times\hat{\mathbf{e}}_1 = \mathbf{0} \tag{A.12}$$

$$\left(\hat{\mathbf{e}}_2^{\pm *}\times\hat{\mathbf{e}}_2^{\pm}\right)_z = 0. \tag{A.13}$$

Therefore, $\hat{\mathbf{e}}_1^{*}\times\left(\mathbf{k}^{\pm}\times\hat{\mathbf{e}}_2^{\pm}\right) = \mathbf{0}$ and $\left(\hat{\mathbf{e}}_2^{*}\times\left(\mathbf{k}^{\pm}\times\hat{\mathbf{e}}_1\right)\right)_z = 0$ such that only in the case $j = j'$ a non zero integrand remains. I evaluate

$$\begin{aligned}\hat{\mathbf{e}}_1^{*}\times\left(\mathbf{k}^{\pm}\times\hat{\mathbf{e}}_1\right) &= -k\hat{\mathbf{e}}_1^{*}\times\hat{\mathbf{e}}_2^{\pm} \\ &= \mathbf{k}^{\pm}\end{aligned} \tag{A.14}$$

$$\begin{aligned}\hat{\mathbf{e}}_2^{+*}\times\left(\mathbf{k}^{\pm}\times\hat{\mathbf{e}}_2^{\pm}\right) &= k\hat{\mathbf{e}}_2^{+*}\times\hat{\mathbf{e}}_1 \\ &= \mathbf{k}^{*}\end{aligned} \tag{A.15}$$

$$\hat{\mathbf{e}}_2^{-*}\times\left(\mathbf{k}^{\pm}\times\hat{\mathbf{e}}_2^{\pm}\right) = \mathbf{k}^{-*}. \tag{A.16}$$

to finally find

$$\begin{aligned}\langle P_z\rangle &= \frac{2\pi^2}{\omega\mu_0}\,\mathrm{Re}\int \mathrm{d}^2\mathbf{k}_\parallel \Big\{k_z\left(g_1^{+*}(\kappa,\alpha)+g_1^{-*}(\kappa,\alpha)\right)\left(g_1^{+}(\kappa,\alpha)-g_1^{-}(\kappa,\alpha)\right) \\ &\qquad +k_z^{*}\left(g_2^{+*}(\kappa,\alpha)-g_2^{-*}(\kappa,\alpha)\right)\left(g_2^{+}(\kappa,\alpha)+g_2^{-}(\kappa,\alpha)\right)\Big\} \\ &= \frac{2\pi^2}{\omega\mu_0}\sum_{j=1}^{2}\int_{\mathbb{R}^2}\mathrm{d}^2\mathbf{k}_\parallel \Big\{\mathrm{Re}\,(k_z)\left(\left|g_j^{+}(\kappa,\alpha)\right|^2-\left|g_j^{-}(\kappa,\alpha)\right|^2\right) \\ &\qquad -2\,\mathrm{Im}\,(k_z)\,\mathrm{Im}\left(g_j^{+}(\kappa,\alpha)g_j^{-*}(\kappa,\alpha)\right)\Big\}\end{aligned}$$

Note that the integrand is not an analytic function of κ such that a deflection of the integration contour into the complex plane is not permitted.

B. SVWF addition theorem

I use the expressions given in the appendix of [135] that have been adapted to the normalization conventions used in this document:

$$\mathbf{\Psi}_n^{(3)}(\mathbf{r}+\mathbf{d}) = \sum_n A_{nn'}(\mathbf{d})\mathbf{\Psi}_{n'}^{(1)}(\mathbf{r}), \quad |\mathbf{r}| < |\mathbf{d}|, \tag{B.1}$$

for

$$A_{n,n'}(\mathbf{d}) = \delta_{pp'} A_{ml,m'l'}(\mathbf{d}) + (1-\delta_{pp'}) B_{ml,m'l'}(\mathbf{d}) \tag{B.2}$$

with

$$A_{ml,m'l'}(\mathbf{d}) = \mathrm{e}^{\mathrm{i}(m-m')\phi_d} \sum_{\lambda=|l-l'|}^{l+l'} a_5(l,m|l',m'|\lambda)\, h_\lambda^{(1)}(kd)\, P_\lambda^{|m-m'|}(\cos\theta_d) \tag{B.3}$$

$$B_{ml,m'l'}(\mathbf{d}) = \mathrm{e}^{\mathrm{i}(m-m')\phi_d} \sum_{\lambda=|l-l'|+1}^{l+l'} b_5(l,m|l',m'|\lambda)\, h_\lambda^{(1)}(kd)\, P_\lambda^{|m-m'|}(\cos\theta_d), \tag{B.4}$$

where

$$\begin{aligned} a_5(l,m|l',m'|p) = {} & \mathrm{i}^{|m-m'|-|m|-|m'|+l'-l+p}(-1)^{m-m'}\sqrt{\frac{(2l+1)(2l'+1)}{2l(l+1)l'(l'+1)}} \\ & \times \left(l(l+1)+l'(l'+1)-p(p+1)\right)\sqrt{2p+1} \\ & \times \begin{pmatrix} l & l' & p \\ m & -m' & -(m-m') \end{pmatrix} \begin{pmatrix} l & l' & p \\ 0 & 0 & 0 \end{pmatrix} \end{aligned} \tag{B.5}$$

$$\begin{aligned} b_5(l,m|l',m'|p) = {} & \mathrm{i}^{|m-m'|-|m|-|m'|+l'-l+p}(-1)^{m-m'}\sqrt{\frac{(2l'+1)(2l+1)}{2l(l+1)l'(l'+1)}} \\ & \times \sqrt{(l+l'+1+p)(l+l'+1-p)(p+l-l')(p-l+l')(2p+1)} \\ & \times \begin{pmatrix} l & l' & p \\ m & -m' & -(m-m') \end{pmatrix} \begin{pmatrix} l & l' & p-1 \\ 0 & 0 & 0 \end{pmatrix} \end{aligned} \tag{B.6}$$

and (d, θ_d, ϕ_d) are the spherical coordinates of $\mathbf{d}$, whereas $\begin{pmatrix} \cdots \\ \cdots \end{pmatrix}$ denote the Wigner-3j symbols.

C. Excitation and response (formal definition)

For a formal definition of $\mathbf{E}_{\text{exc}}$ and $\mathbf{E}^{\text{R}}_{\text{exc}}$ (see section 2.4.3), let $z^{\downarrow}$ and $z^{\uparrow}$ denote two z-surfaces that bound the source domain D_{exc} from below and above, i.e.,

$$z^{\downarrow} < z < z^{\uparrow} \qquad \text{for all } \mathbf{r} \in D_{\text{exc}}.$$

The regions (see figure C.1)

$$D^{\downarrow} = \{\mathbf{r} \in \Lambda_{i_{\text{exc}}} | z < z^{\downarrow}\}$$

and

$$D^{\uparrow} = \{\mathbf{r} \in \Lambda_{i_{\text{exc}}} | z > z^{\uparrow}\}$$

are homogeneous and source-free and thus allow for an expansion of the electric field in PVWFs. I denote the coefficients of these PVWF expansions by $g^{\pm}_{\downarrow,j}$ and $g^{\pm}_{\uparrow,j}$, respectively.

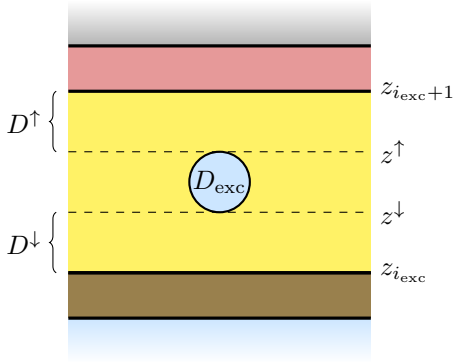

Figure C.1. – Regions $D^{\uparrow}$ and $D^{\downarrow}$.

The formal decomposition of $\mathbf{E}$ into excitation and response is now guided by the idea that for the excitation, no downgoing component should exist above D_{exc} and no upgoing component below D_{exc}, whereas for the response, the expansion in PVWFs should be valid in the whole layer $\Lambda_{i_{\text{exc}}}$ such that the coefficients above D_{exc} should

match those below D_{exc}. This leads to the following definition:

$$\mathbf{E}_{\text{exc}}(\mathbf{r}) = \sum_{j=1}^{2} \int_{\mathbb{R}^2} \mathrm{d}^2\mathbf{k}_\parallel \begin{cases} \mathbf{\Phi}_j^+(\kappa,\alpha;\mathbf{r}-\mathbf{r}_{i_{\text{exc}}}) g_{\text{exc},j}^+(\kappa,\alpha) & \text{for } z \geq z^+ \\ \mathbf{\Phi}_j^-(\kappa,\alpha;\mathbf{r}-\mathbf{r}_{i_{\text{exc}}}) g_{\text{exc},j}^-(\kappa,\alpha) & \text{for } z \leq z^-. \end{cases}$$

$$\mathbf{E}_{\text{exc}}^{\text{R}}(\mathbf{r}) = \sum_{j=1}^{2} \int_{\mathbb{R}^2} \mathrm{d}^2\mathbf{k}_\parallel \left[\mathbf{\Phi}_j^+(\kappa,\alpha;\mathbf{r}-\mathbf{r}_{i_{\text{exc}}}), \mathbf{\Phi}_j^-(\kappa,\alpha;\mathbf{r}-\mathbf{r}_{i_{\text{exc}}})\right] \cdot \begin{bmatrix} g_{\text{exc},i_{\text{exc}},j}^{\text{R}+}(\kappa,\alpha) \\ g_{\text{exc},i_{\text{exc}},j}^{\text{R}-}(\kappa,\alpha) \end{bmatrix}$$

for $\mathbf{r} \in \Lambda_{i_{\text{exc}}}$ and with

$$g_{\text{exc},i_{\text{exc}},j}^{R+}(\kappa,\alpha) = g_{\downarrow,j}^+(\kappa,\alpha) \tag{C.1}$$

$$g_{\text{exc},i_{\text{exc}},j}^{R-}(\kappa,\alpha) = g_{\uparrow,j}^-(\kappa,\alpha) \tag{C.2}$$

and

$$g_{\text{exc},j}^+(\kappa,\alpha) = g_{\uparrow,j}^+(\kappa,\alpha) - g_{\downarrow,j}^+(\kappa,\alpha) \tag{C.3}$$

$$g_{\text{exc},j}^-(\kappa,\alpha) = g_{\downarrow,j}^-(\kappa,\alpha) - g_{\uparrow,j}^-(\kappa,\alpha). \tag{C.4}$$

In the other layers $i \neq i_{\text{exc}}$, the electric field is source-free and can thus be expanded in PVWFs, with coefficients that I denote by $g_{\text{exc},i,j}^{\text{R}\pm}$:

$$\mathbf{E}(\mathbf{r}) = \sum_{j=1}^{2} \int_{\mathbb{R}^2} \mathrm{d}^2\mathbf{k}_\parallel \left[\mathbf{\Phi}_j^+(\kappa,\alpha;\mathbf{r}-\mathbf{r}_i), \mathbf{\Phi}_j^-(\kappa,\alpha;\mathbf{r}-\mathbf{r}_i)\right] \cdot \begin{bmatrix} g_{\text{exc},i,j}^{\text{R}+}(\kappa,\alpha) \\ g_{\text{exc},i,j}^{\text{R}-}(\kappa,\alpha) \end{bmatrix}$$

D. Tests for the conservation of energy

The following code shows a test for the scattering of a plane wave by three spheres in a medium consisting of three planar layers.

```
import numpy as np
import smuthi.particles as part
import smuthi.layers as lay
import smuthi.initial_field as init
import smuthi.coordinates as coord
import smuthi.simulation as simul
import smuthi.scattered_field as sf


vacuum_wavelength = 550

# set complex contour
coord.set_default_k_parallel(vacuum_wavelength, neff_max=3)

# initialize particle objects
sphere1 = part.Sphere(position=[100, 100, 150],
                      refractive_index=2.4 + 0.0j,
                      radius=110,
                      l_max=4, m_max=4)

sphere2 = part.Sphere(position=[-100, -100, 250],
                      refractive_index=1.9 + 0.0j,
                      radius=120,
                      l_max=3, m_max=3)

sphere3 = part.Sphere(position=[-200, 100, 300],
                      refractive_index=1.7 + 0.0j,
                      radius=90,
                      l_max=3, m_max=3)

particle_list = [sphere1, sphere2, sphere3]

# initialize layer system object
lay_sys = lay.LayerSystem(thicknesses=[0, 400, 0],
                          refractive_indices=[2, 1.3, 2])

# initialize initial field object
init_fld = init.PlaneWave(vacuum_wavelength=vacuum_wavelength,
```

```
                            polar_angle=np.pi * 7/8,
                            azimuthal_angle=np.pi * 1/3,
                            polarization=0,
                            amplitude=1,
                            reference_point=[0, 0, 400])

# initialize and run simulation
simulation = simul.Simulation(layer_system=lay_sys,
                              particle_list=particle_list,
                              initial_field=init_fld)
simulation.run()

# scattering cross section
scs = sf.scattering_cross_section(initial_field=init_fld,
                                  particle_list=particle_list,
                                  layer_system=lay_sys)

# extinction cross section
ecs = sf.extinction_cross_section(initial_field=init_fld,
                                  particle_list=particle_list,
                                  layer_system=lay_sys)


def test_optical_theorem():
    relerr = abs((sum(scs.integral()) - ecs['top'] - ecs['bottom'])
                 / sum(scs.integral()))
    print('error: ', relerr)
    assert relerr < 1e-4


if __name__ == '__main__':
    test_optical_theorem()
```

The following code shows a test for the scattering of a Gaussian beam by the same configuration as before.

```
import numpy as np
import smuthi.particles as part
import smuthi.layers as lay
import smuthi.initial_field as init
import smuthi.coordinates as coord
import smuthi.simulation as simul
import smuthi.scattered_field as sf


vacuum_wavelength = 550

# set complex contour
coord.set_default_k_parallel(vacuum_wavelength, neff_max=3)


# initialize particle object
sphere1 = part.Sphere(position=[100, 100, 150],
```

```
                        refractive_index=2.4 + 0.0j,
                        radius=110,
                        l_max=4, m_max=4)

sphere2 = part.Sphere(position=[-100, -100, 250],
                        refractive_index=1.9 + 0.0j,
                        radius=120,
                        l_max=3, m_max=3)

sphere3 = part.Sphere(position=[-200, 100, 300],
                        refractive_index=1.7 + 0.0j,
                        radius=90, l_max=3, m_max=3)

particle_list = [sphere1, sphere2, sphere3]

# initialize layer system object
lay_sys = lay.LayerSystem(thicknesses=[0, 400, 0],
                          refractive_indices=[2, 1.4, 2])

# initialize initial field object
beam_k_parallel = (np.linspace(0, 2, 501, endpoint=False)
                   * coord.angular_frequency(vacuum_wavelength))

init_fld = init.GaussianBeam(vacuum_wavelength=vacuum_wavelength,
                             polar_angle=np.pi * 7/8,
                             azimuthal_angle=np.pi * 1/3,
                             polarization=0,
                             amplitude=1,
                             reference_point=[200, 200, 200],
                             beam_waist=1000,
                             k_parallel_array=beam_k_parallel)

# initialize and run simulation
simulation = simul.Simulation(layer_system=lay_sys,
                              particle_list=particle_list,
                              initial_field=init_fld)

simulation.run()

total_far_field,_,_ = sf.total_far_field(initial_field=init_fld,
                                         particle_list=particle_list,
                                         layer_system=lay_sys)

def test_power():
    relerr = abs(sum(total_far_field.integral())
                 / sum(init_fld.initial_intensity(lay_sys).integral()) - 1)
    print(relerr)
    assert relerr < 1e-4


if __name__ == '__main__':
    test_power()
```

The following code shows a test for the scattering of the field of three arbitrary dipole sources by the same configuration as before.

```
import smuthi.initial_field as init
import smuthi.particles as part
import smuthi.coordinates as coord
import smuthi.simulation as simul
import smuthi.layers as lay
import smuthi.scattered_field as sf


vacuum_wavelength = 550

coord.set_default_k_parallel(vacuum_wavelength, neff_max=3)

# initialize particle object
sphere1 = part.Sphere(position=[200, 200, 300],
                      refractive_index=2.4 + 0.0j,
                      radius=110,
                      l_max=3, m_max=3)

sphere2 = part.Sphere(position=[-200, -200, 300],
                      refractive_index=2.4 + 0.0j,
                      radius=120,
                      l_max=3, m_max=3)

sphere3 = part.Sphere(position=[-200, 200, 300],
                      refractive_index=2.5 + 0.0j,
                      radius=90,
                      l_max=3, m_max=3)

part_list = [sphere1, sphere2, sphere3]

# initialize layer system object
lay_sys = lay.LayerSystem(thicknesses=[0, 400, 0],
                          refractive_indices=[2, 1.3, 2])

# initialize dipole objects
dipole_collection = init.DipoleCollection(vacuum_wavelength)

dipole1 = init.DipoleSource(vacuum_wavelength,
                            dipole_moment=[1+1j,2+2j,3+3j],
                            position=[100,-100,130])
dipole_collection.append(dipole1)


dipole2 = init.DipoleSource(vacuum_wavelength,
                           dipole_moment=[3,-2,1],
                           position=[-100,100,70])
dipole_collection.append(dipole2)

dipole3 = init.DipoleSource(vacuum_wavelength,
                           dipole_moment=[-2,3,1],
```

```
                              position=[-100,100,-100])
dipole_collection.append(dipole3)

# initialize and run simulation
simulation = simul.Simulation(layer_system=lay_sys,
                              particle_list=part_list,
                              initial_field=dipole_collection)

simulation.run()

# dissipated power
power_list = simulation.initial_field.dissipated_power(part_list,
                                                       lay_sys)
power = sum(power_list)

# radiated power
ff_tup = sf.total_far_field(initial_field=simulation.initial_field,
                            particle_list=simulation.particle_list,
                            layer_system=simulation.layer_system)
ff_power = sum(ff_tup[0].integral())


def test_energy_conservation():
    err = abs((power - ff_power) / ff_power)
    print('far field power:', ff_power)
    print('dissipated power:', power)
    print('relative error:', err)
    assert err < 1e-4


if __name__ == '__main__':
    test_energy_conservation()
```

Danksagung

Die Forschungen zu diesem Thema haben fast sechs Jahre gedauert, und während dieser Zeit habe ich viele bereichernde Kontakte mit Mentoren, Kollegen und Freunden erlebt. Es ist mir eine Freude, diese Zeit zu rekapitulieren und meine Dankbarkeit auszudrücken.

An erster Stelle möchte ich mich bei Uli Lemmer bedanken. Sein Betreuungsstil ist eine glückliche Mischung aus Freiheit und Rückhalt, und von einem positiven Menschenbild geprägt. Die Zeit am LTI wird mir dadurch in bester Erinnerung bleiben.

Ein ganz besonderes Dankeschön gilt Siegfried Kettlitz für seine Freundschaft und Kollegialität. Er hat diese Arbeit sowohl auf fachlicher als auch auf moralischer Ebene wesentlich unterstützt.

Guillaume Gomard danke ich für die freundschaftliche und fruchtbare Zusammenarbeit. Besonders die Antragsphase des LAMBDA-Projektes wird mir in diesem Zusammenhang in Erinnerung bleiben.

Thomas Wriedt ist in vielerlei Hinsicht eine wichtige Quelle von Unterstützung gewesen: durch die jährliche Organisation des Bremer Workshops über Lichtstreuung, durch viele Fachgespräche und -beratungen sowie durch sein ermutigendes Feedback. Danke!

A special thanks goes to Yuri Eremin for the collaboration on light scattering by flat particles on a substrate. It was a pleasure to learn from him.

Adrian Doicu, Yuri Eremin and Thomas Wriedt generously allowed me use their code (NFM-DS) with Smuthi.

Diederik Wiersma and the group of Optics at complex systems at the LENS in Florence (Italy) have hosted me as a guest for three months. This time was a highlight of my studies. I want thank Diederik for his welcoming and positive energy. Dmitry Nuzhdin and Giacomo Mazzamuto supported me in many regards. During that time, a long lasting and fruitful collaboration with Lorenzo Pattelli began, for which I am deeply grateful. Lorenzo's enthusiasm for structure in the disorder and his aesthetic view on science are simply unique.

I wish to thank Alan Zhan and Konstantin Ladutenko for their valuable contributions to the CELES and Smuthi code, respectively.

Daniel Mackowski and Gerhard Kristensson supported me with helpful advice.

I want to thank Michael Mishchenko and Jose Stoop from Elsevier for the 2018 JQSRT/Waterman award. This support was so important and makes a huge difference.

Carsten Rockstuhl danke ich für die Übernahme des Korreferates, für hilfreiches Feedback zur Dissertation sowie für den fachlichen Austausch über theoretische Fragestellungen zur T-Matrix Methode. Hier gilt mein Dank auch seinen Gruppenmitgliedern Aso Rahimzadegan und Radius Nagassa Suryadharma für die Zusammenarbeit.

Den Kollegen Tobias Bocksrocker, Stefan Höfle, Jan Preinfalk und Yidenekachew Donie, die experimentell an OLEDs und/oder Streuschichten gearbeitet haben, möchte ich für die gute Zusammenarbeit und die vielen fachlichen Diskussionen danken.

Den Studenten, welche ich während ihrer Abschlussarbeiten betreuen durfte, danke ich für die vertrauensvolle Zusammenarbeit und ihre wichtigen Beiträge zu dieser Arbeit: Tanja Kempfert half mir beim Erschließen der Sommerfeld'schen Theorie über Dipolstrahlung nahe ebener Grenzflächen. Christian Berten legte den Grundstein für die Kombinatin von makro- und mikrooptischen Simulationen am LTI. Christian Yorck half beim Aufbau des Prototyps von Smuthi und bei der Umnormierung der sphärischen Vektorwellenfunktionen. Matthias Hecht hat in seiner Arbeit demonstriert, dass kollimierte und flächige OLED-Abstrahlung einander nicht ausschließen. Aus dieser Arbeit ging sogar eine Patentanmeldung hervor. Julian Bolter analysierte die statistische Fehlerfortpflanzung bei der Schätzung der Emittereigenschaften von OLEDs aus dem Abstrahlprofil. Dominik Theobald erweiterte Smuthi um die Simulation von nicht kugelförmigen Partikeln (Ellipsoide und Zylinder). Aus dieser Arbeit ist eine fortwährende, sehr fruchtbare Kollaboration erwachsen, für die ich sehr dankbar bin. Swantje Pauer untersuchte experimentell die gezielte Anregung von Wellenleitermoden in Dünnschichtsystemen mit Streuschicht. Christian Stamm widmete seine Masterarbeit der Planarisierung von Streuschichten aus der Polymer-Blend Lithografie.

Frs Korrekturlesen dieser Arbeit bedanke ich mich bei Jan Preinfalk, Guillaume Gomard, Jonathan Lehr, Philipp Brenner, Dominik Theobald und Yidenekachew Donie.

André Gall danke ich für die Zurverfügungstellung eines leistungsfähigen Simulationsrechners. Weitere wertvolle Unterstützung beim Aussuchen und bei der Beschaffung von Computerhardware habe ich durch Malte Langenhorst und Raphael Schmager erfahren. Dem bwUniCluster danke ich für die oft genutzte Möglichkeit, große FEM-Simulationen durchzuführen.

Dem Team der Karlsruhe School of Optics & Photonics danke ich für die fortwährende finanzielle und inhaltliche Unterstützung meiner Promotionsstudien. Dem Karlsruhe House of Young Scientists danke ich für die finanzielle Unterstützung meines Italienaufenthaltes.

Klaus Trampert danke ich herzlich für die fachlichen Diskussionen und seine Unterstützung in der optischen Metrologie.

Ohne folgende Personen wäre ein Forschen am LTI nicht mglich gewesen: Astrid Henne und Claudia Holeisen im Sekretariat; Felix Geislhöringer als Seele des Instituts; Siegfried Kettlitz, Carsten Eschenbaum, Jonathan Lehr und Dominik Theobald als Netzwerkadministratoren.

Im Simulantenbüro habe ich mich immer sehr wohl gefühlt. Für die angenehme und kollegiale Atmosphäre danke ich Carola Moosmann, Jan Mescher, Nico Christ, Jonathan Lehr, Matthias Hecht, Philipp Brenner und Dominik Theobald.

Adrian Mertens, nie um ein Bonmot oder einen Schüttelreim verlegen, hat mich oft zum Lachen gebracht. Ich danke ihm außerdem für die Mittagessen-Tombola.

Horst Greiner danke ich für den kontinuierlichen Austausch. Seine Arbeiten sind eine wichtige Inspirationsquelle für diese Dissertation.

Gotthard Weißflog und den übrigen Kollaborationspartnern im OLIB Netzwerk bin ich für die vertrauensvolle Zusammenarbeit sowie für ihren Pioniergeist im Bereich der OLED-Technologie dankbar.

List of Figures

List of Tables

Bibliography

[1] Guillaume Gomard, Jan B Preinfalk, Amos Egel, and Uli Lemmer. Photon management in solution-processed organic light-emitting diodes: a review of light outcoupling micro-and nanostructures. *Journal of Photonics for Energy*, 6(3):030901, 2016.

[2] P C Waterman. Matrix formulation of electromagnetic scattering. *Proc. IEEE*, 53(8):805–812, 1965.

[3] A.V. Tishchenko. Modelling of light extraction from oleds. In Alastair Buckley, editor, *Organic Light-Emitting Diodes (OLEDs)*, Woodhead Publishing Series in Electronic and Optical Materials, pages 262 – 292. Woodhead Publishing, 2013.

[4] Bo Peterson and Staffan Ström. T matrix for electromagnetic scattering from an arbitrary number of scatterers and representations of E(3). *Physical review D*, 8(10):3661, 1973.

[5] Gerhard Kristensson. Electromagnetic scattering from buried inhomogeneities – a general three-dimensional formalism. *Journal of Applied Physics*, 51(7):3486–3500, 1980.

[6] Daniel W Mackowski. Exact solution for the scattering and absorption properties of sphere clusters on a plane surface. *Journal of Quantitative Spectroscopy and Radiative Transfer*, 109(5):770–788, 2008.

[7] Chihaya Adachi, Marc A. Baldo, Mark E. Thompson, and Stephen R. Forrest. Nearly 100% internal phosphorescence efficiency in an organic light-emitting device. *J. Appl. Phys.*, 90(10):5048–5051, nov 2001.

[8] Ayataka Endo, Mai Ogasawara, Atsushi Takahashi, Daisuke Yokoyama, Yoshimine Kato, and Chihaya Adachi. Thermally activated delayed fluorescence from sn4+–porphyrin complexes and their application to organic light emitting diodesa novel mechanism for electroluminescence. *Advanced Materials*, 21(47):4802–4806, 2009.

[9] Wolfgang Brütting, Jörg Frischeisen, Tobias D. Schmidt, Bert J. Scholz, and Christian Mayr. Device efficiency of organic light-emitting diodes: Progress by improved light outcoupling. *Phys. status solidi*, 210(1):44–65, jan 2013.

[10] Sebastian Reineke, Michael Thomschke, Björn Lüssem, and Karl Leo. White organic light-emitting diodes: Status and perspective. *Rev. Mod. Phys.*, 85(3):1245–1293, jul 2013.

[11] Kanchan Saxena, V K Jain, and Dalip Singh Mehta. A review on the light extraction techniques in organic electroluminescent devices. *Opt. Mater. (Amst).*, 32(1):221–233, 2009.

[12] Kihyon Hong and Jong-Lam Lee. Review paper: Recent developments in light extraction technologies of organic light emitting diodes. *Electron. Mater. Lett.*, 7(2):77–91, jun 2011.

[13] M.C. Gather and S. Reineke. Recent advances in light outcoupling from white organic light-emitting diodes. *J. Photonics Energy*, 5:057607, 2015.

[14] Ji-Seon Kim, Peter K. H. Ho, Neil C. Greenham, and Richard H. Friend. Electroluminescence emission pattern of organic light-emitting diodes: Implications for device efficiency calculations. *Journal of Applied Physics*, 88(2):1073–1081, 2000.

[15] Michael Flämmich, Malte C. Gather, Norbert Danz, Dirk Michaelis, Andreas H. Bräuer, Klaus Meerholz, and Andreas Tünnermann. Orientation of emissive dipoles in oleds: Quantitative in situ analysis. *Organic Electronics*, 11(6):1039 – 1046, 2010.

[16] Michael Flämmich Dr. rer. nat. *Optical Characterization of OLED Emitter Properties by Radiation Pattern Analyses*. PhD thesis.

[17] Christian Mayr, Sae Youn Lee, Tobias D. Schmidt, Takuma Yasuda, Chihaya Adachi, and Wolfgang Brtting. Efficiency enhancement of organic light-emitting diodes incorporating a highly oriented thermally activated delayed fluorescence emitter. *Advanced Functional Materials*, 24(33):5232–5239, 2014.

[18] Horst Greiner. Light extraction from organic light emitting diode substrates: Simulation and experiment. *Japanese Journal of Applied Physics*, 46(7R):4125, 2007.

[19] Malte C. Gather, Michael Flämmich, Norbert Danz, Dirk Michaelis, and Klaus Meerholz. Measuring the profile of the emission zone in polymeric organic light-emitting diodes. *Appl. Phys. Lett.*, 94(26):263301, 2009.

[20] Michael Flämmich, Malte C. Gather, Norbert Danz, Dirk Michaelis, and Klaus Meerholz. In situ measurement of the internal luminescence quantum efficiency in organic light-emitting diodes. *Appl. Phys. Lett.*, 95(26):263306, 2009.

[21] B. Perucco, N. A. Reinke, D. Rezzonico, M. Moos, and B. Ruhstaller. Analysis of the emission profile in organic light-emitting devices. *Opt. Express*, 18(S2):A246–A260, Jun 2010.

[22] Michael Flämmich, Malte C Gather, Norbert Danz, Dirk Michaelis, Andreas H Bräuer, Klaus Meerholz, and Andreas Tünnermann. Orientation of emissive dipoles in OLEDs: Quantitative in situ analysis. *Org. Electron.*, 11(6):1039–1046, 2010.

[23] J. J. Shiang, T. J. Faircloth, and Anil R. Duggal. Experimental demonstration of increased organic light emitting device output via volumetric light scattering. *Journal of Applied Physics*, 95(5):2889–2895, 2004.

[24] R. Bathelt, D. Buchhauser, C. Grditz, R. Paetzold, and P. Wellmann. Light extraction from oleds for lighting applications through light scattering. *Organic Electronics*, 8(4):293 – 299, 2007.

[25] Yuan-Sheng Tyan, YuanQiao Rao, Jin-Shan Wang, Raymond Kesel, Thomas R. Cushman, and William J. Begley. 61.2: Fluorescent white oled devices with improved light extraction. *SID Symposium Digest of Technical Papers*, 39(1):933–936, 2008.

[26] Hong-Wei Chang, Yong Hyun Kim, Jonghee Lee, Simone Hofmann, Björn Lüssem, Lars Müller-Meskamp, Malte C. Gather, Karl Leo, and Chung-Chih Wu. Color-stable, ITO-free white organic light-emitting diodes with enhanced efficiency using solution-processed transparent electrodes and optical outcoupling layers. *Org. Electron.*, 15(5):1028–1034, may 2014.

[27] S. Möller and S. R. Forrest. Improved light out-coupling in organic light emitting diodes employing ordered microlens arrays. *Journal of Applied Physics*, 91(5):3324–3327, 2002.

[28] Yiru Sun and Stephen R. Forrest. Organic light emitting devices with enhanced outcoupling via microlenses fabricated by imprint lithography. *Journal of Applied Physics*, 100(7):073106, 2006.

[29] Sang-Hyun Eom, Edward Wrzesniewski, and Jiangeng Xue. Close-packed hemispherical microlens arrays for light extraction enhancement in organic light-emitting devices. *Organic Electronics*, 12(3):472 – 476, 2011.

[30] Francesco Galeotti, Wojciech Mrz, Guido Scavia, and Chiara Botta. Microlens arrays for light extraction enhancement in organic light-emitting diodes: A facile approach. *Organic Electronics*, 14(1):212 – 218, 2013.

[31] Amos Egel, Tobias Bocksrocker, and Uli Lemmer. Extracting substrate modes from flexible oleds. In *Renewable Energy and the Environment*, page DT2E.3. Optical Society of America, 2013.

[32] H. J. Peng, Y. L. Ho, C. F. Qiu, M. Wong, and H. S. Kwok. Coupling Efficiency Enhancement of Organic Light Emitting Devices with Refractive Microlens Array on High Index Glass Substrate. *SID Symp. Dig. Tech. Pap.*, 35(1):158, 2004.

[33] Toshitaka Nakamura, Naoto Tsutsumi, Noriyuki Juni, and Hironaka Fujii. Thin-film waveguiding mode light extraction in organic electroluminescent device using high refractive index substrate. *J. Appl. Phys.*, 97(5):054505, mar 2005.

[34] Georg Gaertner and Horst Greiner. Light extraction from OLEDS with (high) index matched glass substrates. In Paul L. Heremans, Michele Muccini, and Eric A. Meulenkamp, editors, *SPIE Proc.*, page 69992T. International Society for Optics and Photonics, apr 2008.

[35] B. J. Matterson, J. M. Lupton, A. F. Safonov, M. G. Salt, W. L. Barnes, and I. D. W. Samuel. Increased efficiency and controlled light output from a microstructured light-emitting diode. *Advanced Materials*, 13(2):123–127, 2001.

[36] J. M. Ziebarth, A. K. Saafir, S Fan, and M. D. McGehee. Extracting Light from Polymer Light-Emitting Diodes Using Stamped Bragg Gratings. *Adv. Funct. Mater.*, 14(5):451–456, 2004.

[37] Julian Hauss, Tobias Bocksrocker, Boris Riedel, Ulf Geyer, Uli Lemmer, and Martina Gerken. Metallic Bragg-gratings for light management in organic light-emitting devices. *Appl. Phys. Lett.*, 99(10):103303, sep 2011.

[38] T Bocksrocker, J B Preinfalk, J Asche-Tauscher, A Pargner, C Eschenbaum, F Maier-Flaig, and U Lemmer. White organic light emitting diodes with enhanced internal and external outcoupling for ultra-efficient light extraction and Lambertian emission. *Opt. Express*, 20(23):A932–A940, 2012.

[39] Christian Kluge, Michael Rädler, Arfat Pradana, Matthias Bremer, Peter-Jürgen Jakobs, Nicole Barié, Markus Guttmann, and Martina Gerken. Extraction of guided modes from organic emission layers by compound binary gratings. *Opt. Lett.*, 37(13):2646–2648, jul 2012.

[40] Sang-Jun Park, Yang Doo Kim, Ho Won Lee, Hyung Jin Yang, Joong-Yeon Cho, Young Kwan Kim, and Heon Lee. Enhancement of light extraction efficiency of oleds using si 3 n 4-based optical scattering layer. *Optics Express*, 22(10):12392–12397, 2014.

[41] Arfat Pradana and Martina Gerken. Photonic crystal slabs in flexible organic light-emitting diodes. *Photonics Res.*, 3(2):32, apr 2015.

[42] Yong-Jae Lee, Se-Heon Kim, Joon Huh, Guk-Hyun Kim, Yong-Hee Lee, Sang-Hwan Cho, Yoon-Chang Kim, and Young Rag Do. A high-extraction-efficiency nanopatterned organic light-emitting diode. *Appl. Phys. Lett.*, 82(21):3779–3781, 2003.

[43] M. Fujita, T. Ueno, T. Asano, S. Noda, H. Ohhata, T. Tsuji, H. Nakada, and N. Shimoji. Organic light-emitting diode with ITO/organic photonic crystal. *Electron. Lett.*, 39(24):1750, 2003.

[44] Young Rag Do, Yoon-Chang C Kim, Young-Woo W Song, and Yong-Hee H Lee. Enhanced light extraction efficiency from organic light emitting diodes by insertion of a two-dimensional photonic crystal structure. *J. Appl. Phys.*, 96(12):7629–7636, 2004.

[45] Yong-Jae Lee, Se-Heon Kim, Guk-Hyun Kim, Yong-Hee Lee, Sang-Hwan Cho, Young-Woo Song, Yoon-Chang Kim, and Young Rag Do. Far-field radiation of photonic crystal organic light-emitting diode. *Opt. Express*, 13(15):5864–5870, jul 2005.

[46] Jin-Wook Shin, Doo-Hee Cho, Jaehyun Moon, Chul Woong Joo, Seung Koo Park, Jonghee Lee, Jun-Han Han, Nam Sung Cho, Joohyun Hwang, Jin Woo Huh, Hye Yong Chu, and Jeong-Ik Lee. Random nano-structures as light extraction functionals for organic light-emitting diode applications. *Org. Electron.*, 15(1):196–202, 2014.

[47] Jun-Whee Kim, Ji-Hyang Jang, Min-Cheol Oh, Jin-Wook Shin, Doo-Hee Cho, Jae-Hyun Moon, and Jeong-Ik Lee. FDTD analysis of the light extraction efficiency of OLEDs with a random scattering layer. *Opt. Express*, 22(1):498–507, jan 2014.

[48] Keunsoo Lee, Jin-Wook Shin, Jun-Hwan Park, Jonghee Lee, Chul Woong Joo, Jeong-Ik Lee, Doo-Hee Cho, Jong Tae Lim, Min-Cheol Oh, Byeong-Kwon Ju, and Jaehyun Moon. A Light Scattering Layer for Internal Light Extraction of Organic Light-Emitting Diodes Based on Silver Nanowires. *ACS Appl. Mater. Interfaces*, 8(27):17409–17415, 2016.

[49] Jan B. Preinfalk, Yidenekachew J. Donie, Amos Egel, Matthias Hecht, Jürgen Hüpkes, Karsten Bittkau, Uli Lemmer, and Guillaume Gomard. On the fabrication of disordered nanostructures for light extraction in corrugated oleds. In *Light, Energy and the Environment*, page JW5A.20. Optical Society of America, 2017.

[50] Raphael Pugin, Nicolas Blondiaux, Charmariales T Popa, Philippe Niedermann, Martha Liley, Marta Giazzon, Nedege Mathey, Alan Hubbell, and H Heinzelmann. Surface nanopatterning by polymer self-assembly: from applied research to industrial applications. *Journal of Photopolymer Science and Technology*, 22(2):223–228, 2009.

[51] Rui Liu, Zhuo Ye, Joong-Mok Park, Min Cai, Ying Chen, Kai-Ming Ho, Ruth Shinar, and Joseph Shinar. Microporous phase-separated films of polymer blends for enhanced outcoupling of light from oleds. *Opt. Express*, 19(S6):A1272–A1280, Nov 2011.

[52] Cheng Huang, Markus Moosmann, Jiehong Jin, Tobias Heiler, Stefan Walheim, and Thomas Schimmel. Polymer blend lithography: A versatile method to fabricate nanopatterned self-assembled monolayers. *Beilstein journal of nanotechnology*, 3:620, 2012.

[53] Cholho Lee and Jang-Joo Kim. Enhanced light out-coupling of OLEDs with low haze by inserting randomly dispersed nanopillar arrays formed by lateral phase separation of polymer blends. *Small*, 9(22):3858–63, nov 2013.

[54] Cholho Lee, Kyung-Hoon Han, Kwon-Hyeon Kim, and Jang-Joo Kim. Direct formation of nano-pillar arrays by phase separation of polymer blend for the enhanced out-coupling of organic light emitting diodes with low pixel blurring. *Opt. Express*, 24(6):A488–A496, Mar 2016.

[55] Yidenekachew J. Donie, Michael Smeets, Vladimir Smirnov, Jan B. Preinfalk, Amos Egel, Uli Lemmer, Karsten Bittkau, and Guillaume Gomard. Light management in thin film solar cells using internal scattering layers made by polymer blend lithography. In *Light, Energy and the Environment*, page PTh2A.6. Optical Society of America, 2016.

[56] Radwanul H Siddique, Yidenekachew J Donie, Guillaume Gomard, Sisir Yalamanchili, Tsvetelina Merdzhanova, Uli Lemmer, and Hendrik Hölscher. Bioinspired phase-separated disordered nanostructures for thin photovoltaic absorbers. *Science Advances*, 3(10):e1700232, 2017.

[57] Yidenekachew Jenberu Donie, Michael Smeets, Amos Egel, Florian Lentz, Jan Benedikt Preinfalk, Adrian Mertens, Vladimir Smirnov, Uli Lemmer, Karsten Bittkau, and Guillaume Gomard. Light trapping in thin film silicon solar cells via phase separated disordered nanopillars. *Nanoscale*, 2018.

[58] Sohee Jeon, Sunghun Lee, Kyung-Hoon Han, Hyun Shin, Kwon-Hyeon Kim, Jun-Ho Jeong, and Jang-Joo Kim. High-quality white oleds with comparable efficiencies to leds. *Advanced Optical Materials*, pages 1701349–n/a, 2018. 1701349.

[59] Helmut Bechtel, Wolfgang Busselt, and Joachim Opitz. Subwavelength particle layers for improved light outcoupling of oleds, 2004.

[60] Nobuhiro Nakamura, Nao Fukumoto, Fabrice Sinapi, Naoya Wada, Yumiko Aoki, and Kei Maeda. Glass Substrates for OLED Lighting with High Outcoupling Efficiency OLED on a Glass Scattering Layer. In *SID Symp. Dig. Tech. Pap.*, pages 603–606. Blackwell Publishing Ltd, 2009.

[61] Hong-Wei Chang, Kun-Cheng Tien, Min-Hung Hsu, Yi-Hsiang Huang, et al. 5.4: Distinguished paper: Oleds integrated with internal scattering structure for enhancing optical outcoupling. In *SID Symposium Digest of Technical Papers*, volume 41, pages 50–53. Wiley Online Library, 2010.

[62] Chih-Hao Chang, Kuo-Yan Chang, Yu-Jhong Lo, Shu-Jing Chang, and Hsin-Hua Chang. Fourfold power efficiency improvement in organic light-emitting devices using an embedded nanocomposite scattering layer. *Org. Electron.*, 13(6):1073–1080, jun 2012.

[63] Naoya Wada, Nobuhiro Nakamura, Benoit Domercq, Sophie Billet, Nao Fukumoto, Masamichi Tanida, Yumiko Aoki, and Masao Ohgawara. 68.1: Novel light-scattering glass substrate for the enhancement of oled lighting outcoupling efficiency. *SID Symposium Digest of Technical Papers*, 43(1):922–924, 2012.

[64] Nobuhiro Nakamura, Benoit Domercq, Sophie Billet, Philippe Roquiny, Naoya Wada, Nao Fukumoto, Masamichi Tanida, Yumiko Aoki, and Masao Ohgawara. Advanced glass substrate for the enhancement of oled lighting out-coupling efficiency. *SID Symposium Digest of Technical Papers*, 44(1):803–806, 2013.

[65] Hong-Wei Chang, Jonghee Lee, Simone Hofmann, Yong Hyun Kim, Lars Müller-Meskamp, Björn Lüssem, Chung-Chih Wu, Karl Leo, and Malte C. Gather. Nano-particle based scattering layers for optical efficiency enhancement of organic light-emitting diodes and organic solar cells. *J. Appl. Phys.*, 113(20):204502, 2013.

[66] Jooyoung Lee, Yun Young Kwon, Eun-Ho Choi, JeongWoo Park, Hong Yoon, and Hyunbin Kim. Enhancement of light-extraction efficiency of organic light-emitting diodes using silica nanoparticles embedded in TiO2 matrices. *Opt. Express*, 22(S3):A705—-A714, 2014.

[67] V. S. Veerasamy and Tukaram K. Hatwar. Large Area Deposition of a Light Out-Coupling Layer Stack on Low Cost Soda Lime Glass Substrate. *SID Symp. Dig. Tech. Pap.*, 45(1):1507–1510, jun 2014.

[68] Min-Cheol Oh, Jun-Hwan Park, Hyeong Jin Jeon, and Jeung Sang Go. Hollow-core polymeric nanoparticles for the enhancement of {OLED} outcoupling efficiency. *Displays*, 37:72 – 78, 2015. Advanced {MEMS} technologies and Displays.

[69] Ki-Han Kim and Soo-Young Park. Enhancing light-extraction efficiency of OLEDs with high- and low-refractive-index organicinorganic hybrid materials. *Org. Electron.*, 36:103–112, 2016.

[70] Daniel Riedel, Thomas Wehlus, Thilo C.G. Reusch, and Christoph J. Brabec. Polymer-based scattering layers for internal light extraction from organic light emitting diodes. *Org. Electron.*, 32:27–33, may 2016.

[71] Boris Riedel, Inga Kaiser, Julian Hauss, Uli Lemmer, and Martina Gerken. Improving the outcoupling efficiency of indium-tin-oxide-free organic light-emitting diodes via rough internal interfaces. *Opt. Express*, 18(S4):A631, nov 2010.

[72] Boris Riedel, Julian Hauss, Markus Aichholz, Andre Gall, Uli Lemmer, and Martina Gerken. Polymer light emitting diodes containing nanoparticle clusters for improved efficiency. *Organic Electronics*, 11(7):1172 – 1175, 2010.

[73] Julian Hauss, Tobias Bocksrocker, Boris Riedel, Uli Lemmer, and Martina Gerken. On the interplay of waveguide modes and leaky modes in corrugated OLEDs. *Opt. Express*, 19(S4):A851—-A858, jul 2011.

[74] Jörg Frischeisen, Bert J. Scholz, Benedikt J. Arndt, Tobias D. Schmidt, Robert Gehlhaar, Chihaya Adachi, and Wolfgang Brütting. Strategies for light extraction from surface plasmons in organic light-emitting diodes. *Journal of Photonics for Energy*, 1(1):011004–011004–17, 2011.

[75] Dawn K. Gifford and Dennis G. Hall. Emission through one of two metal electrodes of an organic light-emitting diode via surface-plasmon cross coupling. *Applied Physics Letters*, 81(23):4315–4317, 2002.

[76] Tobias Schwab, Cornelius Fuchs, Reinhard Scholz, Alexander Zakhidov, Karl Leo, and Malte C. Gather. Coherent mode coupling in highly efficient top-emitting oleds on periodically corrugated substrates. *Opt. Express*, 22(7):7524–7537, Apr 2014.

[77] Rico Meerheim, Mauro Furno, Simone Hofmann, Björn Lüssem, and Karl Leo. Quantification of energy loss mechanisms in organic light-emitting diodes. *Appl. Phys. Lett.*, 97(25):253305, 2010.

[78] Amos Egel, Guillaume Gomard, Siegfried Kettlitz, and Uli Lemmer. Accurate optical simulation of nano-particle based internal scattering layers for light outcoupling from organic light emitting diodes. *J. Opt.*, dec 2016.

[79] R R Chance, A Prock, and R Silbey. Molecular Fluorescence and Energy Transfer Near Interfaces. *Adv. Chem. Phys.*, 37:1–65, 1978.

[80] Norbert Danz, Ralf Waldhäusl, Andreas Bräuer, and Richard Kowarschik. Dipole lifetime in stratified media. *J. Opt. Soc. Am. B*, 19(3):412, mar 2002.

[81] EA Hinds. Perturbative cavity quantum electrodynamics. In *Advances in atomic, molecular, and optical physics*, volume 28, pages 237–289. Elsevier, 1990.

[82] SD Brorson, H. Yokoyama, and E.P. Ippen. Spontaneous emission rate alteration in optical waveguide structures. *IEEE J. Quantum Electron.*, 26(9):1492, 1990.

[83] D G Deppe and C Lei. Spontaneous emission from a dipole in a semiconductor microcavity. *J. Appl. Phys.*, 70(7):3443–3448, 1991.

[84] C F Janz and J. N. McMullin. Spontaneous Emission Coupling to Radiation and Guided Modes of Planar Waveguide Structures. *IEEE J. Quantum Electron.*, 31(7):1344–1353, 1995.

[85] V Bulovic, V B Khalfin, G Gu, P E Burrows, D Z Garbuzov, and S R Forrest. Weak microcavity effects in organic light-emitting devices. *Phys. Rev. B*, 58(7):3730–3740, aug 1998.

[86] M.-H. Lu and J C Sturm. Optimization of external coupling and light emission in organic light-emitting devices: modeling and experiment. *J. Appl. Phys.*, 91(2):595–604, 2002.

[87] Alongkarn Chutinan, Kuniaki Ishihara, Takashi Asano, Masayuki Fujita, and Susumu Noda. Theoretical analysis on light-extraction efficiency of organic light-emitting diodes using FDTD and mode-expansion methods. *Org. Electron.*, 6(1):3–9, 2005.

[88] Hans Kuhn. Classical Aspects of Energy Transfer in Molecular Systems. *J. Chem. Phys.*, 53(1):101–108, 1970.

[89] Lukas Novotny and Bert Hecht. *Principles of Nano-Optics*, volume 1. Cambridge University Press, Cambridge, 2006.

[90] E. M. Purcell. Spontaneous emission probabilities at radio frequencies. In *Proc. Am. Phys. Soc.*, volume 69, page 681, 1946.

[91] A. Sommerfeld. über die ausbreitung der wellen in der drahtlosen telegraphie. *Annalen der Physik*, 333(4):665–736, 1909.

[92] Horst Weyl. Ausbreitung elektromagnetischer Wellen über einem ebenen Leiter. *Ann. Phys.*, 365(21):481–500, 1919.

[93] Ariel Epstein. *Rigorous electromagnetic analysis of optical emission of organic light-emitting diodes*. Technion-Israel Institute of Technology, Faculty of Electrical Engineering, 2013.

[94] Setfos homepage. `https://www.fluxim.com/setfos-intro/`.

[95] M Bogdanova, Sergey Belousov, Ilya Valuev, A Zakirov, M Okun, D Shirabaykin, V Chorkov, P Tokar, A Knizhnik, B Potapkin, et al. Simulation platform for multiscale and multiphysics modeling of oleds. *Procedia Computer Science*, 29:740–753, 2014.

[96] Stéphane Altazin, Clément Reynaud, Ursula M Mayer, Thomas Lanz, Kevin Lapagna, Reto Knaack, Lieven Penninck, Christoph Kirsch, Kurt P Pernstich, Stephan Harkema, et al. Simulations, measurements, and optimization of oleds with scattering layer. In *SID Symposium Digest of Technical Papers*, volume 46, pages 564–567. Wiley Online Library, 2015.

[97] Jinouk Song, Eunhye Kim, and Seunghyup Yoo. Feasibility of radiative transfer theory for simulation of organic light-emitting diodes with scattering media. In *Conference on Lasers and Electro-Optics/Pacific Rim*, page 27P_107. Optical Society of America, 2015.

[98] Jinouk Song, Eunhye Kim, Jaeho Lee, Jin Chung, and Seunghyup Yoo. Transscale global optimization of oleds on substrates with bulk scattering via radiative transfer theory. In *Optical Nanostructures and Advanced Materials for Photovoltaics*, pages JTu5A–8. Optical Society of America, 2015.

[99] Bahareh Ramezan pour and Daniel W. Mackowski. Radiative transfer equation and direct simulation prediction of reflection and absorption by particle deposits. *Journal of Quantitative Spectroscopy and Radiative Transfer*, 189:361 – 368, 2017.

[100] R.H.T. Bates. Analytic Constraints on Electromagnetic Field Computations. *IEEE Trans. Microw. Theory Tech.*, 23(8):605–623, aug 1975.

[101] RF Oulton, CS Adjiman, K Handa, and S Aramaki. Efficiency enhancement of organic based light emitting diodes using a scattering layer. *arXiv preprint physics/0411095*, 2004.

[102] Kane Yee. Numerical solution of initial boundary value problems involving maxwell's equations in isotropic media. *IEEE Transactions on Antennas and Propagation*, 14(3):302–307, May 1966.

[103] J. L. Volakis, A. Chatterjee, and L. C. Kempel. Review of the finite-element method for three-dimensional electromagnetic scattering. *J. Opt. Soc. Am. A*, 11(4):1422–1433, Apr 1994.

[104] Lumerical homepage. `https://www.lumerical.com/`.

[105] Comsol multiphysics. `https://www.comsol.com/`.

[106] Jcmwave homepage. `https://www.jcmwave.com/`.

[107] Meep online documentation. `https://meep.readthedocs.io`.

[108] SW Liu, JX Wang, Yoga Divayana, Kapil Dev, Swee Tiam Tan, Hilmi Volkan Demir, and XW Sun. An efficient non-lambertian organic light-emitting diode using imprinted submicron-size zinc oxide pillar arrays. *Applied Physics Letters*, 102(5):26, 2013.

[109] Michiel Koen Callens, Herman Marsman, Lieven Penninck, Patrick Peeters, Harry de Groot, Jan Matthijs ter Meulen, and Kristiaan Neyts. Rcwa and fdtd modeling of light emission from internally structured oleds. *Optics express*, 22(103):A589–A600, 2014.

[110] Keunsoo Lee, Jin-Wook Shin, Jun-Hwan Park, Jonghee Lee, Chul Woong Joo, Jeong-Ik Lee, Doo-Hee Cho, Jong Tae Lim, Min-Cheol Oh, Byeong-Kwon Ju, et al. A light scattering layer for internal light extraction of organic light-emitting diodes based on silver nanowires. *ACS applied materials & interfaces*, 8(27):17409–17415, 2016.

[111] Lin Zschiedrich, Horst J Greiner, Sven Burger, and Frank Schmidt. Numerical analysis of nanostructures for enhanced light extraction from oleds. In *Light-Emitting Diodes: Materials, Devices, and Applications for Solid State Lighting XVII*, volume 8641, page 86410B. International Society for Optics and Photonics, 2013.

[112] Pasi Yla-Oijala, Johannes Markkanen, Seppo Jarvenpaa, and Sami P Kiminki. Surface and volume integral equation methods for time-harmonic solutions of maxwell's equations. *Progress In Electromagnetics Research*, 149:15–44, 2014.

[113] Matthys M Botha. Solving the volume integral equations of electromagnetic scattering. *Journal of Computational Physics*, 218(1):141–158, 2006.

[114] Bruce T Draine and Piotr J Flatau. Discrete-dipole approximation for scattering calculations. *JOSA A*, 11(4):1491–1499, 1994.

[115] RF Harrington. *Field Calculations by Moment Methods*. New York: MacMillan, 1968.

[116] Michael Paulus and Oliver J. F. Martin. Light propagation and scattering in stratified media: a green's tensor approach. *J. Opt. Soc. Am. A*, 18(4):854–861, Apr 2001.

[117] Maxim A Yurkin and Marcus Huntemann. Rigorous and fast discrete dipole approximation for particles near a plane interface. *The Journal of Physical Chemistry C*, 119(52):29088–29094, 2015.

[118] Horst Greiner and Olivier JF Martin. Numerical modeling of light emission and propagation in organic leds using the green's tensor. In *Organic Light-Emitting Materials and Devices VII*, volume 5214, pages 248–260. International Society for Optics and Photonics, 2004.

[119] MG Moharam and TK Gaylord. Rigorous coupled-wave analysis of planar-grating diffraction. *JOSA*, 71(7):811–818, 1981.

[120] P Bienstman. *Rigorous and efficient modelling of wavelength scale photonic components. Ghent University*. PhD thesis, Phd. thesis, 2001. http://photonics. intec. ugent. be/publications/phd. asp, 2001.

[121] Lei Zhou, Xiaochen Jiang, Yanqing Li, Aili Shi, Jingde Chen, Qingdong Ou, Haitao Liu, and Jianxin Tang. Light extraction of trapped optical modes in polymer light-emitting diodes with nanoimprinted double-pattern gratings. *ACS applied materials & interfaces*, 6(20):18139–18146, 2014.

[122] Christian Kluge, Jost Adam, Nicole Barié, Peter-Jürgen Jakobs, Markus Guttmann, and Martina Gerken. Multi-periodic nanostructures for photon control. *Optics Express*, 22(105):A1363–A1371, 2014.

[123] Stefano Boscolo and Michele Midrio. Three-dimensional multiple-scattering technique for the analysis of photonic-crystal slabs. *Journal of lightwave technology*, 22(12):2778, 2004.

[124] Davy Pissoort, Eric Michielssen, Dries Vande Ginste, and Femke Olyslager. Fast-multipole analysis of electromagnetic scattering by photonic crystal slabs. *Journal of lightwave technology*, 25(9):2847–2863, 2007.

[125] Xun Lu, Hualiang Shi, and Ya Yan Lu. Vertical mode expansion method for transmission of light through a single circular hole in a slab. *JOSA A*, 31(2):293–300, 2014.

[126] Amos Egel and Uli Lemmer. Dipole emission in stratified media with multiple spherical scatterers: Enhanced outcoupling from OLEDs. *J. Quant. Spectrosc. Radiat. Transf.*, 148:165–176, 2014.

[127] Amos Egel, Siegfried W. Kettlitz, and Uli Lemmer. Efficient evaluation of Sommerfeld integrals for the optical simulation of many scattering particles in planarly layered media. *J. Opt. Soc. Am. A*, 33(4):698, mar 2016.

[128] Lieven Penninck, Patrick De Visschere, Jeroen Beeckman, and Kristiaan Neyts. Dipole radiation within one-dimensional anisotropic microcavities: a simulation method. *Opt. Express*, 19(19):18558, sep 2011.

[129] Andreas Kirsch and Frank Hettlich. *The Mathematical Theory of Time-Harmonic Maxwell's Equations*. Springer International Publishing, Heidelberg, 1 edition, 2015.

[130] P M Morse and H Feshbach. *Methods of Theoretical Physics*, volume 2. McGraw-Hill, New York, 1953.

[131] Thorkild Hansen and Arthur D. Yaghjian. *Plane-wave theory of time-domain fields: near-field scanning applications*. IEEE Press, 1999.

[132] Anders Boström, Gerhard Kristensson, and Staffan Ström. *Transformation properties of plane, spherical and cylindrical scalar and vector wave functions*, volume 1 of *Acoustic, Electromagnetic and Elastic Wave Scattering, Field Representations and Introduction to Scattering*, pages 165–210. Elsevier, 1991.

[133] Y A Doicu, A; Wriedt, T; Eremin. *Light Scattering by Systems of Particles*. Springer-Verlag, Berlin, Heidelberg, 1 edition, 2006.

[134] Gerhard Kristensson. *Scattering of Electromagnetic Waves by Obstacles*. Institution of Engineering and Technology, jul 2016.

[135] Michael I. Mishchenko, Larry D. Travis, and Andrew A. Lacis. *Scattering, Absorption, and Emission of Light by Small Particles*. Cambridge University Press, 2002.

[136] R. M. A. Azzam and N. M. Bashara. *Ellipsometry and polarized light*. North-Holland, 1977.

[137] DYK Ko and JR Sambles. Scattering matrix method for propagation of radiation in stratified media: attenuated total reflection studies of liquid crystals. *JOSA A*, 5(11):1863–1866, 1988.

[138] S.˜A. Dyakov, V.˜A. Tolmachev, E.˜V. Astrova, S.˜G. Tikhodeev, V.˜Y. Timoshenko, and T.˜S. Perova. Numerical methods for calculation of optical properties of layered structures. In *Int. Conf. Micro- Nano-Electronics 2009*, volume 7521 of *procspie*, page 75210G, 2009.

[139] Bin Hu and Weng Cho Chew. Fast inhomogeneous plane wave algorithm for electromagnetic solutions in layered medium structures: Two-dimensional case. *Radio Science*, 35(1):31–43, 2000.

[140] Michael I Mishchenko, Gorden Videen, Victor A Babenko, Nikolai G Khlebtsov, and Thomas Wriedt. T-matrix theory of electromagnetic scattering by partciles and its applications: a comprehensive reference database. *J. Quant. Spectrosc. Radiat. Transf.*, 88(1-3):357–406, sep 2004.

[141] Michael I Mishchenko, Gorden Videen, Victor A Babenko, Nikolai G Khlebtsov, and Thomas Wriedt. Comprehensive T-matrix reference database: A 200406 update. *J. Quant. Spectrosc. Radiat. Transf.*, 106(13):304–324, 2007.

[142] Michael I Mishchenko, Gorden Videen, Nikolai G Khlebtsov, Thomas Wriedt, and Nadia T Zakharova. Comprehensive T-matrix reference database: A 200607 update. *J. Quant. Spectrosc. Radiat. Transf.*, 109(8):1447–1460, 2008.

[143] Michael I. Mishchenko, Nadia T. Zakharova, Gorden Videen, Nikolai G. Khlebtsov, and Thomas Wriedt. Comprehensive T-matrix reference database: A 20072009 update. *J. Quant. Spectrosc. Radiat. Transf.*, 111(4):650–658, mar 2010.

[144] Michael I. Mishchenko, Gorden Videen, Nikolai G. Khlebtsov, and Thomas Wriedt. Comprehensive T-matrix reference database: A 20122013 update. *J. Quant. Spectrosc. Radiat. Transf.*, 123:145–152, jul 2013.

[145] Michael I. Mishchenko, Nadezhda T. Zakharova, Nikolai G. Khlebtsov, Thomas Wriedt, and Gorden Videen. Comprehensive thematic T-matrix reference database: A 20132014 update. *J. Quant. Spectrosc. Radiat. Transf.*, 146:349–354, 2014.

[146] Nadezhda T. Zakharova, Nikolai G. Khlebtsov, Gorden Videen, and Thomas Wriedt. Comprehensive thematic T-matrix reference database: A 20142015 update. *J. Quant. Spectrosc. Radiat. Transf.*, 178:276–283, 2016.

[147] A Doicu and T Wriedt. Extended boundary condition method with multipole sources located in the complex plane. *Optics communications*, 139(1-3):85–91, 1997.

[148] Daniel W. Mackowski. Discrete dipole moment method for calculation of the t matrix for nonspherical particles. *J. Opt. Soc. Am. A*, 19(5):881–893, May 2002.

[149] Johannes Markkanen and Alex J. Yuffa. Fast superposition t-matrix solution for clusters with arbitrarily-shaped constituent particles. *Journal of Quantitative Spectroscopy and Radiative Transfer*, 189:181 – 188, 2017.

[150] Martin Fruhnert, Ivan Fernandez-Corbaton, Vassilios Yannopapas, and Carsten Rockstuhl. Computing the t-matrix of a scattering object with multiple plane wave illuminations. *Beilstein journal of nanotechnology*, 8:614, 2017.

[151] Gustav Mie. Beiträge zur Optik trüber Medien, speziell kolloidaler Metallösungen. *Ann. Phys.*, 330(3):377–445, 1908.

[152] Craig F Bohren and D R Huffman. *Absorption and scattering of light by small particles*. Wiley science paperback series. Wiley, 1983.

[153] Jean Lerm, Christophe Bonnet, Michel Broyer, Emmanuel Cottancin, Delphine Manchon, and Michel Pellarin. Optical properties of a particle above a dielectric interface: Cross sections, benchmark calculations, and analysis of the intrinsic substrate effects. *The Journal of Physical Chemistry C*, 117(12):6383–6398, 2013.

[154] EF Kuester and DC Chang. Evaluation of Sommerfeld integrals associated with dipole sources above Earth. Technical report, Electromagnetics Laboratory, University of Colorado, Boulder, 1979.

[155] Weng Cho Chew. *Waves and Fields in Inhomogeneous Media*. IEEE Press, New York, 1996.

[156] Deb Chatterjee, Sadasiva M. Rao, and Michael S. Kluskens. Analytical evaluation of Sommerfeld integral tails for layered-media Green's functions. In *2011 IEEE Int. Symp. Antennas Propag.*, pages 2150–2153. IEEE, jul 2011.

[157] A. Doicu, Yu.A. Eremin, and T. Wriedt. Convergence of the t-matrix method for light scattering from a particle on or near a surface. *Optics Communications*, 159(4):266 – 277, 1999.

[158] Cecilia Cappellin, Olav Breinbjerg, and Aksel Frandsen. Properties of the transformation from the spherical wave expansion to the plane wave expansion. *Radio Sci.*, 43(1):n/a–n/a, feb 2008.

[159] A. Egel, D. Theobald, Y. Donie, U. Lemmer, and G. Gomard. Light scattering by oblate particles near planar interfaces: On the validity of the T-matrix approach. *Opt. Express*, 24(22), 2016.

[160] Amos Egel, Yuri Eremin, Thomas Wriedt, Dominik Theobald, Uli Lemmer, and Guillaume Gomard. Extending the applicability of the t-matrix method to light scattering by flat particles on a substrate via truncation of sommerfeld integrals. *Journal of Quantitative Spectroscopy and Radiative Transfer*, 202(Supplement C):279 – 285, 2017.

[161] Smuthi online documentation. `http://smuthi.readthedocs.io`.

[162] Sphinx project home page. `http://www.sphinx-doc.org`.

[163] Smuthi repository. `https://gitlab.com/AmosEgel/smuthi`.

[164] Dominik Theobald. Simulation der Streuung elektromagnetischer Strahlulng sn sphäroidalen Nanopartikeln zur Lichtauskopplung aus OLEDs. Master's thesis, Karlsruhe Institute or Technology, Karlsruhe, Germany, 2015.

[165] Thomas C. Rosenow, Mauro Furno, Sebastian Reineke, Selina Olthof, Björn Lüssem, and Karl Leo. Highly efficient white organic light-emitting diodes based on fluorescent blue emitters. *J. Appl. Phys.*, 108(11):113113, dec 2010.

[166] Norbert Danz, Jörg Heber, Andreas Bräuer, and Richard Kowarschik. Fluorescence lifetimes of molecular dye ensembles near interfaces. *Phys. Rev. A*, 66:063809, Dec 2002.

[167] Christian Stamm. Planarisierung von Streuschichten zur verbesserten Lichtauskopplung aus OLEDs. Master's thesis, Karlsruhe Institute or Technology, Karlsruhe, Germany, 2017.

[168] Monica Skoge, Aleksandar Donev, Frank H. Stillinger, and Salvatore Torquato. Packing hyperspheres in high-dimensional euclidean spaces. *Phys. Rev. E*, 74:041127, Oct 2006.

[169] Gaurasundar M. Conley, Matteo Burresi, Filippo Pratesi, Kevin Vynck, and Diederik S. Wiersma. Light transport and localization in two-dimensional correlated disorder. *Phys. Rev. Lett.*, 112:143901, Apr 2014.

[170] Ilya Valmianski. Two point correlation function of a finite 2d lattice. `https://de.mathworks.com/matlabcentral/fileexchange/31353-two-point-correlation-function-of-a-finite-2d-lattice`.

[171] Christopher Wiesmann. Nano-structured leds – light extraction mechanisms and applications, July 2010.

[172] Leslie Greengard and Vladimir Rokhlin. A fast algorithm for particle simulations. *Journal of computational physics*, 73(2):325–348, 1987.

[173] Nail A Gumerov and Ramani Duraiswami. Computation of scattering from clusters of spheres using the fast multipole method. *The Journal of the Acoustical Society of America*, 117(4):1744–1761, 2005.

[174] Zydrunas Gimbutas and Leslie Greengard. Fast multi-particle scattering: A hybrid solver for the maxwell equations in microstructured materials. *Journal of Computational Physics*, 232(1):22–32, 2013.

[175] Johannes Markkanen and Alex J Yuffa. Fast superposition t-matrix solution for clusters with arbitrarily-shaped constituent particles. *Journal of Quantitative Spectroscopy and Radiative Transfer*, 189:181–188, 2017.

[176] JJ Goodman, Bruce T Draine, and Piotr J Flatau. Application of fast-fourier-transform techniques to the discrete-dipole approximation. *Optics Letters*, 16(15):1198–1200, 1991.

[177] WC Chew, JH Lin, and XG Yang. An fft t-matrix method for 3d microwave scattering solutions from random discrete scatterers. *Microwave and Optical Technology Letters*, 9(4):194–196, 1995.

[178] Xue Min Xu and Qing H Liu. The bcgs-fft method for electromagnetic scattering from inhomogeneous objects in a planarly layered medium. *IEEE antennas and wireless propagation letters*, 1(1):77–80, 2002.

Peer-reviewed journal publications

[1] Jan Mescher, Siegfried W Kettlitz, Amos Egel, Carola Moosmann, Nico S Christ, Sebastian Valouch, and Uli Lemmer. Rc-constant in organic photodiodes comprising electrodes with a significant sheet resistance. *IEEE Photonics Technology Letters*, 26(6):579–582, 2014.

[2] Stefan Hofle, Tobias Lutz, Amos Egel, Felix Nickel, Siegfried W Kettlitz, Guillaume Gomard, Uli Lemmer, and Alexander Colsmann. Influence of the emission layer thickness on the optoelectronic properties of solution processed organic light-emitting diodes. *ACS Photonics*, 1(10):968–973, 2014.

[3] Amos Egel and Uli Lemmer. Dipole emission in stratified media with multiple spherical scatterers: Enhanced outcoupling from oleds. *Journal of Quantitative Spectroscopy and Radiative Transfer*, 148:165–176, 2014.

[4] Jan Mescher, Adrian Mertens, Amos Egel, Siegfried W Kettlitz, Uli Lemmer, and Alexander Colsmann. Illumination angle and layer thickness influence on the photo current generation in organic solar cells: A combined simulative and experimental study. *AIP Advances*, 5(7):077188, 2015.

[5] Jan B Preinfalk, Fabian R Schackmar, Thomas Lampe, Amos Egel, Tobias D Schmidt, Wolfgang Brutting, Guillaume Gomard, and Uli Lemmer. Tuning the microcavity of organic light emitting diodes by solution processable polymer–nanoparticle composite layers. *ACS applied materials & interfaces*, 8(4):2666–2672, 2016.

[6] Frederik Mayer, Robert Schittny, Amos Egel, Andreas Niemeyer, Jan Preinfalk, Ulrich Lemmer, and Martin Wegener. Cloaking contacts on large-area organic light-emitting diodes. *Advanced Optical Materials*, 4(5):740–745, 2016.

[7] Amos Egel, Siegfried W Kettlitz, and Uli Lemmer. Efficient evaluation of sommerfeld integrals for the optical simulation of many scattering particles in planarly layered media. *JOSA A*, 33(4):698–706, 2016.

[8] Guillaume Gomard, Jan B Preinfalk, Amos Egel, and Uli Lemmer. Photon management in solution-processed organic light-emitting diodes: a review of light outcoupling micro-and nanostructures¡ xref ref-type=. *Journal of Photonics for Energy*, 6(3):030901, 2016.

[9] Amos Egel, Dominik Theobald, Yidenekachew Donie, Uli Lemmer, and Guillaume Gomard. Light scattering by oblate particles near planar interfaces: on the validity of the t-matrix approach. *Optics express*, 24(22):25154–25168, 2016.

[10] Amos Egel, Guillaume Gomard, Siegfried W Kettlitz, and Uli Lemmer. Accurate optical simulation of nano-particle based internal scattering layers for light outcoupling from organic light emitting diodes. *Journal of Optics*, 19(2):025605, 2017.

[11] Amos Egel, Lorenzo Pattelli, Giacomo Mazzamuto, Diederik S Wiersma, and Uli Lemmer. Celes: Cuda-accelerated simulation of electromagnetic scattering by large ensembles of spheres. *Journal of Quantitative Spectroscopy and Radiative Transfer*, 199:103–110, 2017.

[12] Amos Egel, Yuri Eremin, Thomas Wriedt, Dominik Theobald, Uli Lemmer, and Guillaume Gomard. Extending the applicability of the t-matrix method to light scattering by flat particles on a substrate via truncation of sommerfeld integrals. *Journal of Quantitative Spectroscopy and Radiative Transfer*, 202:279–285, 2017.

[13] Dominik Theobald, Amos Egel, Guillaume Gomard, and Uli Lemmer. Plane-wave coupling formalism for t-matrix simulations of light scattering by non-spherical particles. *Physical Review A*, 96(3):033822, 2017.

[14] Yidenekachew Jenberu Donie, Michael Smeets, Amos Egel, Florian Lentz, Jan Benedikt Preinfalk, Adrian Mertens, Vladimir Smirnov, Uli Lemmer, Karsten Bittkau, and Guillaume Gomard. Light trapping in thin film silicon solar cells via phase separated disordered nanopillars. *Nanoscale*, 2018.

[15] Lorenzo Pattelli, Amos Egel, Uli Lemmer, and Diederik Wiersma. Role of packing density and spatial correlations in strongly scattering 3d systems. (submitted).

Conference proceedings

[1] Amos Egel, Tobias Bocksrocker, and Uli Lemmer. Extracting substrate modes from flexible oleds. In *Solid-State and Organic Lighting*, pages DT2E–3. Optical Society of America, 2013.

[2] Amos Egel and Uli Lemmer. Coherent and near field effects in light scattering at disordered spherical particle ensembles embedded in metal-dielectric thin film systems. In *Bremen Workshop on Light Scattering 2015*, number Light Scattering by Complex Particles, pages 28–31. epubli, 2015.

[3] Yidenekachew J Donie, Michael Smeets, Vladimir Smirnov, Jan B Preinfalk, Amos Egel, Uli Lemmer, Karsten Bittkau, and Guillaume Gomard. Light management in thin film solar cells using internal scattering layers made by polymer blend lithography. In *Optical Nanostructures and Advanced Materials for Photovoltaics*, pages PTh2A–6. Optical Society of America, 2016.

[4] Amos Egel, Dominik Theobald, Yidenekachew J Donie, Jan B Preinfalk, Guillaume Gomard, and Uli Lemmer. Accurate modeling of outcoupling from oleds: Volumetric versus flat internal scattering layers. In *Solid-State Lighting*, pages SSW2D–3. Optical Society of America, 2016.

[5] Amos Egel and Uli Lemmer. Singularity extraction of higher order sommerfeld integrals. In *Bremen Workshop on Light Scattering 2016*, number Light Scattering by Particles, pages 14–19. epubli, 2016.

[6] Jan B Preinfalk, Yidenekachew J Donie, Amos Egel, Matthias Hecht, Jürgen Hüpkes, Karsten Bittkau, Uli Lemmer, and Guillaume Gomard. On the fabrication of disordered nanostructures for light extraction in corrugated oleds. In *Optics for Solar Energy*, pages JW5A–20. Optical Society of America, 2017.

[7] Amos Egel, Yuri Eremin, Thomas Wriedt, Dominik Theobald, and Uli Lemmer. Light scattering by oblate particles near an interface: Improved accuracy of t-matrix calculations through sommerfeld integral truncation. In *Bremen Workshop on Light Scattering 2017*, number Light Scattering by Particles, pages 78–83. epubli, 2017.

[8] Dominik Theobald, Amos Egel, Guillaume Gomard, and Uli Lemmer. Simulation of light scattering in clusters of nonspherical nanoparticles: an adapted t-matrix approach. *Proc.SPIE*, 10672:10672 – 10672 – 9, 2018.

Supervised thesis projects

[1] Christian Berten. Erstellung eines Werkzeuges zur Analyse und Bewertung bionischer Oberflächenstrukturen für CIGS-Solarzellen mittels Raytracingsimulation. B.S. Thesis, Karlsruhe Institute or Technology, Karlsruhe, Germany, 2014.

[2] Hans-Christian Yorck. Streuung an einer dieklektrischen Kugel in einem planaren Wellenleiter. Diploma Thesis, Karlsruhe Institute or Technology, Karlsruhe, Germany, 2014.

[3] Matthias Hecht. Beam-Shaping of Organic Light Emitting Diodes. Master's thesis, Karlsruhe Institute or Technology, Karlsruhe, Germany, 2014.

[4] Julian Bolter. Schätzung der Emissionszone organischer Leuchtdioden. B.S. Thesis, Karlsruhe Institute or Technology, Karlsruhe, Germany, 2015.

[5] Dominik Theobald. Simulation der Streuung elektromagnetischer Strahlung an sphroidalen Nanopartikeln zur Lichtauskopplung aus OLEDs. Master's thesis, Karlsruhe Institute or Technology, Karlsruhe, Germany, 2015.

[6] Swantje Pauer. Planare Wellenleiter mit Streuschichten. B.S. Thesis, Karlsruhe Institute or Technology, Karlsruhe, Germany, 2017.

[7] Christian Stamm. Planarisierung von Streuschichten zur verbesserten Lichtauskopplung aus OLEDs. Master's thesis, Karlsruhe Institute or Technology, Karlsruhe, Germany, 2017.